



TECHNISCHE
UNIVERSITÄT
WIEN
Vienna University of Technology

DISSERTATION

Characterization of Compound Refractive Lenses for synchrotron μ -XRF and μ -XAS and applications with high spatial resolution

ausgeführt zum Zwecke der Erlangung des akademischen Grades eines
Doktors der technischen Wissenschaften unter der Leitung von

Ao. Univ. Prof. Dipl.-Ing. Dr. techn. Christina Strelt

141

Atominstitut der österreichischen Universitäten

eingereicht an der Technischen Universität Wien

Fakultät für Physik

von

Dipl. Ing. Günter Buzanich

9525973

Hubertusgasse 14, 2732 Zweiersdorf

Wien, am _____

*'Write in your notebook every day
even if you have to write
that you didn't do a damn thing.
It makes you know what you have done
and what you should do next.'*

Willis R. Whitney (1974)

Kurzfassung

Die Röntgenfluoreszenzanalyse (XRF) ist eine der am weitest verbreiteten Methoden der Elementanalyse. Die Beliebtheit der Methode ist vor allem darauf zurückzuführen, dass sie eine von wenigen zerstörungsfreien Methoden zur qualitativen und quantitativen Analyse von Spurenelementen ist. Eine weitere vielgenutzte und leistungsfähige Analysetechnik ist die Röntgenabsorptionsspektroskopie (XAS). Hierbei werden die Absorptionskanten der Elemente mit hoher Energieauflösung untersucht, wobei Informationen über das Umfeld des betrachteten Atoms wie z.B. Oxidationszahl oder Bindungsabstände erhalten werden.

Die Änderungen physikalischer und chemischer Eigenschaften von Materialien auf räumlichen Skalen im μm Bereich und darunter, führten zu einer wachsenden Nachfrage nach Analysemethoden mit hoher Auflösung. Dies führte zu einer rasanten Entwicklung von neuen und besseren Röntgenoptiken, welche derzeit Brennfleckgrößen im μm Bereich für Laborquellen und im 10 nm Bereich für Synchrotronquellen erreichen.

Die erreichbaren Strahlgrößen von den hier untersuchten Compound Refractive Lenses (CRLs) liegen derzeit bei etwa 100 nm. Dies ist jedoch abhängig von wählbaren Parametern wie Fokusabstand und Apertur, sowie von vorgegebenen, wie Quellgröße und Strahldivergenz. Zudem sind Parameter wie Fokusabstand und Strahlgröße sehr stark energieabhängig, weshalb jede Linse nur für eine bestimmte Energie verwendet werden kann. Die Vorteile dieser Optiken sind die vergleichsweise geringen Kosten und die einfache Installation, wodurch RFA-Messungen mit sub- μm Auflösung an praktischer jeder Beamline ermöglicht werden.

Die *BAMline* ist ausgelegt für harte Röntgenstrahlung und verfügt über zwei optische Elemente, einen Kristall- (DCM) und einen Multilayer-monochromator (DMM). Während der DCM mit einer Energiebandbreite von $\Delta E/E \approx 0.02\%$ sich für Messungen die eine gute Energieauflösung erfordern (z.B. XAS) eignet, liefert der DMM ($\Delta E/E \approx 1.6\%$) eine etwa 100-fach höhere Flussdichte und ist daher für XRF-Messungen besser geeignet.

Die starke Energieabhängigkeit der CRLs, besonders hinsichtlich XAS Messungen, spricht eigentlich gegen deren Verwendung für diese Art von Messungen, die offensichtlichen Vorteile waren jedoch Anlass genug eine ausführliche Untersuchung durchzuführen.

Ein Satz von 16 Linsen montiert auf einem Si-Wafer wurde am IMT (Institut für Mikrostrukturtechnik) in Karlsruhe hergestellt. Voruntersuchungen an der *BAMline* haben gezeigt, dass mit den vorgegebenen Parametern die erreichbare Spotgröße im Bereich von 1 μm liegt.

II

Das Ziel dieser Arbeit war es, die Linsenparameter, unter verschiedensten Strahlbedingungen zu bestimmen, z.B. unter Verwendung des DMM und unterschiedlicher Vorfokussierung. Desweiteren sollte die Verwendbarkeit für XAS-Messungen ausgiebig geprüft werden.

Die Änderungen der Linsenparameter wurden mithilfe eines bildgebenden Verfahrens unter Verwendung einer hochauflösenden CCD-Kamera ermittelt. Um die Änderung der Absorption in der Linse in Abhängigkeit der Energie zu untersuchen und zu korrigieren, wurden Messungen an Standards mit und ohne Linse durchgeführt und verglichen. Die Untersuchung der Energieabhängigkeit der Linsen hat gezeigt, dass die Änderungen für den XANES-Bereich gering sind, während sie für den EXAFS-Bereich signifikant sind.

Es ist bekannt, dass der Wirkungsgrad von polykristallinen Solarzellen stark abhängig vom Grad der Verunreinigung mit Metallen wie Kupfer und Eisen und deren Verteilung in der Solarzelle ist. Mittels μ -XRF konnten hochaufgelöste zweidimensionale Abbildungen der Verteilung dieser Verunreinigungen erstellt werden. Zusätzliche Aussagen über die Tiefe ausgewählter Ausscheidungen in der Zelle konnten aus dem Verhältnis des $\text{Cu-K}_{\alpha}/\text{Cu-K}_{\beta}$ Signales ermittelt werden. Mikro-XANES Messungen an den Cu-Ausscheidungen legen nahe, dass unterschiedliche Cu-Verbindungen in Solarzellen vorkommen können. Die untersuchten Ausscheidungen in dieser Probe bestanden höchstwahrscheinlich aus Kupfersilizid (Cu_3Si) und Kupferoxid (Cu_2O). Das Wissen um die räumliche Verteilung und die Art der Cu-Verbindung sind unverzichtbare Informationen, um ein erfolgreiches "defect engineering" durchzuführen. Das Ziel dabei ist es, trotz Verwendung von billigerem und daher "schmutzigerem" Ausgangsmaterial, den Wirkungsgrad von Solarzellen zu erhöhen.

Eine weitere Anwendung war die Untersuchung von Keramiken aus Portugal, hergestellt zwischen dem 16. und 18. Jahrhundert in Lissabon bzw. Coimbra. Das Ziel dieser Untersuchung war es, nicht die eigentliche Keramik, sondern das System Glasur und Dekoration zu analysieren, um Angaben über die Produktionsweise der Keramiken machen zu können. Mittels Synchrotron μ -XRF wurden Linienscans an Querschnitten verschiedenster Proben durchgeführt und Profile der Hauptelemente für Dekor, Glasur und Keramik erstellt. Hauptelemente hierbei sind z.B. Co für blau und Sb für gelb sowie Pb für die Glasur und Fe für die Keramik. Als genereller Unterschied konnte die Dicke der Glasur mit bis zu 200 μm für faiences (z.B. Teller oder Vasen) und bis zu 400 μm für tiles (dekorative Wandfliesen) ermittelt werden. Außerdem konnten Unterschiede in der Verteilung der charakteristischen Elemente der Dekoration in der Glasur festgestellt werden, sowohl zwischen den Keramiken als auch zwischen den Produktionsstätten.

Abstract

The X-ray Fluorescence analysis (XRF) is one of the widest spread methods for elemental analysis. The popularity of the method is mainly based on the fact, that it is one of only a few non-destructive methods for qualitative and quantitative trace element analysis. Another powerful analytical technique is X-ray Absorption Spectroscopy (XAS). Thereby, absorption edges of elements are examined with high energy resolution, providing information about the environment of the probed atom like oxidation number or bond distances.

The changes in physical and chemical properties of materials, on spatial scales in the micrometer range and below, resulted in a growing demand for analytical methods with a high resolution. This led to a rapid development of new and better X-ray optics, which currently achieve spot sizes in the μm range for laboratory sources and in the 10 nm range for synchrotron sources.

The achievable beam sizes of the investigated compound refractive Lenses (CRLs) are currently at about 100 nm, but this depends of selectable parameters such as focus distance and aperture, as well as given parameters like the source size and beam divergence. In addition, parameters such as focus distance and beam size are highly energy dependent, so each lens can only be used for a given energy. The advantages of these lenses are the relatively low costs and the ease of installation, which allows XRF measurements with sub- μm resolution at practical each beamline.

The BAMline is a hard X-rays beamline and has two optical elements, a crystal (DCM) and a multilayer monochromator (DMM). While the DCM with an energy bandwidth of $\Delta E/E = 0.02\%$ is suitable for measurements which require a good energy resolution (e.g. XAS), the DMM with a bandwidth of $\Delta E/E = 1.6\%$ provides an about 100-times higher flux density and is therefore suitable for XRF measurements.

The strong energy dependence of the CRLs, particularly with regard to XAS measurements, speaks actually against the use of this type of optics for this kind of measurements. The obvious advantages, however, were reason enough to carry out a detailed investigation.

A set of 16 lenses mounted on a Si wafer was produced at IMT (Institute of microstructure technology) in Karlsruhe. Preliminary investigations at the BAMline have shown, that with the given parameters, the achievable spot size in the range of 1 μm . The aim of this work was to determine the lens parameters under different beam conditions of the BAMline as e.g. with

the DMM and different prefocusing conditions. Furthermore, an extensive study regarding the usability for X-ray absorption spectroscopy (XAS) was conducted.

The changes in the lens parameters were determined by using an X-ray imaging setup with a high resolution CCD camera. The investigation of the energy dependence of the lenses showed that there are only minor changes in the XANES region, while for the EXAFS region the changes are significant. To examine and correct the changes due to the absorption within the lens depending on the energy, measurements with and without lens were carried out on standards and compared.

It is known, that the efficiency of polycrystalline photovoltaic cells is strongly dependent on the degree of contamination with metals such as copper and iron, and their distribution in the solar cell. The application of CRLs in μ -XRF analysis allowed a high resolution two-dimensional mapping of relevant contaminations and localization of their sites of deposition. Depth information for selected precipitates was obtained by the $\text{Cu-K}_\alpha/\text{Cu-K}_\beta$ ratio and μ -XANES measurements revealed that different Cu-compounds are present in the solar cell. The investigated precipitates in this sample consisted most probably of copper silicide (Cu_3Si) and copper oxide (Cu_2O). The knowledge of the spatial distribution and the nature of the Cu compound are essential to perform a successful "defect engineering", with the aim to increase the solar cell efficiency despite the use of cheaper but therefore dirtier feedstock.

Another application was the study of glazed ceramic fragments from Portugal, made between the XVI and XVIII century in Lisbon and Coimbra. The aim of this study was to investigate not the actual ceramic, but the system of glaze and decoration in order to gain data about the production process. Synchrotron micro X-ray fluorescence analysis was used to perform cross section scans on various samples to monitor the profiles of the key elements from decoration, glaze and body. The key elements are e.g. Co for blue and Sb for yellow as well as Pb for the glaze and Fe for the body. The general difference between faiences (consumer goods like plates or vases) and tiles (e.g. decorative wall tiles) is the thickness of the glaze, which is up to 200 μm for faiences and up to 400 μm for tiles. Also differences in the distribution of the characteristic elements from the decoration within the glaze were found for the different kinds of ceramics as well as for the different production centers.

A part of the work reported in this thesis appears in following publications:

- G. Buzanich, M. Radtke, U. Reinholz, H. Riesemeier, and C. Strelt, *Micro-X-ray absorption spectroscopy with compound refractive lenses*. Journal of Analytical Atomic Spectrometry, 2012. **27**(10): p. 1803-1808.
- G. Buzanich, M. Radtke, U. Reinholz, H. Riesemeier, A. F. Thunemann and C. Strelt, *Impurities in multicrystalline silicon wafers for solar cells detected by synchrotron micro-beam X-ray fluorescence analysis*. Journal of Analytical Atomic Spectrometry, 2012.
- A. Guilherme, G. Buzanich, M. Radtke, U. Reinholz, J. Coroado, J. M. F. Dos Santos, and M. L. Carvalho, *Synchrotron micro-XRF with Compound Refractive Lenses (CRLs) for tracing key elements on Portuguese glazed ceramics*. Journal of Analytical Atomic Spectrometry, 2012. **27**(6): p. 966-974.
- A. Guilherme, G. Buzanich, and M. L. Carvalho, *Focusing systems for the generation of X-ray micro beam: An overview*. Spectrochimica Acta Part B: Atomic Spectroscopy, 2012. **77**(0): p. 1-8.
- I. Ordavo, S. Ihle, V. Arkadiev, O. Scharf, H. Soltau, A. Bjeoumikhov, S. Bjeoumikhova, G. Buzanich, R. Gubzhokov, A. Guenther, R. Hartmann, P. Holl, N. Kimmel, M. Kuehbacher, M. Lang, N. Langhoff, A. Liebel, M. Radtke, U. Reinholz, H. Riesemeier, G. Schaller, F. Schopper, L. Strueder, C. Thamm, and R. Wedell, *A new pnCCD-based color X-ray camera for fast spatial and energy-resolved measurements*. Nuclear Instruments & Methods in Physics Research Section a-Accelerators Spectrometers Detectors and Associated Equipment, 2011. **654**(1): p. 250-257.
- O. Scharf, S. Ihle, I. Ordavo, V. Arkadiev, A. Bjeoumikhov, S. Bjeoumikhova, G. Buzanich, R. Gubzhokov, A. Gunther, R. Hartmann, M. Kuhbacher, M. Lang, N. Langhoff, A. Liebel, M. Radtke, U. Reinholz, H. Riesemeier, H. Soltau, L. Struder, A. F. Thunemann, and R. Wedell, *Compact pnCCD-based X-ray camera with high spatial and energy resolution: A Color X-ray Camera*. Analytical Chemistry, 2011. **83**(7): p. 2532-2538.

and a part has been presented at following conferences:

- G. Buzanich, M. Radtke, U. Reinholz, H. Riesemeier, D. Kreßner-Kiel, T. Kaden, M. Kittler and W. Seifert, *Micro-XANES: A tool for the analysis of copper impurities in photovoltaic polycrystalline silicon*, in 12th Workshop on Progress in Analytical Methodologies for Trace Metal Speciation, TraceSpec 2009 Mainz, Germany.
- G. Buzanich, M. Radtke, U. Reinholz, H. Riesemeier, M. Kittler and W. Seifert, *XBIC, μ RFA und μ XANES an metallischen Verunreinigungen in polykristallinem Solarsilicium*, in Deutsche Tagung für Forschung mit Synchrotronstrahlung, Neutronen und Ionenstrahlen, SNI 2010: Berlin, Germany.
- G. Buzanich, M. Radtke, U. Reinholz, H. Riesemeier, D. Kreßner-Kiel and T. Kaden, , *μ -XRF and μ -XANES, tools for the analysis of metallic impurities in photovoltaic polycrystalline silicon*, in European Conference on X-ray Spectrometry 2010: Figueira da Foz, Coimbra, Portugal.

Partially to the thesis related work appears in following publications:

- C. Grunewald, M. Radtke, U. Reinholz, G. Buzanich, and H. Riesemeier, *SRXRF-measurements at non-planar objects: automatic determination of the angle of incidence of the exciting X-ray*. Journal of Analytical Atomic Spectrometry, 2011. **26**(5): p. 1088-1089.
- T. El-Hasan, W. Szczerba, G. Buzanich, M. Radtke, H. Riesemeier, and M. Kersten, *Cr(VI)/Cr(III) and As(V)/As(III) Ratio Assessments in Jordanian Spent Oil Shale Produced by Aerobic Combustion and Anaerobic Pyrolysis*. Environmental Science & Technology, 2011. **45**(22): p. 9799-9805.
- B. Constantinescu, A. Vasilescu, D. Stan, M. Radtke, U. Reinholz, G. Buzanich, D. Ceccato, and E. Oberlander-Tarnoveanu, *Studies on archaeological gold items found on Romanian territory using X-ray based analytical spectrometry*. Journal of Analytical Atomic Spectrometry, 2012.

and has been presented at following conferences and meetings:

- M. Radtke, G. Buzanich, U. Reinholz, H. Riesemeier, *X-ray Fluorescence analysis using synchrotron radiation excitation*, in 75. Jahrestagung der DPG und DPG Frühjahrstagung 2011: Dresden, Germany.
- A. Bidarra, G. Buzanich, J. Coroado, F. Rocha, *A multianalytical approach to the study of gold leaf from a baroque altarpiece*, in Technart 2011: Berlin, Germany.
- C. Grunewald, G. Buzanich, M. Radtke, U. Reinholz, H. Riesemeier, *SRXRF-measurements at non planar objects: Automatic determination of the angle of incidence of the exciting X-ray*, in Technart 2011: Berlin, Germany.
- A. Guilherme, G. Buzanich, L. Lühl, T. Wolff, M. Radtke, U. Reinholz, J.F. dos Santos, B. Kanngießer, J. Coroado, M.L. Carvalho, *SR-Xanes for the study of portuguese polychrome glazed ceramics: 16th - 19th centuries*, in Technart 2011: Berlin, Germany.
- P. Giere, M. Kuehbacher, O. Scharf, S. Bjeoumikova, R. Gubzhokov, M. Radtke, U. Reinholz, H. Riesemeier, G. Buzanich, R. Wedell, H. Soltau, I. Ordavo and N. Langhoff, *Non-invasive spatial scanning for iron and calcium in the enamel of a red toothed shrew, Sorex araneus (Soricidae, Lipotyphla)*, in 85th Annual Conference of the German Society of Mammalogy 2011: Luxembourg, Luxembourg.
- P. P. Michalak, A. D. Renno, F. Munnik, M. Radtke, G. Buzanich, U. Reinholz, S. Merchel, *Three natural minerals - sanidine, pyrite and columbite - as potential geologic reference materials. Characterization of chemical homogeneity at a micrometer scale*, in European Mineralogical Conference 2012: Frankfurt (M.), Germany.
- P. P. Michalak, A. D. Renno, F. Munnik, M. Radtke, G. Buzanich, U. Reinholz, S. Merchel, *Spatially-resolved analysis of natural minerals as carriers of high-tech metals and Rare Earth Elements: comparison of EPMA, PIXE and Sy- μ XR*, in ICNMTA 2012: Lisbon, Portugal
- G. Buzanich, M. Radtke, U. Reinholz, *Facettenreiche Forschung an der BAMline*, in Lange Nacht der Wissenschaften 2012: Berlin, Germany.
- J. Lingott, H. Riesemeier, U. Reinholz, G. Buzanich, M. Radtke, N. Jakubowski, U. Panne, *Gadolinium-based MRI Contrast Agents in Biological Samples*, in 11th European Workshop on Laser Ablation 2012: Gijón, Spain.

The novel Color X-ray Camera was presented at several conferences as e.g.:

- O. Scharf, M. Radtke, U. Reinholz, H. Riesemeier, G. Buzanich, A. Bjeoumikhov, R. Gubzhokov, R. Wedell, H. Soltau, S. Ihle, I. Ordavo, N. Langhoff, *An Energy-Resolving X-RAY Camera as a novel tool in the full-field X-ray analysis of medical and biological samples*, in SFM 11 Saratov Fall Meeting 2011: Saratov, Russia.
- M. Radtke, O. Scharf, U. Reinholz, H. Riesemeier, G. Buzanich, A. Bjeoumikhov, R. Gubzhokov, R. Wedell, H. Soltau, S. Ihle, I. Ordavo, N. Langhoff, *The colour X-ray camera: Basics, Applications and Perspectives*, in 21st International Congress on X-ray Optics and Microanalysis ICXOM 2011: Campinas, Brazil.
- U. Reinholz, M. Radtke, O. Scharf, H. Riesemeier, G. Buzanich, A. Bjeoumikhov, R. Gubzhokov, R. Wedell, H. Soltau, S. Ihle, I. Ordavo, N. Langhoff, *A novel device for elemental distribution imaging: A color X-ray Camera*, in Jahrestagung der Deutschen Gesellschaft für Biomaterialien (DGBM) 2011: Gießen, Germany.
- O. Scharf, M. Radtke, U. Reinholz, H. Riesemeier, G. Buzanich, A. Bjeoumikhov, R. Gubzhokov, R. Wedell, H. Soltau, S. Ihle, I. Ordavo, N. Langhoff, *Design and measurement with a new portable X-ray camera for full-field fluorescence imaging*, in Denver X-ray conference 2011: Denver, CO, USA.
- O. Scharf, M. Radtke, U. Reinholz, H. Riesemeier, G. Buzanich, A. Bjeoumikhov, R. Gubzhokov, R. Wedell, H. Soltau, S. Ihle, I. Ordavo, N. Langhoff, *The SLcam: A full-field energy dispersive X-ray camera*, in 14th International Workshop on Radiation Imaging Detectors 2012: Figueira da Foz, Coimbra, Portugal.

Acknowledgement

This work would never have been possible without my wife Ana, my parents Helene and Johann, my grandmother Maria, my sister Ulrike and my nephew Daniel, who have supported and encouraged me throughout my studies and the preparation of this thesis.

Special thanks go to my supervisors Christina Strelt and Heinrich Rieseemeier for their guidance and the fruitful discussions. I am very grateful for the confidence they placed in me and the freedom they granted me to conduct my work.

I would like to express my gratitude to my colleagues Martin Radtke and Uwe Reinholz for their help and support with the experiments as well as for the interesting debates on the subject and beyond.

Many other people deserve to be thanked and are mentioned in no particular order:

- from the Federal Institute for Materials Research and Testing (BAM) in Berlin, Oliver Scharf for his support with the Color X-ray Camera as well as Ralf Britzke and Monika Klinger for their technical support at the beamline.
- from the IHP/BTU Joint Lab in Cottbus, Martin Kittler and Winfried Seifert for providing the solar cell fragment and background knowledge about solar cells.
- from the TU Bergakademie in Freiberg, Denise Kreßner-Kiel and Thomas Kaden for sample preparation within the research cluster Solar Valley.
- from the Atomic Physics Centre of the University of Lisbon, Ana Guilherme Buzanich for the ceramic fragments, their data evaluation and discussion.

My sincere thanks go to Simon Arnold for proof reading this work and correcting many orthographical and grammatical mistakes.

The work was financially supported by

- the IHP/BTU Joint Lab, Cottbus for 9 months,
- the German Federal Ministry of Education and Research within the framework of the research cluster Solar Valley Central Germany for 13 months and
- the Federal Institute for Materials Research and Testing for 15 months.

Content

1	Introduction	1
2	Synchrotron Radiation.....	3
2.1	Introduction.....	3
2.2	Radiation from moving charged particles	6
2.2.1	Electromagnetic waves from moving charges.....	6
2.2.2	Radiation from a non-relativistic electron.....	8
2.2.3	Radiation from a relativistic electron	9
2.2.4	The time structure of SR	11
2.2.5	The frequency distribution of SR.....	12
2.2.6	The brightness, flux and brilliance of SR.....	14
2.2.7	The polarization of SR	16
2.3	Synchrotron radiation facilities	17
2.3.1	Wavelength shifters (WLS)	17
2.3.2	Wigglers and Undulators	18
3	Compound Refractive Lens	21
3.1	Introduction.....	21
3.2	Refraction index.....	24
3.3	Theory of a parabolic refractive lens for X-rays.....	26
3.3.1	Focal length of a parabolic refractive lens	27
3.3.2	Derivation of the main parameters of a parabolic CRL	28
3.3.2.1	Ray-tracing method	29
3.3.2.2	Analytical method	31
3.4	Properties of a parabolic compound refractive lens	34
3.4.1	Aberrations.....	34
3.4.2	Transmission and gain	35
3.4.3	Lateral resolution and depth of focus	35
3.4.4	Surface roughness	36
3.4.5	Lens material.....	36
4	Analytical techniques	39
4.1	X-ray fluorescence analysis.....	39
4.1.1	Qualitative and quantitative X-ray fluorescence analysis	39
4.2	X-ray beam induced current.....	42

4.3.1 X-ray absorption	43
4.3.2 X-ray absorption fine structure (XAFS)	45
4.3.2.1 XANES	46
4.3.2.2 EXAFS.....	49
4.3.3 Micro-XRF and micro-XAFS.....	52
5 Experimental setup.....	55
5.1 Berliner Elektronen Speicher SYnchrotron (BESSY).....	55
5.2 BAMline.....	57
5.2.1 The superconducting 7 T wavelength shifter	58
5.2.2 The beam shutter.....	60
5.2.3 The slit system	60
5.2.4 The filter rack.....	60
5.2.4 The double multilayer monochromator.....	61
5.2.4 The double crystal monochromator.....	62
5.3 The imaging setup.....	64
5.4 The X-ray fluorescence setup.....	65
5.5 The Color X-ray Camera	66
6 Characterization of the CRL	69
6.1 Polymeric crossed planar parabolic CRL.....	69
6.2 Alignment of the CRL at the beamline	72
6.3 Focal distances of the lens plate.....	74
6.3.1 Focal length of lens 8t.....	75
6.3.2 Measured focal lengths of lens plate #08-762P-JW13_a	77
6.4 Spot size and spot geometry	80
6.4.1 Influence of the DMM on the spot size.....	80
6.4.2 Changes of the spot geometry due to prefocusing	81
6.4.3 Spot size depending on the energy	82
6.4.4 Spot size for energies much higher than the nominal	84
6.5 Influence of the CRL on the features of XAFS spectra	86
6.6 Conclusions and outlook.....	90
7 Applications.....	91
7.1 Polycrystalline solar cells ^[108].....	93
7.1.1 Theoretical considerations	94
7.1.2 Sample and sample preparation	97

7.1.3 Preliminary investigations.....	98
7.1.4 XBIC and XRF measurements.....	100
7.1.5 Detailed analysis of the Cu precipitates	110
7.2 Portuguese glazed ceramics ^[109]	113
7.2.1 Samples and sample preparation.....	113
7.2.2 Experimental setup.....	114
7.2.3 Results.....	115
7.2.3.1 Blue decorations	115
7.2.3.2 Purple decorations	116
7.2.3.3 Green decorations.....	117
7.2.3.4 Yellow decorations.....	118
7.2.4 Elemental mappings with a Color X-ray Camera (CXC).....	119
7.2.5 Conclusions.....	120
8 Conclusions and Outlook	123
Bibliography.....	127
Appendix.....	135

1 Introduction

When matter is exposed to high-energy X-rays ionization in inner orbitals of atoms may occur, leaving them in an unstable state. Reoccupying these holes with electrons from higher orbital's takes place along with the emission of a photon with an energy equal to the energy difference of the two involved orbitals. The energy of these photons is unique for each element and therefore the phenomenon can be used for elemental analysis. H.G.J. Moseley showed this relation between the wavelength (λ) of the emission lines and the atomic number (Z) of an element in 1913 [1, 2]. Since then X-ray Fluorescence spectrometry (XRF) is used in various scientific fields as a non-destructive and multi-elemental technique allowing to perform not only qualitative but also quantitative analysis of trace elements.

The ionization process is the reason for abrupt raises in the absorption coefficient, which are characteristic for each element and involved orbital as well. These so called absorption edges are fundamental for an area of application called X-ray Absorption Spectroscopy (XAS). A wide variety of methods are available to investigate physical properties such as the electronic structure, the coordination geometry, bond length and angles in molecules. Investigations of the X-ray Absorption Fine Structure (XAFS) provide information about the structure of matter at an atomic scale. For example, with X-ray Absorption Near Edge Structure (XANES) information about the electronic states and coordination geometry is provided, while with Extended X-ray Absorption Fine Structure (EXAFS) information about the bond length and angles of the probed atomic species are obtained.

Some of these methods require a polarized or a monochromatic X-ray beam with high intensity, properties that only Synchrotron Radiation (SR) offers [3, 4]. Synchrotron radiation is electromagnetic radiation emitted from relativistic charged particles, typically electrons, when forced on a curved trajectory by magnetic fields. The outstanding properties of this kind of radiation source like high intensity over a broad spectral range, high brilliance and small divergence of the beam are advantageous for all and even essential for some of the mentioned methods.

Furthermore, to understand certain properties or phenomena of materials, it became necessary to analyze samples with a high lateral or spatial resolution. This lead to a rapid development of optical systems to focus or collimate X-ray beams. Nowadays a variety of X-ray optical systems, based on four physical principles: reflection, diffraction, refraction and absorp-

tion, are available [5, 6]. Taking advantage of the properties of synchrotron radiation (SR), particularly from the so-called third generation storage rings efficient X-ray focusing to beam sizes down to a few nm is possible [7].

The 3rd generation synchrotron source BESSY II in Berlin-Adlershof is due to its high brilliance a suitable source for any kind of X-ray focusing optics. The Federal institute for materials research and testing (BAM) operates a hard X-ray beamline at BESSY II [8] using as radiation source a 7 Tesla WLS (wave length shifter) [9]. For high lateral or spatial resolution measurements a spot size in the μm or sub- μm range is necessary and therefore a Compound Refractive Lens (CRL) with a spot size of about 1 μm was obtained for the *BAMline*. The lenses from the Institute of Microstructure Technology (IMT) Karlsruhe consist of vertical and horizontal stacks of planar parabolic lenses, made out of SU-8 polymer. Sixteen of these lenses are mounted on a Si-wafer, each of them manufactured specifically to match the conditions at the *BAMline* and a certain energy. Preliminary studies [10] of this lenses showed that under optimal conditions a spot size of about 1 μm can be reached. These studies also showed, although only in a very basic way, that μ -XANES and μ -EXAFS should be possible which cannot be taken as granted since focal distance and spot size depend very strong on the energy.

The present work is a study regarding the possibilities to use the CRL with different beam conditions at the *BAMline*, as for example when using the DMM (double multilayer monochromator) instead of the DCM (double crystal monochromator) having a much higher flux but an energy bandwidth of $\frac{\Delta E}{E} = 1.6\%$ instead of $\frac{\Delta E}{E} = 0.02\%$. Furthermore, an extensive study regarding the possibility to use the CRL for X-ray absorption spectroscopy (XAS) was conducted. For these measurements the energy of the incident beam has to be tuned over an energy range from ~ 100 eV below to several 100 eV above the absorption edge of the probed element. To prove that μ -XAS analysis with CRL's is possible, it was investigated how far changes in the energy influence the beam parameters.

2 Synchrotron Radiation

2.1 Introduction

The theoretical basis for the energy loss of charged particles moving with relativistic speed undergoing centripetal acceleration dates back to 1898 when A. Liénard presented a formula showing that the radiated power is proportional to the particle energy E , its rest mass m and the radius of its trajectory R [11]. After G.A. Schott's work from 1912 [12], which included the calculations for frequency and angular distribution for this kind of radiation, there was no further interest in this theory for the next three decades. Only when D.W. Kerst [13, 14] in 1940 started with the construction of high-energy (MeV) accelerators, the power loss due to radiation became an important topic again, because it would limit the "maximal energy attainable in a betatron", as D. Iwanenko and I. Pomeranchuk pointed out in 1944 [15].

Based on these conclusions and taking the operating parameters of the General Electric 100-MeV unit into account [16], J.P. Blewett refined the calculations and found that the theory is in good agreement with the observations they made [17]. Following their assumption, that the wavelength of the emitted radiation should be "between the first thousand or so harmonics", the scientists at GE searched the peak of the radiation in the microwave range but were not able to detect it. While writing the article they found out and mentioned there that, according to the theory of J. Schwinger, they searched the wrong wavelength region.

In 1945 J. Schwinger presented a preprint of his paper "*Electron Radiation in High Energy Accelerators*" to some colleagues, resulting in an invited talk in 1946 at an American Physical Society meeting [18], demonstrating that the radiated energy is in the IR and visible part of the spectra. In 1949 Schwinger published the paper with the title "*On the Classical Radiation of Accelerated Electrons*" [19], presenting a full theory for the radiation loss from an accelerated high energy electron.

Also in 1945 McMillan proposed a machine he called "The synchrotron" [20], meaning a particle accelerator based on the principles of a cyclotron, which by either varying the magnetic field or the frequency could reach energies in the GeV range. He furthermore calculated that the energy loss by radiation should not "seriously" affect the operation of the synchrotron [21].

At the laboratories of General Electric F.R. Elder [22] constructed and built in 1947 a 70 MeV Synchrotron. It was Elder, together with Langmuir R.V. and Pollock H.C. who reported in 1948 the first observation of synchrotron radiation [23] seen through the glass walls of their accelerating tube. They described the light starting as a "dull red spot" at about 30 MeV until a "brilliant bluish-white spot" at an operating energy of 80 MeV. The measurements of the spectral distribution at different energies showed a good agreement with the theory of Schwinger.

The first synchrotron facilities, built as accelerators for high-energy physics, allowed limited access only to the SR for a few experiments to characterize it. Nevertheless, the results gathered from several groups during the next eight years [24-26] increase severely the interest in this radiation. In 1961 the National Bureau of Standards (today: National Institute of Standards and Technology - NIST) decided to modify their 180 MeV synchrotron, allowing the first direct access to the radiation in this case in the UV region. The first synchrotron providing radiation in the hard X-ray region (down to a wavelength of 0.1 Å), was the 6 GeV - Deutsches Elektronen Synchrotron (DESY) in Hamburg, which started operation in 1964.

The next major step on the way to modern synchrotron radiation sources was the development of storage rings, where the beam circulates for a long period continuously in the ring providing amongst other things the possibility of a higher current and hence higher radiation fluxes. In 1953, a high-current synchrotron for particle physics having an additional 240 MeV storage ring to test new accelerator concepts was proposed. In 1968, after a long and turbulent history [27], the Tantalus storage ring became the first reporting a stored electron beam as well as the first facility used only to produce synchrotron radiation.

In the following years, due to its special properties, SR was demanded more and more as radiation source for experiments, leading to the commissioning of beamlines at existing synchrotrons and new storage rings. Beginning of the 1980's facilities dedicated to synchrotron radiation, so-called second generation sources, were built all over the world, as e.g. the National Synchrotron Light Source (NSLS) in Brookhaven in 1981, the Photon Factory in Tsukuba or the Berliner Elektronen Speicher SYNchrotron (BESSY) in Berlin both in 1982.

Some years later, it turned out that for many experiments the spectral brightness (in [photons/sec/mrad²/0.1% bandwidth/mA]) of the light is essential. Since the brightness (or brilliance when divided by the size of the source) of the SR is only dependent on the size and divergence of the electron beam in the storage ring, special care has to be taken in alignment and strength of the magnets who are forming the beam. Already in 1975 Chasman and Green,

working at the Brookhaven National Laboratory, suggested for the arcs of the planned NSLS a lattice out of small achromatic bends [28]. This so-called Chasman-Green lattice is the basis for most of the today's third generation synchrotron sources. The first to go operational was the European Synchrotron Radiation Facility (ESRF) in Grenoble in 1994, followed by the Advanced Photon Source (APS) in Argonne (1996) and Spring-8 in Harima Science Garden City (1997). Next to this large sources, having 30 or more insertion devices, many smaller but therefore less expensive machines were built and are planned all over the world.

The best chance to become the fourth generation source seems to have the Free Electron Laser (FEL), in principle a long undulator in a high-energy linear accelerator, promising a several orders of magnitude higher brilliance than 3rd generation sources.

The superiority of synchrotron radiation over other X-ray sources allowed experiments with high spectral resolution, a necessity for X-ray Absorption Spectroscopy (XAS) or high-resolution crystallography of small crystals and proteins, among others. Nowadays the importance of SR for the improvements in various fields, as e.g. material sciences, arts, geology, biology and medicine, is an incontrovertible fact since its properties make it an ideal X-ray source.

The most important properties of synchrotron radiation are:

- Polarization
- Collimation (divergence in the mrad range)
- High photon intensity
- Time structure (pulse lengths down to 100 ps)
- Broad spectral range (IR to hard X-ray region)
- Small source size (size and divergence of the electron beam)

A more detailed overview on the history of SR can be found in the article "The discovery of synchrotron radiation" from H.C. Pollock (1982) [29].

2.2 Radiation from moving charged particles

In the following only a brief summary on the theory of the synchrotron radiation is given. More detailed information can be found in the original work from J.A. Schwinger [19] and in several books on the topic, as e.g. in the "Handbook on synchrotron radiation" by Koch E. [30], "Synchrotron Radiation" by Wiedemann H. [31] or "Synchrotron radiation: Production and properties" by Duke J.P. [4].

2.2.1 Electromagnetic waves from moving charges

Starting with the Maxwell equations for charges ρ and currents \mathbf{J}

$$\begin{aligned}\nabla \cdot \mathbf{E} &= \frac{\rho}{\varepsilon_0} \quad \text{and} \quad \nabla \cdot \mathbf{B} = 0 \\ \nabla \times \mathbf{E} &= -\frac{\partial \mathbf{B}}{\partial t} \quad \text{and} \quad \nabla \times \mathbf{B} = \mu_0 \left(\mathbf{J} + \varepsilon_0 \frac{\partial \mathbf{E}}{\partial t} \right)\end{aligned}\quad (2.1)$$

and introducing a scalar potential Φ and the vector potential \mathbf{A} for the dynamic case

$$\mathbf{E} = -\nabla\Phi - \frac{\partial \mathbf{A}}{\partial t} \quad \text{and} \quad \mathbf{B} = \nabla \times \mathbf{A} \quad (2.2)$$

the inhomogeneous wave equations are

$$\nabla^2 \Phi - \frac{1}{c^2} \frac{\partial^2 \Phi}{\partial t^2} = -\frac{\rho}{\varepsilon_0} \quad \text{and} \quad \nabla^2 \mathbf{A} - \frac{1}{c^2} \frac{\partial^2 \mathbf{A}}{\partial t^2} = -\mu_0 \mathbf{J} \quad (2.3)$$

$$\text{with } \mu_0 = \frac{1}{\varepsilon_0 c^2} \quad (2.4)$$

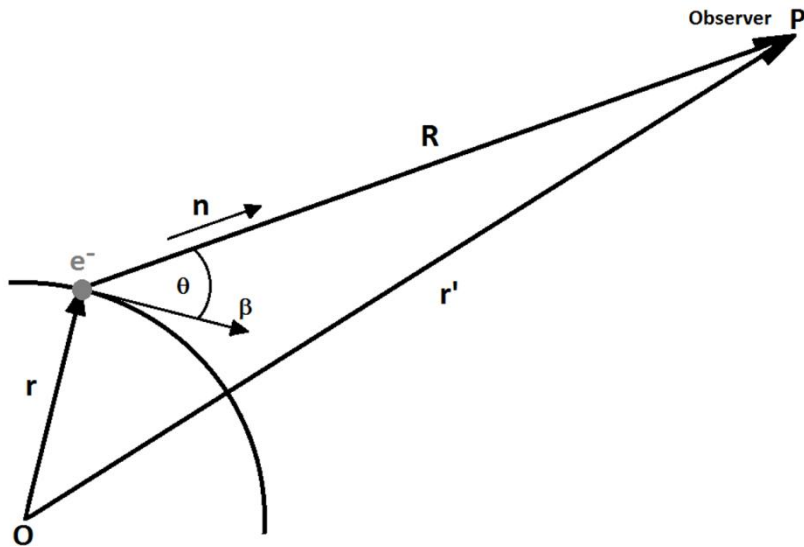


Figure 2.1 Sketch of a moving electron and an observer in P.

Figure 2.1 indicates the geometric relationship between an electron moving on a trajectory with radius \mathbf{r} and an observer in point P . Where \mathbf{R} is the vector from the electron to the observer, with R being the length and \mathbf{n} the unit vector of \mathbf{R} and $\boldsymbol{\beta}$ is the normalized electron velocity defined as

$$\mathbf{R} = \mathbf{r}' - \mathbf{r} \quad \text{and} \quad \mathbf{n} = \frac{\mathbf{R}}{|\mathbf{R}|} \quad \text{and} \quad \boldsymbol{\beta} = \frac{\mathbf{v}}{c} \quad \text{and} \quad \gamma = \frac{1}{\sqrt{1-\beta^2}}$$

Since the observer in P sees the distribution of charge not as it is at the moment, but like it was at an earlier time, the so called retarded time

$$\frac{dt}{dt'} = 1 + \frac{1}{c} \frac{dR(t')}{dx} = 1 - \mathbf{n} \cdot \boldsymbol{\beta} \quad \text{and} \quad t = t' + \frac{R(t')}{c} \quad (2.5)$$

has to be taken into account to calculate the potentials.

Using the localized charge and current densities of a single electron

$$\rho(\mathbf{x}, t) = e \delta^{(3)}(\mathbf{x} - \mathbf{r}(t)) \quad \text{and} \quad \mathbf{J}(\mathbf{x}, t) = e \mathbf{v}(t) \delta^{(3)}(\mathbf{x} - \mathbf{r}(t)) \quad (2.6)$$

the inhomogeneous wave equations have as solution the so called Liénard-Wichert potentials

$$\Phi(\mathbf{x}, t) = \frac{1}{4\pi\epsilon_0} \left[\frac{e}{(1-\mathbf{n}\cdot\boldsymbol{\beta})R} \right]_{\text{ret}} \quad \text{and} \quad \mathbf{A}(\mathbf{x}, t) = \frac{\mu_0}{4\pi} \left[\frac{e\boldsymbol{\beta}}{(1-\mathbf{n}\cdot\boldsymbol{\beta})R} \right]_{\text{ret}} \quad (2.7)$$

where the index *ret* means that the expression has to be calculated with the retarded time.

Inserting these potentials into (2.2) leads to equations for the electric and magnetic fields called Liénard-Wichert fields

$$\mathbf{E}(\mathbf{x}, t) = \frac{e}{4\pi\epsilon_0} \left[\left(\frac{\mathbf{n}-\boldsymbol{\beta}}{\gamma^2(1-\mathbf{n}\cdot\boldsymbol{\beta})^3 R^2} \right) + \frac{1}{c} \left(\frac{\mathbf{n} \times (\mathbf{n}-\boldsymbol{\beta}) \times \dot{\boldsymbol{\beta}}}{(1-\mathbf{n}\cdot\boldsymbol{\beta})^3 R} \right) \right]_{\text{ret}} \quad (2.8a)$$

$$\mathbf{B}(\mathbf{x}, t) = \frac{1}{c} [\mathbf{n} \times \mathbf{E}(\mathbf{x}, t)]_{\text{ret}} \quad (2.8b)$$

It is evident that \mathbf{E} and \mathbf{B} are coupled together, as well as normal to the radius vector \mathbf{r} and normal to each other. Furthermore, it is obvious that the expressions consist of two terms, where the first depends on the velocity $\boldsymbol{\beta}$ (velocity field) and the second on the acceleration $\dot{\boldsymbol{\beta}}$ (acceleration field).

The power radiated from a moving electron observed at the point P at a distance of R from the charge is

$$\frac{d^2P}{d\Omega} = R^2 [\mathbf{S} \cdot \mathbf{n}] \left(\frac{dt}{dt'} \right) = R^2 (\mathbf{S} \cdot \mathbf{n}) (1 - \mathbf{n} \cdot \boldsymbol{\beta}) \quad (2.9)$$

where \mathbf{S} is the so-called Poynting vector.

$$\mathbf{S} = \frac{\mathbf{E} \times \mathbf{B}}{\mu_0} = \frac{1}{\mu_0 c} |\mathbf{E}|^2 \mathbf{n} = \varepsilon_0 c |\mathbf{E}|^2 \mathbf{n}. \quad (2.10)$$

For large distances between the observer and the moving charge, the second term of the equations (2.8) dominates, since it decreases linear with R while the second term decreases by the square of R .

For further calculations it will be assumed that $R \gg 1$ and the velocity term of the equations (2.9) will be neglected (indicated by the index ac).

2.2.2 Radiation from a non-relativistic electron

Leaving aside the velocity field and having the electron moving at a velocity much lower than the speed of light ($v \ll c \rightarrow \boldsymbol{\beta} \approx \vec{0}$) the Liénard-Wichert fields reduce to

$$\mathbf{E}_{ac}(\mathbf{x}, t) = \frac{e}{4\pi\varepsilon_0 c} \left[\frac{\mathbf{n} \times (\mathbf{n} \times \dot{\boldsymbol{\beta}})}{R} \right]_{\text{ret}} \quad (2.11)$$

and the radiated power is

$$\frac{d^2 P}{d\Omega} = R^2 (\mathbf{S} \cdot \mathbf{n}) = \varepsilon_0 c |R \mathbf{E}_{ac}|^2 = \frac{e^2}{(4\pi)^2 \varepsilon_0 c} |\mathbf{n} \times (\mathbf{n} \times \dot{\boldsymbol{\beta}})|^2 \quad (2.12)$$

Using θ , the angle between the unit vector of \mathbf{R} the acceleration $\dot{\boldsymbol{\beta}}$ as indicated in fig. 2.2, the equation can be rewritten as

$$\frac{d^2 P}{d\Omega} = \frac{e^2}{(4\pi)^2 \varepsilon_0 c} |\dot{\boldsymbol{\beta}}|^2 \sin^2 \theta \quad (2.13)$$

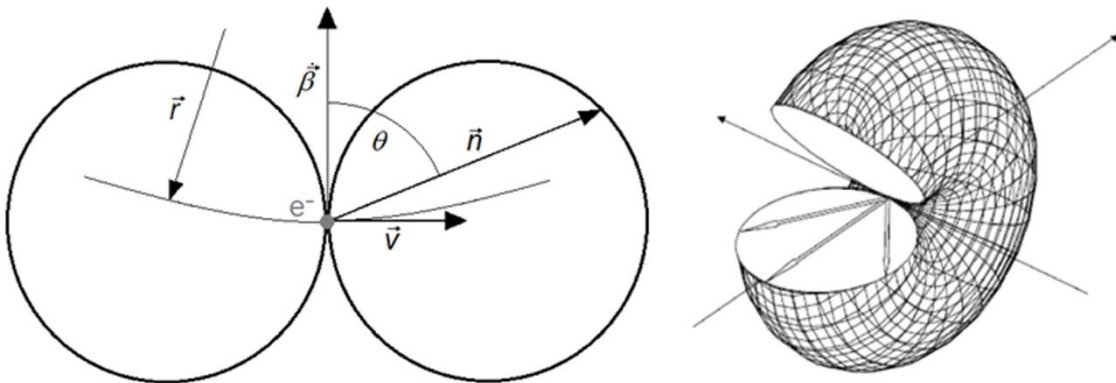


Figure 2.2 Sketch of the radiation emission pattern in the $\boldsymbol{\beta}$ - \mathbf{v} -plane on the left and the 3 dimensional distribution on the right (3D-sketch from [31])

Figure 2.2 shows on the left a sketch of a non-relativistic moving electron in his reference system. The spatial distribution of the radiation emission as shown on the right corresponds to that of a Hertz dipole and is the result of the φ rotation around $\dot{\boldsymbol{\beta}}$.

Integrating equation (2.13) over the whole solid angle 4π with ($d\Omega = \sin\theta d\theta d\varphi$), gives the total amount of power radiated by a non-relativistic electron as

$$P = \frac{e^2}{6\pi\epsilon_0 c} |\dot{\boldsymbol{\beta}}|^2 \quad (2.14)$$

Equation (2.14) is also known as Larmor formula.

2.2.3 Radiation from a relativistic electron

Having the electron moving at a velocity near the speed of light ($v \sim c$) and neglecting again the velocity field, the Liénard-Wichert fields reduce to

$$\mathbf{E}_{ac}(\mathbf{x}, t) = \frac{e}{4\pi\epsilon_0 c} \left[\frac{\mathbf{n} \times (\mathbf{n} - \boldsymbol{\beta}) \times \dot{\boldsymbol{\beta}}}{(1 - \mathbf{n} \cdot \boldsymbol{\beta})^3 R} \right]_{\text{ret}} \quad (2.15)$$

and the radiated power is calculated by

$$\frac{d^2 P}{d\Omega} = \epsilon_0 c |R \mathbf{E}_{ac}|^2 = \frac{e^2}{(4\pi)^2 \epsilon_0 c} \frac{|\mathbf{n} \times [(\mathbf{n} - \boldsymbol{\beta}) \times \dot{\boldsymbol{\beta}}]|^2}{(1 - \mathbf{n} \cdot \boldsymbol{\beta})^5} \quad (2.16)$$

and the integration over 4π gives the power radiated by a relativistic electron as

$$P = \frac{e^2}{6\pi\epsilon_0 c} \gamma^6 \left[\dot{\boldsymbol{\beta}}^2 - (\boldsymbol{\beta} \times \dot{\boldsymbol{\beta}})^2 \right] \quad (2.17)$$

The dominating factor in equation (2.15) is $(1 - \mathbf{n} \cdot \boldsymbol{\beta})^5 = (1 - \beta \cos\theta)^5$, which for ($|\boldsymbol{\beta}| \rightarrow 1$) leads to a emission pattern strongly collimated in the direction of $\boldsymbol{\beta}$ (figures 2.3 and 2.4)

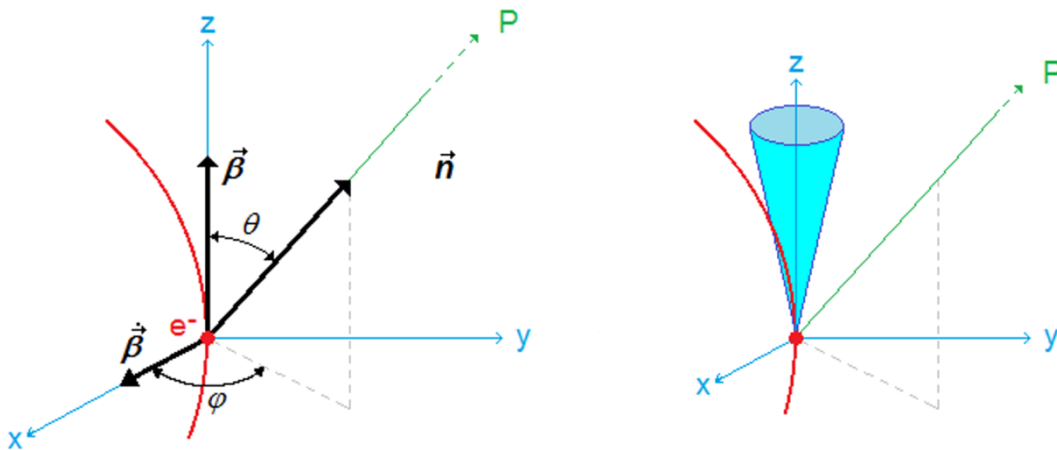


Figure 2.3 Coordinate system of an electron on a circular orbit (left) and the emission pattern (right) in the laboratory frame. The angles θ and φ define the direction of observation.

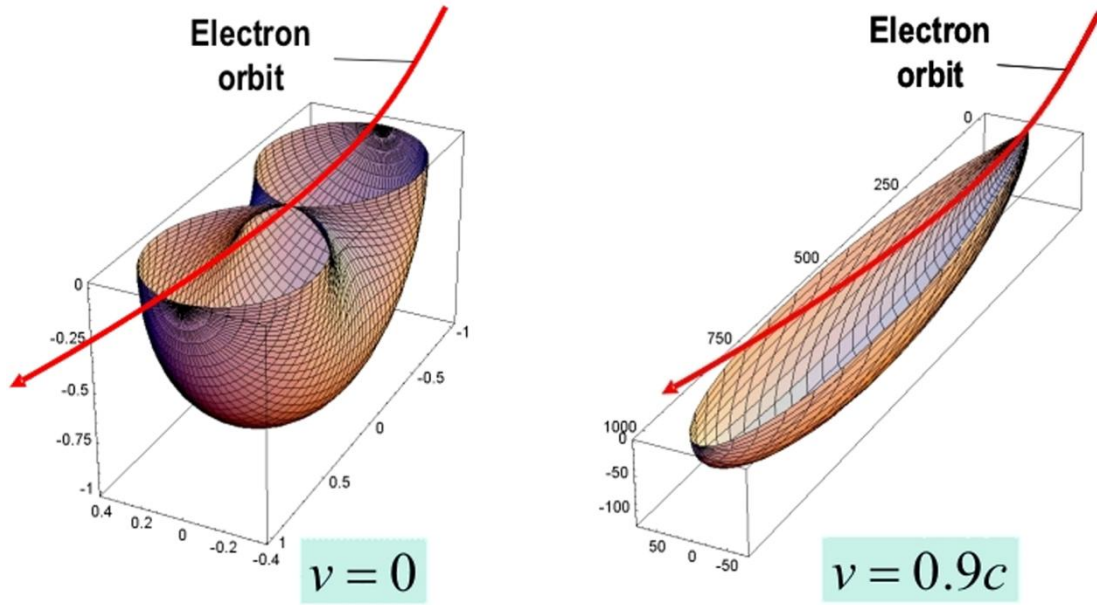


Figure 2.4 3D-sketch from the radiation pattern emitted by an electron moving at non-relativistic (left) and relativistic speed (right).

For an electron at a circular orbit it applies, that at all times $\boldsymbol{\beta} \perp \dot{\boldsymbol{\beta}}$, hence the radiated power is

$$\frac{d^2P}{d\Omega} = \frac{e^2}{(4\pi)^2 \epsilon_0 c} \frac{|\dot{\boldsymbol{\beta}}|^2}{(1-\beta \cos \theta)^3} \left[1 - \frac{\sin^2 \theta \cos^2 \varphi}{\gamma^2 (1-\beta \cos \theta)^2} \right] \quad (2.18)$$

Applying the small angle approximation for θ

$$(1 - \beta \cos \theta) \approx \frac{1}{2\gamma^2} (1 + \gamma^2 \theta^2) \quad \text{and} \quad \sin^2 \theta \approx \theta^2 \quad (2.19)$$

gives for the radiated power

$$\frac{d^2P}{d\Omega} = \frac{e^2}{(4\pi)^2 \epsilon_0 c} \frac{8\gamma^6 |\dot{\boldsymbol{\beta}}|^2}{(1+\gamma^2 \theta^2)^3} \left[1 - \frac{4\gamma^2 \theta^2 \cos^2 \varphi}{(1+\gamma^2 \theta^2)^2} \right] \quad (2.20)$$

showing that $(\gamma\theta)$ is the important parameter for the angular distribution.

Therefore it is not a big surprise that calculating the mean square value $\langle \theta \rangle^2$ (the mean angle between the direction of emission and $\boldsymbol{\beta}$) gives

$$\langle \theta \rangle^2 = \frac{1}{\gamma^2} \quad (2.21)$$

as characteristic opening angle for synchrotron radiation.

Integrating equation (2.18) over the whole solid angle 4π and using $|\dot{\boldsymbol{\beta}}|^2 = \frac{|\dot{\boldsymbol{v}}|^2}{c^2}$ with $|\dot{\boldsymbol{v}}| = \frac{v^2}{r}$ and $\dot{\boldsymbol{v}} = \frac{1}{\gamma m_0} \frac{d\boldsymbol{p}}{dt}$, gives the total amount of power radiated by one relativistic electron as

$$P = \frac{e^2}{6\pi\epsilon_0 c} |\dot{\boldsymbol{\beta}}|^2 \gamma^4 = \frac{e^2 c}{6\pi\epsilon_0} \frac{\beta^4}{r^2} \gamma^4 = \frac{e^2}{6\pi\epsilon_0 m_0^2 c^3} \left| \frac{d\boldsymbol{p}}{dt} \right|^2 \gamma^2 \quad (2.22)$$

Taking as an example a bending magnet ($\boldsymbol{E} = \vec{\mathbf{0}}$ and $\boldsymbol{B} \perp \boldsymbol{v}$) to accelerate the electron the Lorentz equation

$$\left| \frac{d\boldsymbol{p}}{dt} \right| = \left| e \left(\boldsymbol{E} + \frac{\boldsymbol{v} \times \boldsymbol{B}}{c} \right) \right| = \frac{evB}{c} \quad (2.23)$$

and the energy of the electron $E = \gamma m_0 c^2$ can be used to calculate the radiated power as

$$P = \frac{e^4 \beta^2}{6\pi\epsilon_0 m_0^4 c^5} E^2 B^2 \quad (2.24)$$

Equation (2.22) shows that the radiated power is proportional to the bending radius ($\frac{1}{r^2}$), and (2.24) shows the dependency on different factors like the magnetic field (B^2) or the rest mass of the particle ($\frac{1}{m_0^4}$).

Comparing the rest mass of an electron with the one of a proton

$$m_e c^2 = 0.511 \text{ MeV} \quad \text{to} \quad m_p c^2 = 938.3 \text{ MeV} \quad (2.25)$$

and calculating the quotient of the radiated power for them under the same conditions (E and B) gives

$$\frac{P_e}{P_p} = \left(\frac{m_e c^2}{m_p c^2} \right)^4 = 1.13 \cdot 10^{13} \quad (2.26)$$

which clearly shows the advantages when using electrons.

2.2.4 The time structure of SR

Figure 2.5 shows a part of the trajectory of an electron moving at relativistic speed βc at a circular orbit with radius \boldsymbol{R} . Due to the strong forward collimation with a cone angle of θ , an observer at point P only sees photons emitted between the points **A** and **B** of the trajectory, hence only a short pulse of radiation. The length of the pulse equals the time difference between the first (emitted at **A**), and the last (emitted at **B**), photons arriving at P.

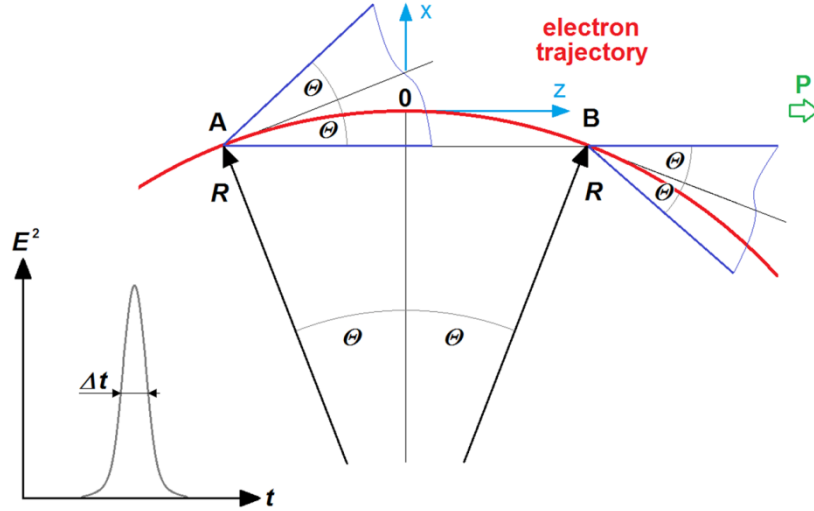


Figure 2.5 Origin of the time structure of synchrotron radiation

Taking into account the additional distance \overline{AB} the photon emitted at **A** has to travel this gives

$$\Delta t = t_B - t_A = \frac{2R\theta}{\beta c} - \frac{2R \sin \theta}{c} \quad (2.27)$$

with $\sin \theta = \theta - \frac{\theta^3}{3!}$ (suitable for small angles θ) and equation (2.21) follows

$$\Delta t = \frac{2R}{c} \left(\frac{1}{\gamma\beta} - \frac{1}{\gamma} + \frac{1}{6\gamma^3} \right) \approx \frac{4R}{3c\gamma^3} \quad \text{with} \quad \frac{1}{\gamma\beta} \approx \frac{1}{\gamma} + \frac{1}{2\gamma^3} \quad (2.28)$$

The frequency spectrum is obtained by a Fourier transformation and gives a typical frequency of

$$\omega_{typ} = \frac{2\pi}{\Delta t} = \frac{3\pi c \gamma^3}{2R} \quad (2.29)$$

with the critical frequency defined as

$$\omega_c = \frac{\omega_{typ}}{\pi} = \frac{3c\gamma^3}{2R} = \frac{3}{2}\gamma^3\omega_0 \quad (2.30)$$

where $\omega_0 = \frac{c}{R}$ is the angular frequency from the rotation of the electron.

The critical frequency divides the radiations frequency spectrum in two regions with equal power and equation (2.30) furthermore shows that a relativistic particle emits at a broad range of frequencies.

2.2.5 The frequency distribution of SR

The calculation of the frequency spectrum was first done by J. Schwinger [19] and can also be found in various book about synchrotron radiation or electrodynamics (e.g. [4]).

For the case of an electron in the field of a bending magnet, hence the electron trajectory is an arc of a circle, and under the assumptions that the observer is far from the source so that the velocity field can be neglected the frequency and angular distribution of the energy is

$$\frac{d^3I}{d\Omega d\omega} = \frac{e^2}{16\pi^3 \epsilon_0 c} \left(\frac{2\omega R}{3c\gamma^2} \right)^2 (1 + \gamma^2 \theta^2)^2 \left[K_{2/3}^2(\xi) + \frac{\gamma^2 \theta^2}{1 + \gamma^2 \theta^2} K_{1/3}^2(\xi) \right] \quad (2.31)$$

$$\text{with } \xi = \frac{\omega R}{3c\gamma^3} (1 + \gamma^2 \theta^2)^{3/2} \quad (2.32)$$

and the modified Bessel functions $K_{2/3}(\xi)$, corresponding to the radiation polarized in the orbital plane, and $K_{1/3}(\xi)$ corresponding to the one perpendicular to that plane.

The most important conclusions from these calculations are, that:

- the radiation intensity is negligible for large angles θ .
- the radiation is mainly restricted to the plane of motion (forward collimation)
- by increasing the frequency ω the critical angle θ_c decreases,

The critical angle, defined as the angle beyond which the radiation is negligible, is:

$$\theta_c = \frac{1}{\gamma} \left(\frac{\omega_c}{\omega} \right)^{1/3} \quad (2.33)$$

Integrating equation (2.31) over the whole solid angle gives

$$\frac{dI}{d\omega} = \frac{\sqrt{3}e^2}{4\pi\epsilon_0 c} \gamma \frac{\omega}{\omega_c} \int_{\omega/\omega_c}^{\infty} K_{5/3}(x) dx \quad (2.34)$$

and building the limit for low- an high-frequencies gives

$$\frac{dI}{d\omega} \approx \frac{e^2}{4\pi\epsilon_0 c} \left(\frac{\omega R}{c} \right)^{1/3} \quad \text{for } \omega \ll \omega_c \quad (2.35)$$

$$\frac{dI}{d\omega} \approx \sqrt{\frac{3\pi}{2}} \frac{e^2}{4\pi\epsilon_0 c} \left(\frac{\omega}{\omega_c} \right)^{1/2} e^{-\omega/\omega_c} \quad \text{for } \omega \gg \omega_c \quad (2.36)$$

A universal distribution, only dependent on the critical frequency and the mathematical Bessel functions but not on the actual particle energy, is achieved by normalizing $\frac{dI}{d\omega}$ to the critical frequency

$$S(\omega/\omega_c) = \frac{9\sqrt{3}}{8\pi} \frac{\omega}{\omega_c} \int_{\omega/\omega_c}^{\infty} K_{5/3}(x) dx \quad (2.37)$$

with the conditions

$$\int_0^{\infty} S(x) dx = 1 \quad \text{and} \quad \int_0^1 S(x) dx = \frac{1}{2} \quad (2.38)$$

which show that the critical frequency divides the spectrum in two parts of equal power.

Figure 2.6 shows the universal function with $x = \frac{\omega}{\omega_c}$ and indicated low-frequency (red) and high-frequency (blue) limits.

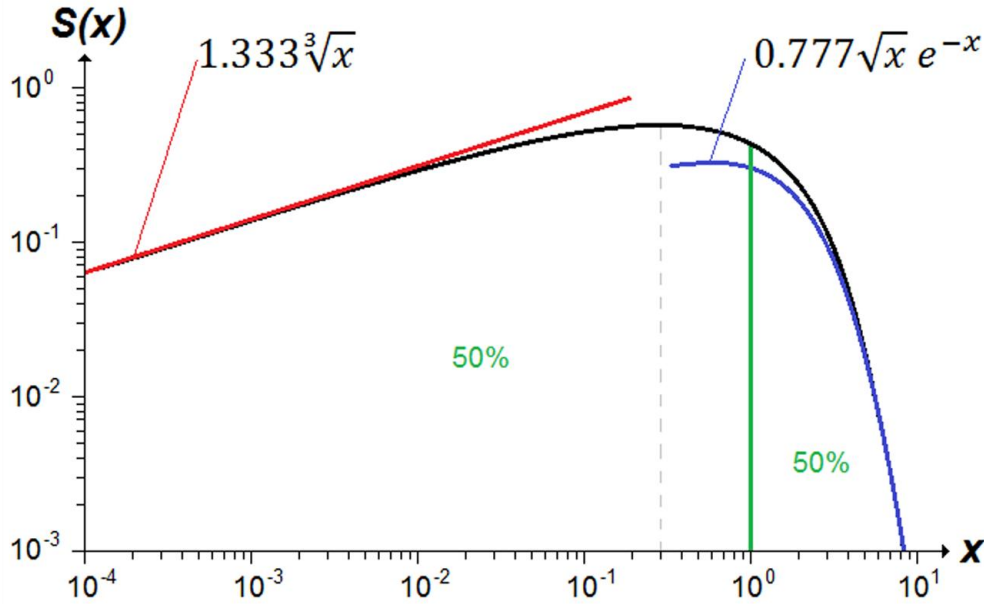


Figure 2.6 Normalized universal function $S(\omega/\omega_c)$ of the synchrotron radiation spectrum.

The peak of $S(x)$ is at about $x = 0.3$ and the green line at the critical frequency divides the area under the curve in equal parts.

2.2.6 The brightness, flux and brilliance of SR

Defining the critical energy and the critical wavelength and calculate them using practical units leads for electrons to

$$\varepsilon_c = \hbar\omega_c = \frac{3}{2} \frac{\hbar c}{R} \gamma^3 \approx 2.218 \frac{E^3}{R} = 0.665 E^2 B \quad (2.39)$$

$$\lambda_c = \frac{2\pi c}{\omega_c} = \frac{4\pi}{3} \frac{R}{\gamma^3} \approx 5.59 \frac{R}{E^3} = 18.6 \frac{1}{E^2 B} \quad (2.40)$$

with ε_c in [keV], λ_c in Ångström, R in meters, E in [GeV] and B in Tesla.

Up to now the calculations are for a single electron only. In the case of a particle beam the total radiated power is proportional to the number of electrons that pass the observer. With I_b

in [A] being the average current of the beam, the radiated power per second in [W] can be calculated by

$$\frac{d^3P}{d\Omega d\omega} = \frac{d^3I}{d\Omega d\omega} \frac{I_b}{e} \quad (2.41)$$

and by using the practical units and the photon energy ε in [eV] this becomes

$$\begin{aligned} \frac{d^3P}{d\Omega d\omega} = 2.124 \cdot 10^{-3} E^2 I_b \left(\frac{\varepsilon}{\varepsilon_c}\right)^2 (1 + \gamma^2 \theta^2)^2 \cdot \\ \cdot \left[K_{2/3}^2(\xi) + \frac{\gamma^2 \theta^2}{1 + \gamma^2 \theta^2} K_{1/3}^2(\xi) \right] \end{aligned} \quad (2.42)$$

$$\text{with } \xi = \frac{\omega R}{3c\gamma^3} (1 + \gamma^2 \theta^2)^{3/2} \quad \text{and} \quad \frac{\omega R}{3c\gamma^3} = \frac{\omega}{2\omega_c} = \frac{\varepsilon}{2\varepsilon_c} = \frac{\lambda_c}{2\lambda} \quad (2.43)$$

Another way to express the synchrotron intensity is the by the so called "spectral brightness", the number of photons emitted per second, per 1 mrad² solid angle, per 0.1 % bandwidth and per mA

$$\begin{aligned} \frac{d^4N}{dt d\Omega d\lambda} = 3.46 \cdot 10^3 \gamma^2 \left(\frac{\lambda_c}{\lambda}\right)^2 (1 + \gamma^2 \theta^2)^2 \cdot \\ \cdot \left[K_{2/3}^2(\xi) + \frac{\gamma^2 \theta^2}{1 + \gamma^2 \theta^2} K_{1/3}^2(\xi) \right] \end{aligned} \quad (2.44)$$

which in the orbital plane ($\theta = 0$) at the critical wavelength ($\lambda = \lambda_c \Rightarrow \xi = \frac{1}{2}$) is

$$\left[\frac{d^4N}{dt d\Omega d\lambda} \right]_{\theta=0, \lambda=\lambda_c} = 5.04 \cdot 10^3 \gamma^2 \quad (2.45)$$

When (2.44) is integrated over all angles the so called "spectral flux" in photons per second, per unit bandwidth and per mA beam current is obtained. Integrating this over all wavelengths, leads to the "total flux" in photons per second and per mA beam current.

Since the trajectories of the electrons in storage rings show some aberration from the ideal circular orbit, the size and angular spread of the electron beam has to be taken into account. This leads to another characteristic value for a radiation source called "spectral brilliance", defined as the brightness divided by the source size S (e.g. electron beam cross section)

$$\frac{d^5N}{dt d\Omega dS d\lambda} \quad (2.46)$$

in [photons/sec/mrad²/mm²/0.1% bandwidth/mA].

2.2.7 The polarization of SR

As mentioned above, the modified Bessel functions in (2.31) can be associated with the polarization parallel (P) and normal (N) to the orbit plane. Defining P_l as the degree of linear polarization, with I_P and I_N being the intensities of the two polarization directions, it can be written as

$$P_l = \frac{I_P - I_N}{I_P + I_N} = \frac{K_{2/3}^2(\xi) - \frac{\gamma^2 \theta^2}{1 + \gamma^2 \theta^2} K_{1/3}^2(\xi)}{K_{2/3}^2(\xi) + \frac{\gamma^2 \theta^2}{1 + \gamma^2 \theta^2} K_{1/3}^2(\xi)} \quad (2.47)$$

It is obvious that P_l depends on the angle θ (angle between orbital plane and observer) and that for ($\theta = 0$) follows that $P_l = 1$ and $I_N = 0$, meaning that in the orbital plane the emitted radiation is entirely linear polarized.

2.3 Synchrotron radiation facilities

The main devices of a synchrotron source are an electron gun, a primary accelerator, a booster ring (the synchrotron), a storage ring, the beam lines and the experimental workstations. The electron gun consists typically of a tungsten plate (anode), heated to a temperature above 1000°C , where valence electrons are released and accelerated to the cathode. After the electrons leave the electron gun with an energy in the order of 100keV ($v_{[100\text{keV}]} \approx 0.548 c$), they are injected into the primary accelerator, typically a Linear Accelerator (LINAC) or a microtron, and accelerated to an energy of several tens to hundreds of MeV ($v_{[100\text{MeV}]} \approx 0.999\,987 c$). With this energy the electrons enter the synchrotron where they are further accelerated until they reach energies in the GeV region ($v_{[1\text{GeV}]} \approx 0.999\,999\,869 c$) and afterwards are injected into the storage ring where they are kept on a circular orbit for several hours. To accomplish this, a synchrotron storage ring needs to consist of several devices, the most important are dipole (bending) magnets to force the beam on the circular orbit and produce SR, quadrupole and sextupole magnets to stabilize and focus the electron beam and radio frequency (RF) cavities to compensate the energy loss due to the emitted radiation.

Second and third generation synchrotrons have, beside of the above mentioned elements, specially designed sections to setup so-called insertion devices. These are magnetic structures designed to produce SR with a different characteristic than the one emitted by bending magnets. The most common of these devices and their properties are described briefly in the following sections.

2.3.1 Wavelength shifters (WLS)

These are devices used to shift the emitted spectrum, radiated from electrons with moderate energies, to higher energies in comparison to the spectral distribution when using a bending magnet (see figure 2.7). To accomplish this, the electron beam passes a linear array of three dipole magnets with alternating field directions. The radiation is emitted at the central dipole of the wavelength shifter. The other two dipoles only compensate the deflection of the electron beam from its orbit (see figure 2.7 upper right corner), so that the electrons leave the device in the same direction as they entered. For the production of hard X-rays a strong magnetic field in the order of several Tesla is necessary which is why the dipoles of wavelength shifters are usually made of superconducting magnets.

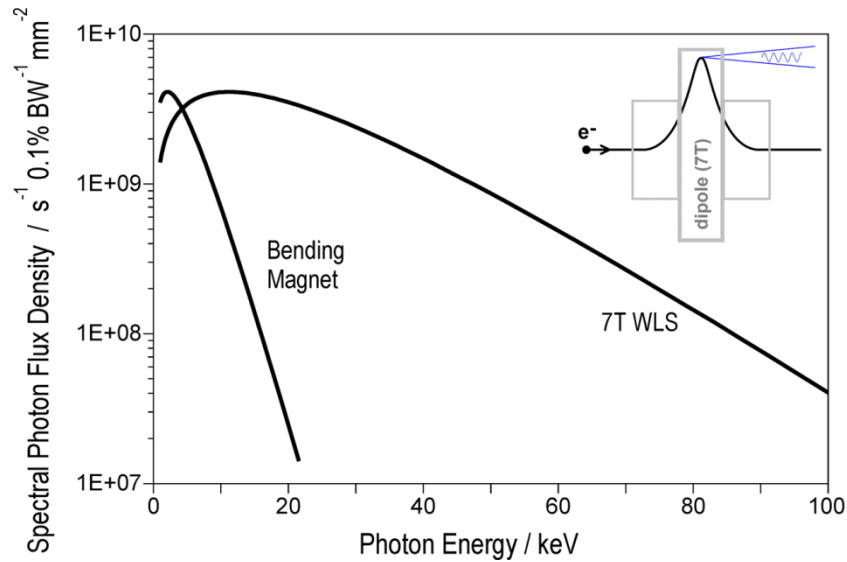


Figure 2.7 Spectral Photon Flux of a 1.3T bending magnet and a 7T wavelength shifter (adapted from [8]). In the upper right corner, a schematic view of the electron trajectory in a WLS is shown.

2.3.2 Wigglers and Undulators

Wigglers and undulators work at the same principle as wavelength shifters, but instead of only three there are many dipole magnets with alternating field directions aligned. The strength of the magnetic fields is the same for all center dipoles forcing the electron beam on a sinusoidal trajectory within the device. Again, the first and the last dipole in the device only compensate the deflection of the electron beam, with respect to the geometry of the beam path through the storage ring. All other dipoles are sources of SR producing a short pulse of radiation, which when superimposed lead to an increase in the photon flux by a factor of N , when $(N + 2)$ is the total number of dipoles in the device.

An important parameter characterizing the electron motion is the deflection parameter K , which is defined as

$$K = \frac{eB_0\lambda_0}{2\pi mc} \quad (2.48)$$

where B_0 is the magnetic field of the dipoles and λ_0 the magnetic period, defined as the distance between two neighboring dipoles having their magnetic field in the same direction (see figure 2.8).

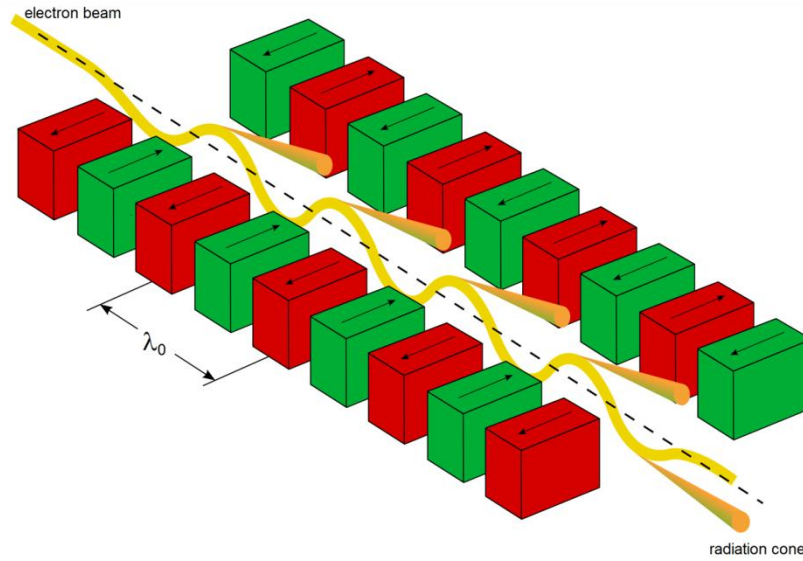


Figure 2.8 Principle of multipole wiggler or undulator devices (source [32])

Knowing the deflection parameter, the maximum deflection angle of the beam is given by

$$\delta = \frac{K}{\gamma} \quad (2.49)$$

To distinguish between wiggler and undulators the K parameter is used so that one speaks of an undulator for K smaller than 1 and of a wiggler when K is much bigger than 1.

For wigglers ($K \gg 1$), which is the case for strong magnetic fields B_0 and long magnetic periods λ_0 , the superimposition of the radiation is incoherent and the spectral distribution is similar to the one of a WLS (see figure 2.9).

In undulators ($K \leq 1$), which have weaker fields and shorter magnetic periods, the deflection angle is smaller than the opening angle of the synchrotron radiation and therefore the emitted radiation is coherent superimposed. Due to this strong interference the spectral distribution shows sharp peaks with discrete wavelength dependent on θ , the angle between the observation direction and the z -axis

$$\lambda = \frac{\lambda_0}{2j\gamma^2} \left(1 + \frac{1}{2}K^2 + \gamma^2\theta^2 \right) \quad \text{with } j = 1, 2, 3, \dots \quad (2.50)$$

Figure 2.9 shows the brilliance of different undulator beamlines at third generation synchrotron sources compared with free electron lasers.

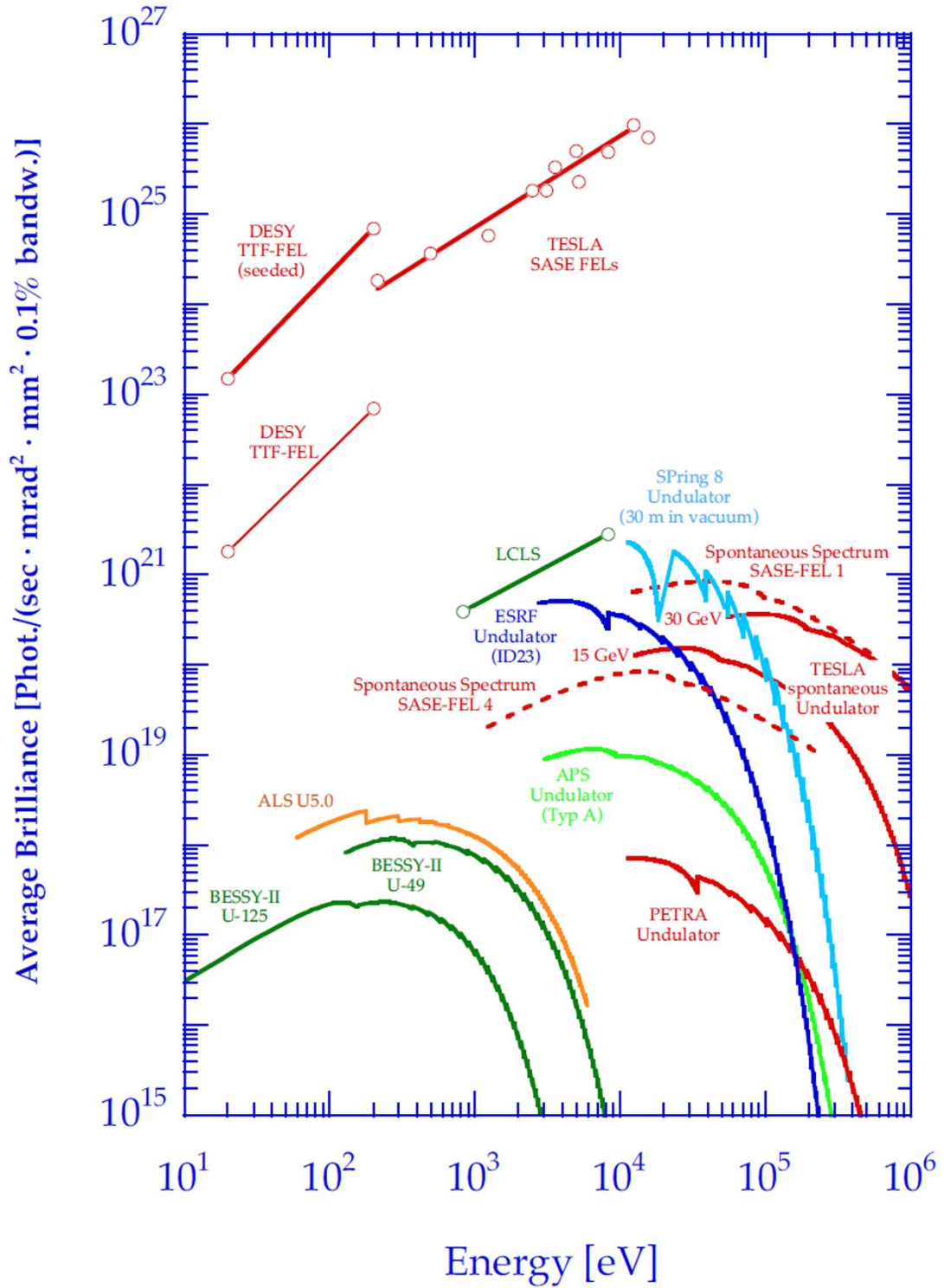


Figure 2.9 Average brilliance of undulator beamlines from different synchrotron radiation sources and of free electron lasers (FELs) (source [33])

3 Compound Refractive Lens

3.1 Introduction

Analyzing samples with a high lateral or spatial resolution is necessary to help understand certain properties or phenomena. Due to the growing interest in high-resolution imaging, a fast development in X-ray optics has emerged, hence the field of X-ray optics has grown enormously in the past decades [7, 34]. Nowadays the developments in focusing X-ray optical systems provide appropriate beam sizes for almost every requirement.

The unique properties of synchrotron radiation, as described in Chapter 2, particularly the high brilliance and coherence, allow even more efficient X-ray focusing. Especially at third generation storage rings, it is possible to focus X-rays from a broad energy range with the respective optical device to a beam size in the nm region [35, 36].

Focusing X-ray optical systems can be divided by the three physical principles: reflection, diffraction and refraction. The most common optical devices based on this three principles are described in detail in various books and articles as e.g. in [5]. Furthermore there are a number of different devices within each class, a good overview not claiming to be complete can be found at [37], each one having advantages and disadvantages.

Reflective optics work under the principle of total external reflection, meaning that X-rays, which hit a surface under an angle smaller than the critical angle θ_C , are reflected from the surface. The critical angle θ_C only depends on the refraction decrement δ of the mirror material given by Snell's law:

$$\theta_C = \sqrt{2\delta} \quad (3.1)$$

The most common optics in this category are Kirkpatrick-Baez mirrors [38] and capillaries, mostly polycapillary optics, also known as Kumakhov lenses [39]. Since polycapillaries are practically the only feasible optics to be used with an X-ray tube they are widely used in laboratory devices while K-B mirrors are mainly used at synchrotron radiation sources.

A diffractive optics works under the principle of Bragg's law, given by:

$$n\lambda = 2d \sin \theta \quad (3.2)$$

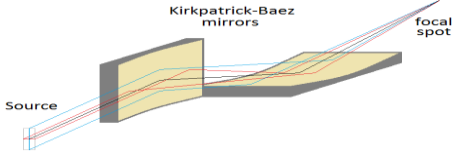
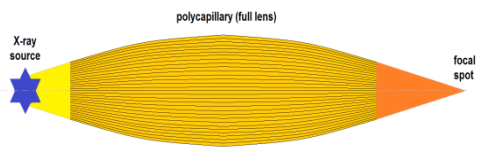
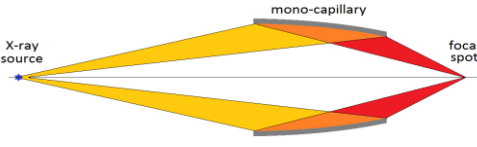
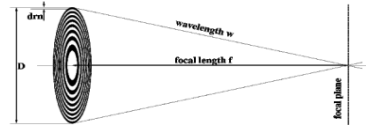


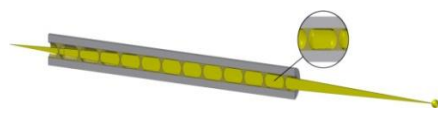
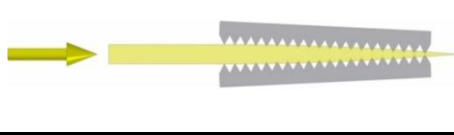
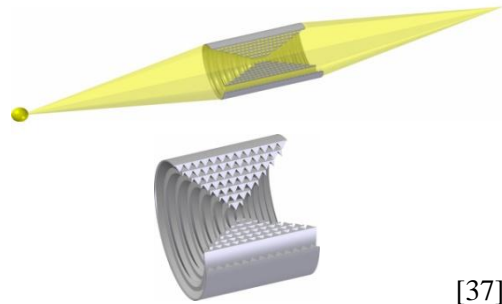
where d is the spacing of the periodic lattice, λ the wavelength of the photon, θ the incident angle and n the order of the diffraction [40]. The most common optics of this type is the Fresnel Zone Plate (FZP). A FZP consist of concentric rings of alternatively transparent and opaque material. If the switching between the different zones is at well-defined diameters, the rings build a diffraction grating so that the diffracted X-rays interfere constructively at the focal point.

Refractive optics work under the principle of refraction at the interface of two media described by the index:

$$n = 1 - \delta + i\beta \quad (3.3)$$

where δ characterizes the refraction and β the absorption. Since δ is small for X-rays n differs only by a factor of 10^{-5} to 10^{-7} from unity, which is why such a lens only provokes very little changes in the direction of the X-rays. Therefore and due to absorption Kirkpatrick and Baez [38] stated in 1948, that they consider focusing X-rays with refractive optics as "discouraging". Although δ is very small it is also positive, which leads according to equation (3.3) to a refractive index n which is less than unity. This means that one has to use a concave lens to focus X-rays. Due to this shape the central thickness of the lens can be made very small - limited by the stability of the lens material and the technological feasibility - to reduce the absorption losses within the lens material. The promising brilliance of the upcoming third generation synchrotron sources lead to reconsider the use of refractive lenses to focus X-rays. In 1991, Suehiro et.al. [41] suggested the use of single lenses made out of high-Z materials with a long focal distances. In 1996, Snigirev et.al. [42] proposed the use of a low-Z material to minimize the absorption, and align several lenses in a linear array to get a shorter focal distance. His group drilled 30 closely spaced holes with 0.3 mm diameter in an aluminum block of 19 mm length, fabricating the first Compound Refractive Lens (CRL) for high-energy X-rays. Tests showed that this CRL had a spot size of about 8 μm with a focal distance of 1.8 m for 14 keV X-rays. In table 3.1 an overview of the most common X-ray optical systems is given. As one can see a big variety of CRL designs was developed in the last years, starting with simple holes drilled in an Al-block manufactured by Snigirev et.al. in 1996 [42]. Shortly after parabolic refractive lenses [43, 44], bubble lenses [45] and alligator lenses [46], where basically just two pieces of an long-play vinyl record are putted together to form a lens, were designed. The most recent development are rolled X-ray prism lenses which were introduced by Nillius in 2011 [47].

Table 3.1 Focusing systems for X-rays (references to the sources are next to the pictures).

Reflecting Optics	Mirror optics	Kirkpatrick-Baez mirrors	
	Capillary optics	Polycapillary	
		Monocapillary	
Diffracting Optics	Fresnel Zone Plates		 <p style="text-align: right;">[48]</p>
Refracting Optics	Compound Refractive Lenses (CRL)	Hole array lenses	 <p style="text-align: right;">[37]</p>
		Parabolic (crossed planar)	 <p style="text-align: right;">[37]</p>
		Bubble lenses	 <p style="text-align: right;">[37]</p>
		Alligator lenses	 <p style="text-align: right;">[37]</p>
		Rolled X-ray prism lenses	 <p style="text-align: right;">[37]</p>

3.2 Refraction index

After W.C. Röntgen discovered the X-radiation in 1895, he could not distinguish that the beam was refracted and concluded that the index of refraction must be less than 1.05 [49]. In 1916 Barkla showed that there should be refraction with n in the order of 0.999995 to 1.000005 [50]. The refraction index for X-rays can be derived from the interaction between a photon and a bound electron using the forced oscillator model, where an elastically bound electron is forced to oscillate in the electric field of the impinging photon. The detailed derivation can be found for example, in the work of R.W. James from 1954 [51]. An important result of this theory is that it leads to a complex index of refraction for X-rays, given by:

$$n = 1 - \frac{\lambda^2}{2\pi} r_0 \frac{\rho N_A}{A} f(\vec{K}) \quad (3.4)$$

with the wavelength of the photon λ , the scattering length r_0 , the density of the matter ρ , the Avogadro constant N_A , the molar mass A and the atomic scattering factor

$$f(\vec{K}) = f_0(\vec{K}) + f'(\lambda) + i f''(\lambda) \quad (3.5)$$

where \vec{K} is the scattering vector between incident and scattered beam. Since for refractive optics only scattering in forward direction is beneficial, while the rest is attenuation, the atomic scattering factor, using the atomic number of the scattering element Z , can be rewritten as

$$f = Z + f'(\lambda) + i f''(\lambda) \quad (3.6)$$

This leads to equation (3.3) with δ characterizing the refraction and the imaginary part β characterizing the absorption as

$$\delta = \frac{\lambda^2}{2\pi} r_0 \frac{\rho N_A}{A} (Z + f'(\lambda)) \quad \text{and} \quad \beta = \frac{\lambda^2}{2\pi} r_0 \frac{\rho N_A}{A} f''(\lambda) \quad (3.7)$$

The value of the decrement δ is in the order of 10^{-5} to 10^{-7} and depends on two factors, the energy of the X-rays $\left(\frac{\lambda^2}{2\pi}\right)$ and the material of the lens via the scattering length, the number of relevant electrons per atom $(Z + f'(\lambda))$ and the density of atoms $\left(\frac{\rho N_A}{A}\right)$. Since δ is positive the real part of the refraction index is less than unity, which leads to the interesting effect that at the intersection from vacuum (air) to matter X-rays are refracted - on the contrary to what happens with visible light - towards the surface, which also leads for very small angles of incident to total external reflection which is e.g. used to build mirrors for X-rays.

The value of the imaginary part β depends also on the energy of the X-rays and the material of the lens and can be related to the attenuation coefficient μ by

$$\mu = 4\pi \frac{\beta}{\lambda} \quad (3.8)$$

In the energy range we are dealing with the attenuation coefficient consists of three parts, the photoabsorption coefficient τ , the elastic μ_R (Rayleigh) and the inelastic μ_C (Compton) scattering. When an X-ray beam with an intensity of I_0 passes through matter of a thickness d the attenuation coefficient can be used to calculate the intensity $I_{(d)}$ according to the Lambert-Beer law

$$I_{(d)} = I_0 e^{-\mu d} \quad (3.9)$$

3.3 Theory of a parabolic refractive lens for X-rays

A detailed theory for refractive lenses for X-rays can be found in the work of Snigirev et.al. [44], Protopopov et.al. [52], Elleaume [53] and others. In this chapter only a brief summary with some fundamental equations regarding this kind of lenses will be given, with emphasis on planar parabolic Compound Refractive Lenses (CRL's) since they were used in this work. Compared to lenses with cylindrical holes, parabolic shaped lenses are more difficult to fabricate, but since this lenses have among others the advantage that they are practically free of spherical aberration, great efforts were made in developing new manufacturing processes. A cross section of a parabolic lens with the main dimensions is shown in figure 3.1.

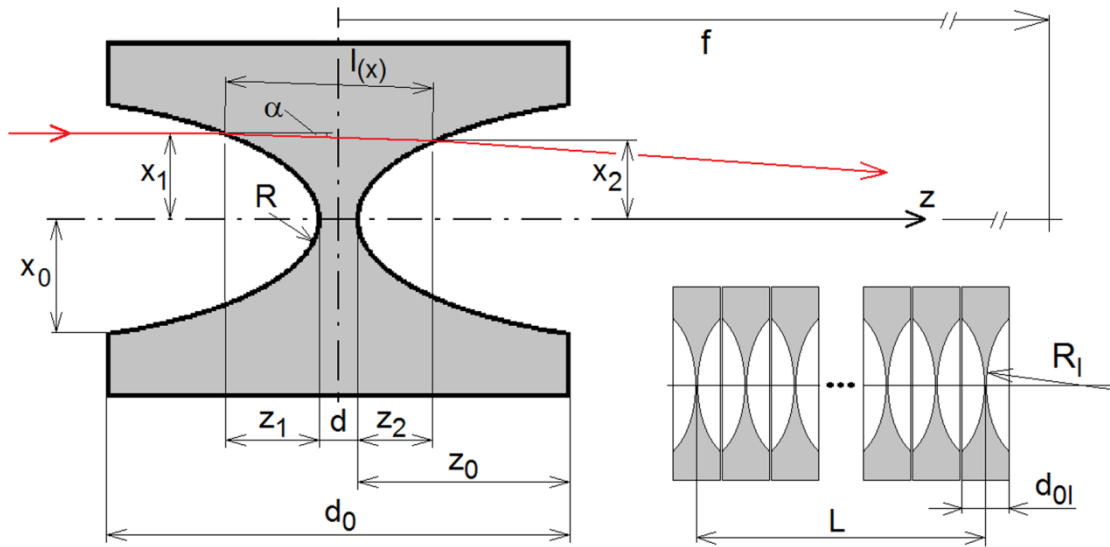


Figure 3.1 Schematics of a parabolic lens with encoded dimensions.

The surface for a parabolically shaped lens is given by

$$x = \pm\sqrt{2Rz} \quad (3.10)$$

with the curvature radius R and $z = 0$ at the apex, the focal length for the lens can be calculated with

$$f = \frac{R}{2\delta} \quad (3.11)$$

The aperture of such a lens is limited only by the absorption of the beam and can be written with the attenuation coefficient μ as

$$A = 2x_0 = 2\sqrt{\frac{2R}{\mu}} \quad (3.12)$$

and the thickness of the lens is given by

$$d_0 = \frac{x_0^2}{R} + d \quad (3.13)$$

Snigirev et.al. [44] give an example for a lens made of boron for 30 keV photons with an requested aperture of 1 mm and focal length of 1 m. Such a lens would have a curvature radius R of about 1 μm and a thickness d_0 of 25 cm which is very difficult to fabricate. The idea to overcome this problem was to use N lenses in a row which allows increasing the curvature radius while simultaneously the lens thickness decreases. For a lens with the same characteristics as above the radius R_l of a single lens is

$$R_l = \frac{R}{N} = \frac{2\delta f}{N} \quad (3.14)$$

The thickness d_{0l} of a lens thereby becomes N times smaller leaving the total length of the compound lens approximately the same as for the single lens (d_0).

3.3.1 Focal length of a parabolic refractive lens

As illustrated in figure 3.1 when a parallel incoming beam hits the lens, it gets refracted at the interface between air and lens material (z_1), passes the lens and refracts again when it passes from the lens to the air (z_2).

For the calculation of the focal distance, the minimal thickness of the lens d can be set to zero without effect on the result.

$$d = 0 \quad (3.15)$$

To calculate the focal length, the optical length of two different paths reaching the focal spot, have to be equal. Choosing one path along the optical axis and another like indicated red in figure 3.1, with the refractive indices $n' = 1$ for air and $n = 1 - \delta$ for the lens. Since the refraction is low and the thickness of the lens is small ($l_{(x)} < 1 \text{ mm}$), assumptions like $\cos \alpha \approx 1$, $\sin \alpha \approx 0$, $z_1 \approx z_2$ and therefore $x_1 \approx x_2$ can be made to simplify the calculation.

The optical length of two possible paths has to be equal for constructive interference at the focal point and a comparison gives

$$2z_1 - 2z_1\delta + f\sqrt{1 + \frac{x_2^2}{f^2}} - z_1 = z_1 + f \quad (3.16)$$

The square root term can be expanded in a series

$$\sqrt{1+x} = \sum_{n=0}^{\infty} \binom{1/2}{n} x^n = \sum_{n=0}^{\infty} \binom{2n}{n} \frac{(-1)^n}{(1-2n)4^n} x^n \quad (3.17)$$

and since $f \gg x_2$ the series can be truncated after the second term giving

$$\begin{aligned} 2z_1 - 2z_1\delta + f \left(1 + \frac{x_2^2}{2f^2}\right) - z_1 &= z_1 + f \\ \rightarrow \frac{x_2^2}{2f} &= 2z_1\delta \end{aligned} \quad (3.18)$$

and with the formula for a parabolically surface (3.10) this leads to equation (3.11).

3.3.2 Derivation of the main parameters of a parabolic CRL

Due to the weak refraction the focal length can, depending on material and photon energy, reach hundreds of meters. Building a Compound Refractive Lens (CRL) by placing N of those single lenses together in a properly aligned stack, the focal length can be reduced to

$$f_0 = \frac{f}{N} = \frac{R}{2N\delta} \quad (3.19)$$

This equation is valid as long as the thin lens limit $f_0 \gg L$ is fulfilled, where L is the total length of the lens stack (see figure 3.1). The basis of this approximation is that the ray, by passing through the lens, changes his direction but not his position in the x -direction. With lenses used for energies higher than about 20 keV, or a short focal length is required, the total length L of the CRL has a comparable size to the focal length f_0 and the thin lens approximation is not longer valid. Due to the curved X-ray path caused by the continuous focusing of the lenses the x -position cannot be seen as constant (cf. $x_0 \leftrightarrow x_N$ in figure 3.2) and corrections to the equations above have to be made.

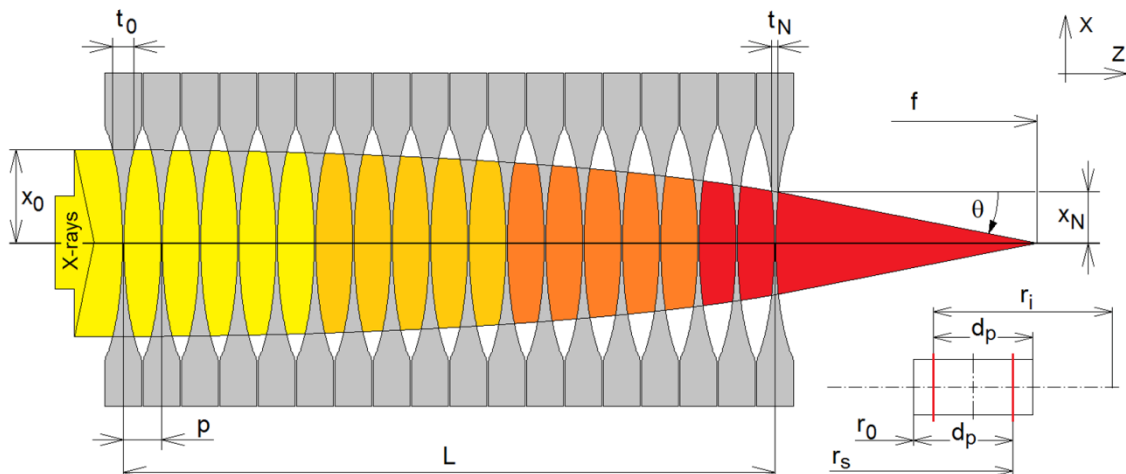


Figure 3.2 Geometry of the beam in a thick parabolic compound refractive lens

To achieve this either ray-tracing methods as the ones used by Protopopov et al. [52] and Pantell et al. [54], for example, or analytical methods using a propagator similar to the free space Kirchhoff propagator - as done e.g. by Kohn [55] - can be used to derive the main lens parameters for a thick parabolic CRL.

3.3.2.1 Ray-tracing method

The relevant parameters are indicated in figure 3.2 being x the distance and θ the angle of the ray in relation to the optical axis of the lens. With the assumption that the lens elements are sufficiently close to each other so that the focusing can be seen as continuous the change in angle and x-position can be written as

$$d\theta = \frac{x}{f_0 L} dz \quad \text{and} \quad dx = -\theta dz \quad (3.20)$$

The matrix formulation for the values of x and θ from the front surface ($z = 0$) to the back surface ($z = L$) is given by

$$\begin{bmatrix} x_N \\ \theta_N \end{bmatrix} = M \begin{bmatrix} x_0 \\ \theta_0 \end{bmatrix} \quad (3.21)$$

$$\text{with } M = \begin{bmatrix} \cos L_f & -f_0 L_f \sin L_f \\ \frac{1}{f_0 L_f} \sin L_f & \cos L_f \end{bmatrix} \quad (3.22)$$

$$\text{and } L_f = \sqrt{\frac{L}{f_0}} = \sqrt{\frac{Rp}{2\delta f_0^2}} \quad (3.23)$$

For a thick lens principal planes can be defined (see Born et al. [56]), in a way that when the distance to the source r_s is measured from one and the distance to the image r_i from the other (see figure 3.2) the thin lens relation

$$\frac{1}{f} = \frac{1}{r_s} + \frac{1}{r_i} \quad (3.24)$$

is fulfilled with the according matrix

$$\begin{bmatrix} 1 & 0 \\ 1/f & 1 \end{bmatrix} \quad (3.25)$$

The principle plane can be found as the intersection point of the linear extensions from the incoming and outgoing rays, where d_p is the distance between this plane and the end of the lens. For a linear ray it becomes

$$\begin{bmatrix} 1 & d_p \\ 0 & 1 \end{bmatrix} \quad (3.26)$$

and therefore in matrix formulation

$$\begin{bmatrix} 1 & d_p \\ 0 & 1 \end{bmatrix} M \begin{bmatrix} 1 & d_p \\ 0 & 1 \end{bmatrix} = \begin{bmatrix} 1 & 0 \\ 1/f & 1 \end{bmatrix} \quad (3.27)$$

with the solution

$$\frac{f}{f_0} = \frac{L_f}{\sin L_f} \quad (3.28)$$

$$d_p = f (1 - \cos L_f) \quad (3.29)$$

For a thick lens f can get smaller than d_p , which means that the focal point is within the lens. From equation (3.29) the ratio $\frac{f}{d_p}$ can be calculated leading for $f < d_p$ to limits for L_f from

$$\frac{3\pi}{2} > L_f - 2\pi m > \frac{\pi}{2} \quad (3.30)$$

with m being a positive integer. Provided that the image plane has to be outside the lens ($r_i \geq d_p$) the maximum value for the distance source to lens is given by

$$\left. \frac{r_s}{f} \right|_{max} = 1 - \frac{1}{\cos L_f} \quad (3.31)$$

The fact that r_s might have a maximum has also consequences on the achievable gain of the CRL since the one-dimensional gain G for $r_s < \frac{A_0^2}{\lambda}$ (for cylindrical holes) is given by

$$G = \frac{TA_0 r_s}{\sigma f} \quad (3.32)$$

where T represents the transmission, A_0 the aperture and σ the size of the source [42].

For a lens where the thickness is assumed negligible, the aperture A_0 is given by

$$A_0 = 4 \sqrt{\frac{\delta f_0}{\mu}} \quad (3.33)$$

where δ is the decrement of the refraction index and μ the absorption coefficient of the according lens material. For a thick CRL, where the x-position of the ray through the lens is no longer constant, the aperture becomes

$$\frac{A}{A_0} = \frac{x_0}{\sqrt{\int_0^L dz \frac{x(z)^2}{L}}} \quad (3.34)$$

with the radius at the beginning of the lens x_0 and also as a function of the distance z within

the lens being

$$x_{(z)} = x_0 \left(\cos \frac{z}{f_0 L_f} + \frac{f_0 L_f}{r_0} \sin \frac{z}{f_0 L_f} \right) - s \left(\frac{f_0 L_f}{r_0} \sin \frac{z}{f_0 L_f} \right) \quad (3.35)$$

with the distance between source and beginning of the lens r_0 and the x-position of the ray at the source s and in case the lens is far from the source, so that $\frac{f_0 L_f}{r_0} \ll 1$, the aperture becomes only a function of L_f .

With increasing thickness of the CRL the maximal aperture increases as well since the rays are on a curved trajectory towards the optical axis where the lenses get thinner and the losses diminish. Due to the restriction that the image plane has to be outside the lens the maximum of the ratio $\frac{A}{A_0}$ and also the increase in the gain is 1.4 for $(L_f = \frac{\pi}{2})$.

3.3.2.2 Analytical method

The general solution of the Maxwell equation is given by

$$E_{(x,y,z)} = e^{ikz} A_{t(x,y,z)} \quad (3.36)$$

where $k = \frac{\omega}{c}$ is the wave number in vacuum and the function $A_{t(x,y,z)}$ describing the radial dependence of the wave field from the z -axis. A paraxial approximation, neglecting the second derivative of $A_{t(x,y,z)}$ with respect to z , still gives good results since the radiation interacts very weakly with the lens material leading to a parabolic equation for the function $A_{t(x,y,z)}$

$$\frac{dA_{t(x,y,z)}}{dz} = -ik\eta s_{(x,y,z)} A_{t(x,y,z)} + \frac{i}{2k} \left(\frac{d^2 A_{t(x,y,z)}}{dx^2} + \frac{d^2 A_{t(x,y,z)}}{dy^2} \right) \quad (3.37)$$

where $\eta = 1 - n = \delta - i\beta$ and $s_{(x,y,z)}$ is unity within the material and zero outside.

For a compound lens with many elements the thin lens approximation can be assumed as fulfilled for a single lens element and therefore the function $s_{(x,y,z)}$ can be averaged over the period p and replaced by the function

$$\bar{s}_{(x,y)} = \frac{d}{p} + \frac{x^2}{pR_l} + \frac{y^2}{pR_l} \quad (3.38)$$

With the initial wave field at the entrance of the lens as Fourier integral

$$A_{t(x,y,0)} = A_0(x,y) = \int \frac{dq_x dq_y}{(2\pi)^2} \tilde{A}_0(q_x, q_y) e^{i(q_x x + q_y y)} \quad (3.39)$$

and its solution in form of a plane wave

$$\tilde{P}_t(x, q_x, y, q_y, z) = e^{-ik\eta \frac{d}{p} z} \tilde{P}_{(x, q_x, z)} \tilde{P}_{(y, q_y, z)} \quad (3.40)$$

The partial function $\tilde{P}_{(x, q, z)}$ has to satisfy the equation

$$\frac{d\tilde{P}}{dz} = -i \frac{k\eta}{pR_l} x^2 \tilde{P} + i \frac{1}{2k} \frac{d^2\tilde{P}}{dx^2} \quad \text{with} \quad \tilde{P}_{(x, q, 0)} = e^{iqx} \quad (3.41)$$

and with an approach in form of a Gaussian function (reasonable because of the initial function)

$$\tilde{P}_t(x, q_x, y, q_y, z) = e^{i(a_0(z) + a_1(z)x + a_2(z)x^2)} \quad (3.42)$$

where the complex coefficients for $z = 0$ have the values $a_{0(0)} = a_{2(0)} = 0$ and $a_{1(0)} = q$.

Equation (3.41) can be rewritten as a system of ordinary differential equations

$$\frac{da_0}{dz} = i \frac{a_2}{k} - \frac{a_1^2}{2k}, \quad \frac{da_1}{dz} = -\frac{2a_1 a_2}{k} \quad \text{and} \quad \frac{da_2}{dz} = -\frac{k\eta}{pR_l} - \frac{2a_2^2}{k} \quad (3.43)$$

which for any initial conditions have an analytical solution in the form of

$$a_0(z) = a_{0(0)} - \frac{i}{2} \ln \left(\frac{\cos \alpha}{\cos(\alpha - z/z_c)} \right) - \frac{a_{1(0)}^2 z_c \tan(z/z_c)}{2k[1 + \tan \alpha \tan(z/z_c)]}$$

$$a_1(z) = a_{1(0)} \frac{\cos \alpha}{\cos(\alpha - z/z_c)} \quad \text{and} \quad a_2(z) = a_{2(0)} \frac{\tan(\alpha - z/z_c)}{\tan \alpha} \quad (3.44)$$

$$\text{with} \quad \tan \alpha = \frac{z}{z_c}, \quad z_0 = \frac{k}{2a_{2(0)}} \quad \text{and} \quad z_c = \sqrt{\frac{pR_l}{2\eta}}$$

Using these relations and the initial conditions, the partial function can be written as

$$\tilde{P}_{(x, q, z)} = e^{-i \frac{k \tan(z/z_c)}{2z_c} x^2} \sqrt{\frac{1}{\cos(z/z_c)}} e^{i \left(\frac{x}{\cos(z/z_c)} - \frac{z_c \tan(z/z_c)}{2k} q^2 \right)} \quad (3.45)$$

From the general solution in integral form (see eqn. (3.39)) the integral transformation for a parabolic compound X-ray lens can be obtained

$$A_t(x, y, z) = \int dx' dy' P_t(x, x', y, y', z) A_t(x', y', 0) \quad (3.46)$$

where the propagator is $P_t(x, x', y, y', z) = e^{-ik\eta \frac{d}{p} z} P_{(x, x', z)} P_{(y, y', z)}$ and the partial propagator is

$$P_{(x, x', z)} = e^{-i \frac{\pi \tan(z/z_c)}{\lambda z_c} x^2} \sqrt{\frac{1}{i\lambda z_c \sin(z/z_c)}} e^{i\pi \frac{(x-x' \cos(z/z_c))^2}{\lambda z_c \cos(z/z_c) \sin(z/z_c)}} \quad (3.47)$$

with the X-ray wavelength $\lambda = \frac{2\pi}{k}$.

For the propagation in air where $\eta = 0$ the limit $|z_c| \rightarrow \infty$ in equation (3.47) leads to

$$P_{(x,x',z)} \xrightarrow{|z_c| \rightarrow \infty} P_K(x-x',z) = \sqrt{\frac{1}{i\lambda z}} e^{i\pi \frac{(x-x')^2}{\lambda z}} \quad (3.48)$$

Considering the radiation transfer in air from the source to the lens over a distance of r_0 the passing through the lens with a length of L and to a point after lens in a distance of r_i , the propagator can be written as

$$G_{(x,x',r_0,L,r_i)} = \int dx_2 dx_1 P_K(x-x_2,r_i) P_{(x_2,x_1,L)} P_K(x_1-x',r_0) \quad (3.49)$$

Since $\gamma = \frac{\beta}{\delta} \ll 1$ the parameter z_c can be written as $z_c = \sqrt{pf} \left(1 + i\frac{\gamma}{2}\right)$ and the propagator in the thin lens limit ($L \ll \sqrt{pf}$) is

$$P_0(x,x',L) = e^{-i\pi \frac{x^2}{\lambda f_0} (1-i\gamma)} P_K(x-x',L) \quad (3.50)$$

leading for the focal length f_0 to the already known equation (3.19).

Due to absorption within the lens the plane wave obtains a Gaussian shape intensity distribution considered to be the effective aperture of the lens with a half-width of

$$\alpha_\gamma = 0.664 \sqrt{\frac{\lambda F}{\gamma}} \quad (3.51)$$

For $L_0 = \sqrt{pf} \frac{\pi}{2}$, $\sin \frac{z}{z_c} = 1$ and $\cos \frac{z}{z_c} = i\gamma \frac{\pi}{4}$ in the linear approximation in γ the propagator can be written as

$$P_{(x,x')} = \sqrt{\frac{1}{i\lambda z_c}} e^{-\left(i\frac{2\pi}{\lambda z_c} xx' + \gamma \frac{\pi^2}{4\lambda z_c} (x^2 + x'^2)\right)} \quad (3.52)$$

From this expression it follows that the plane wave after the lens has a Gaussian intensity distribution leading to a focal spot diameter with a half-width of

$$s_\gamma = 0.47 \sqrt{\lambda L_0 \gamma} \quad (3.53)$$

and an effective aperture of

$$\alpha_\gamma = 0.846 \sqrt{\frac{\lambda L_0}{\gamma}} \quad (3.54)$$

3.4 Properties of a parabolic compound refractive lens

3.4.1 Aberrations

For an ideal parabolic refractive lens the spherical aberration, astigmatism and coma can be neglected since the paraxial approximation is fulfilled, meaning that the geometry is very narrow due to the straight optical path and the small field of view. The chromatic aberration is the only one remaining for parabolic refractive lenses due to the fact that the focal length f depends on decrement δ (see eqn. (3.11)) and δ depends on the photon wavelength λ (see eqn. (3.7)). Due to this effect a parabolic refractive lens cannot focus a polychromatic X-ray beam in a point and the difference in the focal length depending on the energy bandwidth can be written

$$\frac{\Delta f}{f} = 2 \frac{\Delta E}{E} \quad (3.55)$$

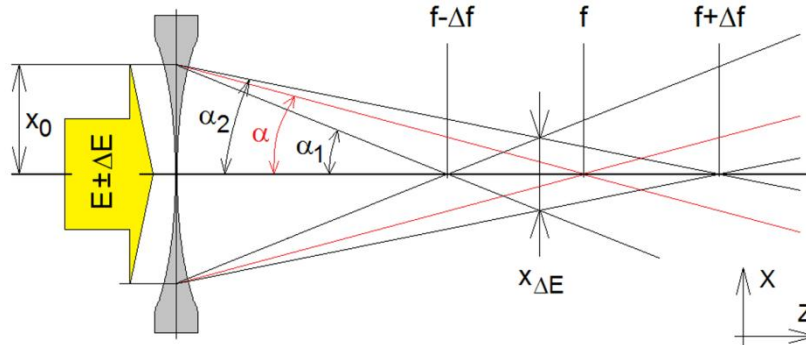


Figure 3.3 Chromatic aberration of a parabolic compound refractive lens

Figure 3.3 shows the geometrical situation when a polychromatic beam hits a parabolic refractive lens, creating a blur of width $x_{\Delta E}$ which can be derived by trigonometry

$$\begin{aligned} \tan \alpha_1 &= x_0 \frac{1}{f - \Delta f}, \quad \tan \alpha_2 = x_0 \frac{1}{f + \Delta f} \quad \text{and} \\ 2\Delta f &= \frac{x_{\Delta E}}{2} \frac{1}{\tan \alpha_1} + \frac{x_{\Delta E}}{2} \frac{1}{\tan \alpha_2} \end{aligned} \quad (3.56)$$

giving

$$x_{\Delta E} = 2x_0 \frac{\Delta f}{f} = 4x_0 \frac{\Delta E}{E} \quad (3.57)$$

3.4.2 Transmission and gain

The transmission of a CRL with N lenses and a thickness of d between the apices can be calculated (see e.g. Lengeler et al. [57]) according the Lambert-Beer law (see equation (3.9)). For lenses where the surface roughness can be neglected the transmission parameter a_p can be written as

$$2a_p = \mu N 2z_0 = \frac{\mu}{\rho} \frac{x_0^2}{2f_0} \frac{\rho}{\delta} \quad (3.58)$$

and this leads to the expression for the transmission

$$T = e^{-\mu N d} \frac{1 - e^{-2a_p}}{2a_p} \quad (3.59)$$

with the first term representing the absorption within the material and the second term considers the varying thickness of the parabolas. It is evident that the transmission increases with decreasing mass absorption coefficient and x_0 .

The gain of a CRL is defined as the ratio of the intensity in the focal spot and the intensity behind a pinhole of the same size as the spot of the lens. With s_v as the full width half maximum (FWHM) size of the beam in vertical and s_h in horizontal direction the gain of a CRL can be written as

$$G = T \frac{4x_0^2}{s_v s_h} \quad (3.60)$$

3.4.3 Lateral resolution and depth of focus

The lateral resolution of an X-ray lens is given as (see Lipson et al. [58])

$$d_l = \text{const} \frac{\lambda}{2A_N} \quad (3.61)$$

with the numerical aperture A_N and the constant of order 1 varying slightly depending on the geometry of the setup. Since α is small for refractive lenses we can write

$$A_N = \sin \alpha \approx \tan \alpha \approx \frac{d_{eff}}{2f} \quad (3.62)$$

and with the effective aperture d_{eff} for a parabolic refractive lens in the form

$$d_{eff} = 2x_0 \sqrt{\frac{1 - e^{-a_p}}{a_p}} \quad (3.63)$$

the lateral resolution is

$$d_l \approx \text{const} \frac{\lambda f}{d_{eff}} \quad (3.64)$$

with $\text{const} \approx 1$.

In beam direction a length called depth of focus d_{focus} , where the lateral beam size does not significantly exceed the spot size given by s_v and s_h , can be defined as

$$d_{focus} = \frac{4}{2\sqrt{2}\ln 2} \frac{s_{v,h} f}{d_{eff}} \quad (3.65)$$

Since for compound refractive lenses the effective aperture is much smaller than the focal distance the depth of focus is in the range of millimeters up to some centimeters.

3.4.4 Surface roughness

The surface roughness of the lens causes a blur of the spot and therefore influences the lateral resolution. Other than for high quality X-ray mirrors, where the roughness has to be kept in the Ångström range, the performance of lenses is only affected when the roughness reaches the 10^3 Ångström range.

3.4.5 Lens material

The material used for a refractive lens has to fulfill various requirements which are briefly discussed here. As already seen above one of the most vital parameters is the

mass absorption coefficient of the lens material due to the fact that the transmission increases with decreasing $\frac{\mu}{\rho}$. Therefore low-Z elements like Li, Be, B, C and so on or materials composed from low-Z elements like polymers should be used as lens materials. Another important feature is the

homogeneity of the lens material since every variation in density or composition leads to small angle X-ray scattering (SAXS) and the scattered photons do not contribute to the focused beam but to the background. Since inhomogeneity is a consequence of the bulk material fabrication process and not a characteristic of an element, the amount of inhomogeneities in the bulk material has to be evaluated for every new batch of bulk material. Especially for the use at synchrotron beamlines with their high photon flux the

durability of the lens material in the beam is an important feature. There are two factors to consider, the first is that the radiation is ionizing the matter so that to replace the knocked-

out electrons the material should not be an insulator. The second factor is that the absorbed radiation creates a heat load in the material of the lenses. The lenses have to withstand this heat without becoming deformed. Furthermore a very important factor for the production of the lenses, is the

machinability of the lens material. Depending on the manufacturing technique the material has to have certain qualities like ductility for stamping techniques or grindability for drilling holes.

In the following a short list of suitable materials for refractive X-ray optics is presented.

Lithium (Li):	+ transmission – very corrosive (only in oxygen free environments)
Beryllium (Be):	+ transmission, durable – no ductility at room temperature, toxic
Boron (B):	+ weak scattering, durable – extremely hard, not easily machinable
Boron carbide (B₄C):	+ as hard as B but due to spark erosion it is better machinable – scattering is far too strong
Carbon (C):	+ durable ± scattering and machinability dependent on the structure: Diamond: weak scattering but hard to machine Glassy carbon: easier to machine but strong scattering
Aluminum (Al):	+ ductile, machinability, weak scattering, durable – low transmission for photons with $E < 20$ keV
Polymers:	+ transmission, machinability, homogeneity, costs – durability in the beam

4 Analytical techniques

4.1 X-ray fluorescence analysis

X-ray Fluorescence Analysis (XRF) is a well known spectroscopic technique suitable for qualitative and quantitative elemental analysis of unknown samples. The big advantages of XRF, compared with many other methods, are its non-destructiveness and capability of detecting all elements from Boron ($Z=5$) upwards. Furthermore, samples can be analyzed at any aggregate state and a sample preparation is in many cases not necessary at all. Disadvantages are the poorer limits of detection (LOD) compared with e.g. mass spectrometry methods and a small information depth which is depending on the analyzed element and the matrix.

XRF is based on two basic principles, the photoelectric effect and the emission of fluorescence radiation with an energy characteristic for the emitting element. The energy of this characteristic radiation can be measured with a wavelength or energy dispersive spectrometer.

The wavelength dispersive detector is based on Bragg's law,

$$n\lambda = 2d \sin \theta \quad (4.1)$$

where n is the order of the reflex, d the spacing between the planes in the atomic lattice, λ the wavelength of the radiation and θ the angle between the lattice plane and the impinging radiation. Using a crystal with well known d the wavelength of the emitted radiation can be determined by scanning the angle θ . Depending on the crystal and the wavelength, the energy resolution of this method is about 10 times better than the one of an energy dispersive detector. The big advantage of an energy dispersive detector is that an energy range from less than one up to tens of keV can be measured simultaneously.

4.1.1 Qualitative and quantitative X-ray fluorescence analysis

The foundation for the qualitative analysis of an unknown sample was laid in 1913 and 1914, when Moseley [1, 2] discovered the correlation between the energy of the fluorescence radiation E and the atomic number of the emitting element Z given by

$$E = K(Z - \sigma)^2 \quad (4.2)$$

with K and σ being constants depending on the observed fluorescence line

Figure 4.1 shows a sketch of the geometrical conditions of a standard XRF setup.

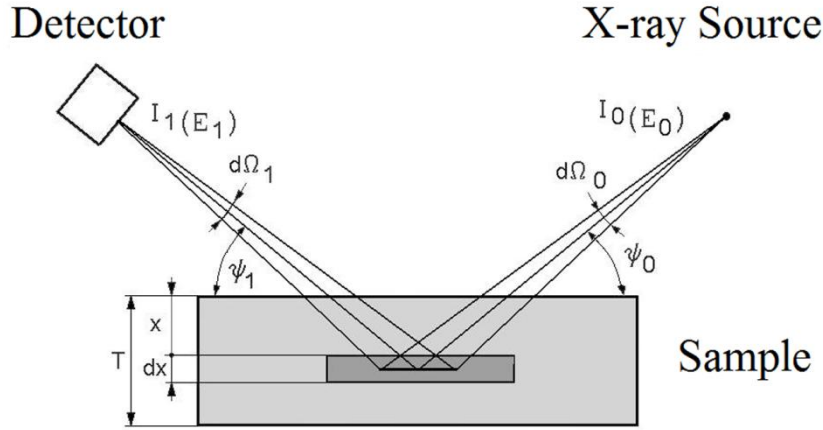


Figure 4.1 Sketch of a standard XRF setup.

Besides of a qualitative analysis of the elements composing the sample, XRF is also a quantitative method, since there is a correlation between the intensity of the fluorescence signal I and the concentration of the emitting element within the sample c_i . But the intensity of the fluorescence signal is not only depending on the concentration but also on several other factors. Taking all relevant factors into account the equation for the fluorescence intensity of an element i is

$$I_{E_{i,j,k}} = \frac{d\Omega_0 d\Omega_1}{4\pi} \int_{E_{abs}}^{E_{max}} dE \int_0^T dx I_0(E) \frac{\rho}{\sin \psi_0} \left(1 - \frac{1}{S_{i,j}}\right) \left(\frac{\tau}{\rho}\right)_i \cdot c_i p_{i,j,k} \omega_{i,j} \varepsilon_{E_{i,j,k}} f_{E_{i,j,k}} V \exp\left[-\left(\frac{\mu_{E_{i,j,k}}}{\rho \sin \psi_1} + \frac{\mu_E}{\rho \sin \psi_0}\right) \rho x\right]. \quad (4.3)$$

with: $I_0(E)$...photon intensity emitted from the source in a solid angle of $d\Omega_0$

$d\Omega_1$...solid angle of the detector

E_{abs} ...absorption edge energy of the element

$\left(1 - \frac{1}{S_{i,j}}\right) \left(\frac{\tau}{\rho}\right)_i$...probability for excitation of element i in shell j

$p_{i,j,k}$...probability for transition from shell k to j

$\omega_{i,j}$...fluorescence yield

$\varepsilon_{E_{i,j,k}}$...detector efficiency

$f_{E_{i,j,k}}$...absorption between sample surface and detector

V ...factor for secondary excitation by elements with high fluorescence energy

$\exp[...]$...attenuation of the fluorescence and primary beam in the sample

where τ_i is the photo absorption coefficient from shell j of element i and $S_{i,j}$ the absorption edge step.

Under the presumption that the sample is homogeneous the integral over dx can be calculated and when the primary radiation is monochromatic with an energy E_0 equation (4.3) can be written as

$$I_{E_{i,j,k}} = \frac{d\Omega_0 d\Omega_1}{4\pi} I_{0(E_0)} \frac{\rho}{\sin \psi_0} \left(1 - \frac{1}{S_{i,j}}\right) c_i \sigma_{i,j,k(E_0)} \varepsilon_{E_{i,j,k}} f_{E_{i,j,k}} V T A_{(E_0)} \quad (4.4)$$

with $A_{(E_0)}$ including all absorption factors and $\sigma_{i,j,k(E_0)}$ including the parameters for the fluorescence cross section.

In case of a infinitely thin sample, where the sample thickness is less than $T_{99\%}$ with

$$T_{99\%} = \frac{-\ln 0.99}{\left(\frac{\mu_{E_{i,j,k}}}{\rho \sin \psi_1} + \frac{\mu_E}{\rho \sin \psi_0}\right)\rho} \quad (4.5)$$

the absorption and the secondary excitation effects can be neglected. The intensity of the fluorescence radiation depends in this case on the fundamental parameters and the measurement conditions. Therefore the intensity measured on a on a thin sample is directly proportional to the concentration of the element in the sample and given by

$$I_{E_{i,j,k}} = c_i S_i m \quad (4.6)$$

where S_i is the sensitivity of the spectrometer for the element i , c_i the concentration and m the mass of the sample.

4.2 X-ray beam induced current

X-ray beam induced current (XBIC) is a method developed for the analysis of solar cells [59]. The principle of XBIC is similar to the earlier developed methods EBIC (Electron beam induced current) or LBIC (Laser beam induced current). The only difference between these methods is that instead of an electron or laser beam a focused X-ray beam generates the minority charge carriers within the Si-wafer. The efficiency of the solar cell is characterized by the minority carrier diffusion length, which is determined by measuring the current induced by the beam. Having a beam scanning across the solar cell, an image of the minority carrier diffusion length can be made showing the electrically active defects within the solar cell. The big advantage of XBIC is that, in comparison to the other methods, a μ -XRF mapping of a solar cell is made simultaneously, allowing a direct correlation between the recombination activity and the distribution of metal impurities within the solar cell.

4.3 X-ray absorption spectroscopy (XAS)

4.3.1 X-ray absorption

This chapter only gives a brief overview of the theory of X-ray absorption spectroscopy, based on the more detailed work of Lengeler [60] or Baumgartel [61], the review of Rehr and Albers [62] or the paper of Yano and Yachandra [63].

The first recorded observation of absorption effects by P. Bouguer date back to the year 1729 [64]. Lambert in 1760 [65] and Beer in 1852 [66] published their work where they formulated the law for the absorption of light, nowadays named after them Lambert-Beer-law

$$I(E) = I_0(E)e^{-\mu(E)x} \quad (4.7)$$

where $I(E)$ is the intensity of the beam after passing the absorber, when $I_0(E)$ is the incoming intensity, x the thickness of the absorber (see figure 4.2) and $\mu(E)$ the absorption coefficient of the material at the according energy. The absorption coefficient of a material consisting of a single element as function of the energy looks typically like drawn in figure 4.2 (right), showing that the general decrease of $\mu(E)$ is interrupted by step-function like increases at certain energies.

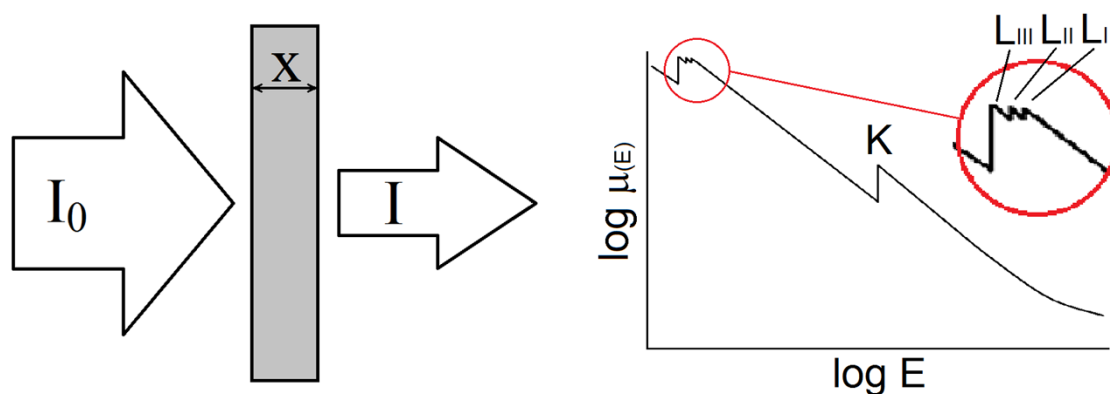


Figure 4.2 Schematic view of the Lambert-Beer law (left) and the absorption coefficient as function of the photon energy (right).

These phenomena are well understood, so is the decrease due to the absorption of X-rays by atoms well described in standard texts of quantum mechanics (e.g. Messiah, 1996) by Fermi's "golden rule". The sharp raises at certain energies, the so-called absorption edges, arise from the ejection of core electrons into the lowest unoccupied molecular orbit (LUMO) or to the continuum producing a photoelectron. These edges are labeled according to the core level the electron was ejected from, as e.g. when the photoelectron originates from the $1s$ orbit the edge is called K-edge and L-edge when from ($2s$) or ($2p$). The L-edge splits in three

parts, according to the different orbital-quantum numbers ($l = 0$ or 1) and total angular momentum quantum numbers ($j = \frac{1}{2}$ or $\frac{3}{2}$) of the involved electron;

$$L_I : (l = 0, j = \frac{1}{2}), L_{II} : (l = 1, j = \frac{1}{2}) \text{ and } L_{III} : (l = 1, j = \frac{3}{2}).$$

A model of the core electron energy levels is shown in figure 4.3.

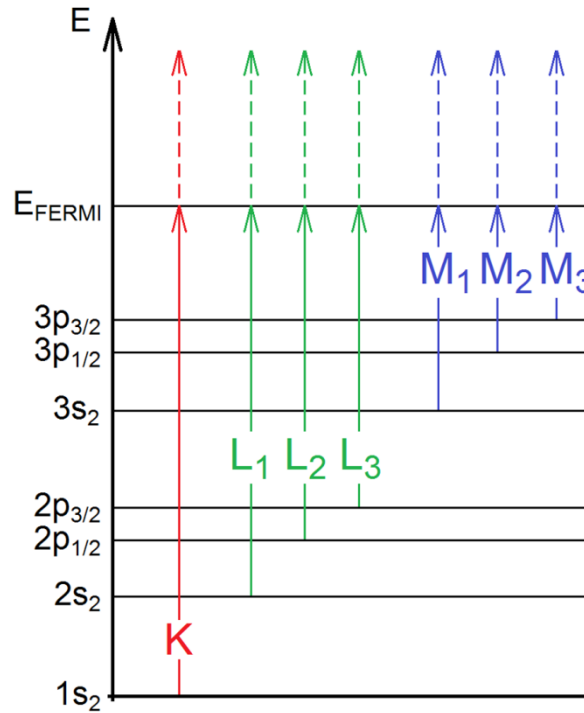


Figure 4.3 Model of the core electron energy levels and the excitations corresponding to K-, L- and M-edge. (energy levels are not drawn to scale)

The arrows indicate the energy difference for the excitations corresponding to the K-, L- and M-absorption edges. The energies of these edges are as unique for each element as the energy of the fluorescence radiation since each absorption edge is related to a transition of a specific core electron from a particular element. The energy of the impinging photons at the absorption edge thereby corresponds exactly to the energy difference between the according core level and the Fermi energy (E_{FERMI}) which is called binding energy of the core electron (E_0). Figure 4.4 shows, schematically, the absorption of an X-ray through the photoelectric effect on an isolated atom. When the X-ray has energy equal to the binding energy of the core electron (E_0) the absorption probability shows a sharp rise (figure 4.4 on the right) and a photoelectron is created. If the impinging photon energy is higher than this, the emitted photoelectron has a kinetic energy E_{kin} or when seen as a wave a wave number λ of

$$E_{kin} = E - E_0 = h\nu - E_0 \quad \text{or} \quad \lambda \propto \sqrt{E - E_0} \quad (4.8)$$

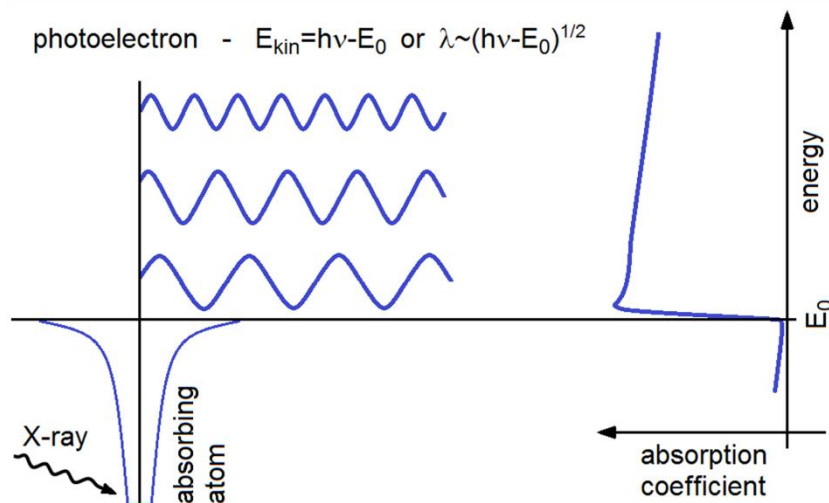


Figure 4.4 X-ray absorption by a core electron from an isolated atom

For energies below this threshold the absorption is defined by excitation of higher levels and other processes like Compton- or Rayleigh-scattering.

The relaxation of the excited atoms happens by refilling the core hole with an electron of an outer shell. The difference in the binding energies between the two involved core levels has to be emitted and this can occur in three ways, as characteristic fluorescence radiation, in form of Auger-electrons or via secondary-electrons. The intensity of the emitted fluorescence radiation (I_F) or Auger-electrons (I_A) is directly proportional to the absorption probability of the impinging photons and can be used to determine the absorption coefficient.

A useful empirical formula to calculate the absorption coefficient was given by J. A. Victoreen in 1949 [67]

$$\frac{\mu(\lambda)}{\rho} = C\lambda^3 - D\lambda^4 + \sigma_{KN} \frac{N_A Z}{A} \quad (4.9)$$

with the element specific constants C and D , the density ρ , the Klein-Nishina coefficient σ_{KN} the Avogadro constant N_A , the atomic weight A and the atomic number Z . The constants C and D , which are changing abruptly at the absorption edges, and σ_{KN} are tabulated in the "International tables for crystallography, Volume C (2006)".

4.3.2 X-ray absorption fine structure (XAFS)

For non isolated atoms the absorption coefficient shows (beside this "rough" structure) oscillations at energies near and above the edge, which is called X-ray absorption fine structure (XAFS). This structure occurs because the photo-electron when scattered from a neighboring atom can return to the absorbing atom and modulate the amplitude of the photo-electron

wave-function at the absorbing atom. This in turn modulates the absorption coefficient $\mu(E)$ as shown schematically in figure 4.5. These oscillations depend on the local atomic coordination and oxidation state of the atom providing a unique signature for a given material.

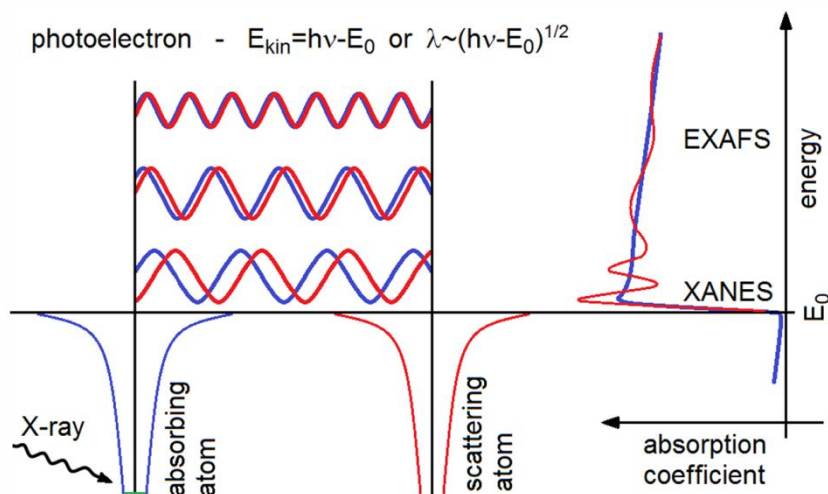


Figure 4.5 X-ray absorption fine structure caused by scattering from neighboring atoms

The X-ray absorption spectra can be divided into two parts as shown in figure 4.5 on the right side, the first covering an energy range from ~ 100 eV below to some tens of eV above the edge is called XANES (X-ray absorption near edge structure) and the second called EXAFS (extended X-ray absorption fine structure) ranges from some tens to several 100 eV above the edge. The borders of these regions are not fixed but depending on the dominant scattering process of the photoelectron. For low kinetic energies the so called X-ray absorption near edge structure (XANES) this is multiple scattering, while for the higher kinetic energies in the extended X-ray absorption fine structure (EXAFS) region the back scattering from the next neighboring atoms dominates.

4.3.2.1 XANES

The region around the absorption edge provides information about the oxidation state and the coordination geometry of the probed atom.

In an atom with many electrons the outer ones are attracted to the positive charged nucleus but also repelled by the negative charge of the inner electrons. A positive oxidation state therefore means a more positive overall charge of the atom, which causes a stronger attraction on the inner electrons. Due to this stronger bond of the core electrons a higher energy is needed to remove them and the oxidation state of the atom can be determined by the energy shift of the edge as shown in figure 4.6 a.

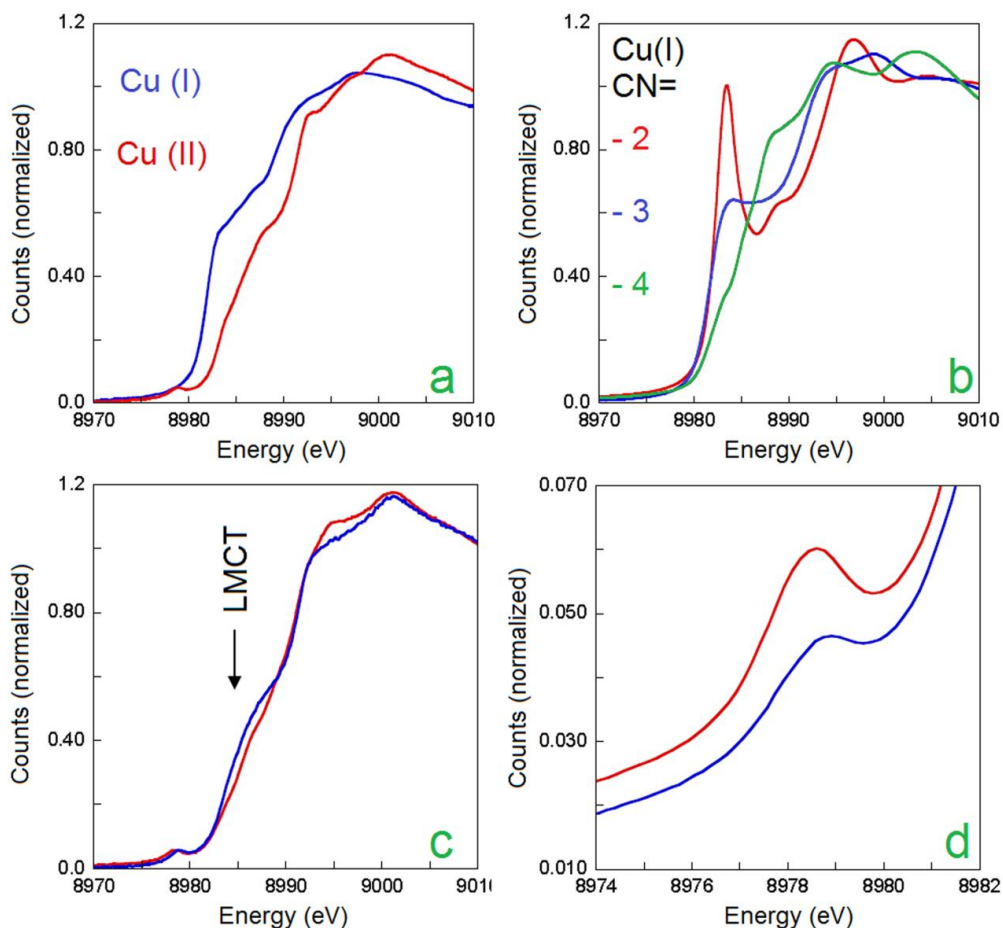


Figure 4.6 Structures at the Cu-K-absorption edge depending on oxidation state (a), coordination number (b), LMCT (c) and $s \rightarrow d$ transitions (d).

For K-edge spectra the dominant transitions are the $(1s \rightarrow np)$, where (np) is the lowest unoccupied (p)-orbital. This transition is very intense since it is a quantum-mechanically allowed electric dipole transition ($\Delta l = \pm 1$).

Figure 4.6 b shows the influence of the coordination number of the probed atom. The differences in the spectra of the three Cu complexes with the same oxidation state are evident and caused by different coordination numbers. In figure 4.7 the influence on the $(4p)$ energy levels of Cu(I) complexes with different coordination number is shown.

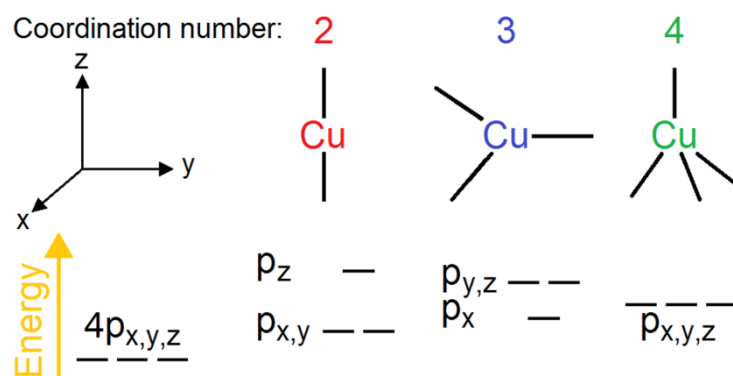


Figure 4.7 Effect of the coordination number on the $4p$ orbital of Cu

Furthermore charge-transfer bands in transition metal compounds, resulting from a shift of charge density between molecular orbitals (MO) that are predominantly from the probed atom and those that are predominantly ligand in character, alter the shape of the edge (see figure 4.6 c). If the transfer occurs from the MO with ligand-like character to the metal-like one, the complex is called a ligand-to-metal charge-transfer (LMCT) complex. Figure 4.8 illustrates the energy levels of probed atom and ligand in ground state (a), direct ($1s \rightarrow 4p$)-transition (b) and ($1s \rightarrow 4p$) plus ligand-to-metal charge transfer transition (c).

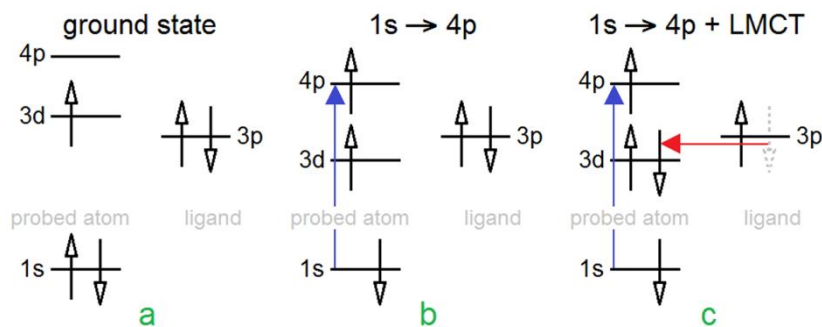


Figure 4.8 Illustration of the energy levels involved in LMCT

When probing atoms with unoccupied d orbitals ($1s \rightarrow (n-1)d$)-transitions can be observed in the XANES spectra at an energy slightly below the edge (figure 4.6 d). Although this transition is forbidden by dipole selection rules, it can be observed due to $(n-1)d + np$ mixing and electric quadrupole allowed transitions. This so called pre-peak has a lower intensity; roughly two orders of magnitude lower than the edge, but can strongly increase in suitable coordination geometries. The sensitivity to $d + p$ mixing can be used as probe of the geometry since the intensity increases with the distortion from a centro-symmetric environment as for example shown in figure 4.9 by means of the octahedral manganese oxide (MnO) without and the tetrahedral sodium permanganate (NaMnO_4) with distinct pre-peak.

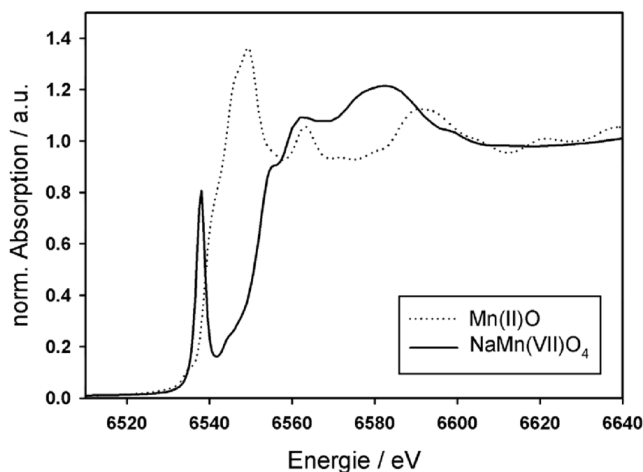


Figure 4.9 XANES spectra of the Mn-K-edge on a octahedral (dotted) and tetrahedral (solid) compound. [61]

4.3.2.2 EXAFS

The EXAFS region typically starts some tens of eV above the absorption edge, when the de Broglie wavelength becomes comparable with the interatomic distance. The photoexcitation cross-section is then modulated by the interference between the outgoing and backscattered photoelectron waves as illustrated in figure 4.10.

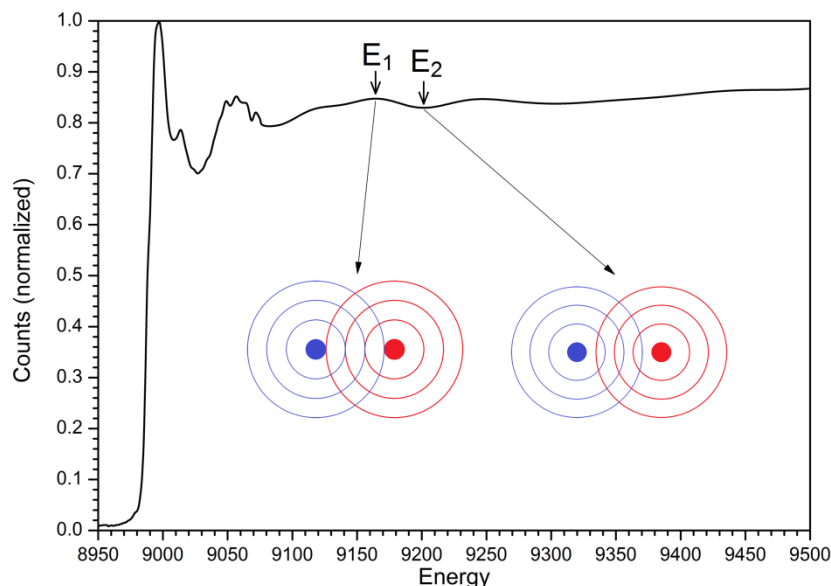


Figure 4.10 Origin of the EXAFS oscillations

At energy E_1 the absorption coefficient has a local maximum since the outgoing wave and the backscattered wave are in phase and interfere constructively, while at energy E_2 the photoelectron has a higher energy (shorter wavelength) and the waves interfere destructively resulting in a local minimum of the absorption coefficient.

Since XAFS is an interference effect it is better to think in terms of wavenumbers

$$k = \sqrt{\frac{2m_e(E-E_0)}{\hbar^2}} \quad (4.10)$$

rather than in energy.

The EXAFS ($\chi(k)$) is typically defined as the modulation in the absorption coefficient

$$\chi(k[E]) = \frac{\mu(E) - \mu_0(E)}{\mu_0(E)} \quad (4.11)$$

where $\mu(E)$ is the observed absorption coefficient and $\mu_0(E)$ the one from an isolated atom (see figure 4.11). Since $\mu_0(E)$ usually cannot be measured it is approximated by fitting a smooth spline function through the data. The division by $\mu_0(E)$ normalizes the oscillations "per atom" and the EXAFS then represents the average structure around the absorbing atoms.

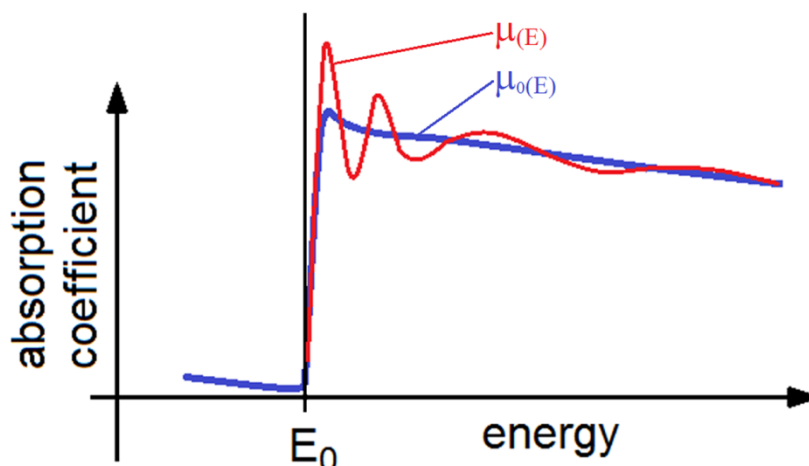


Figure 4.11 The EXAFS oscillations for a "isolated" atom in blue and for a bound atom in red.

$\chi(k)$ typically looks like shown in figure 4.12 when multiplied with k^3 to enhance the oscillations for higher k .

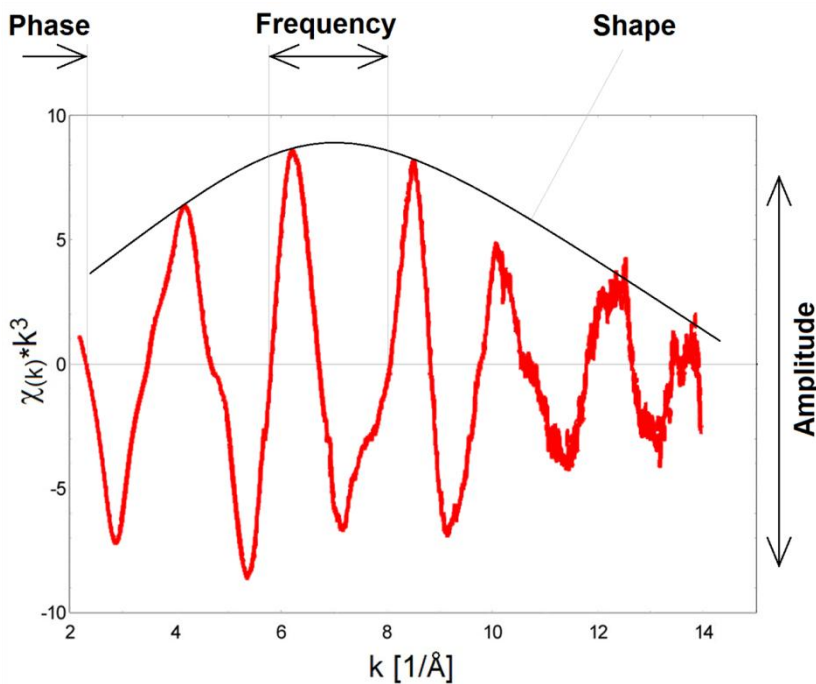


Figure 4.12 Normalized EXAFS oscillations multiplied by k^3 .

The important features of this spectra are:

- the amplitude - proportional to the number of scatterers (coordination number)
- the frequency - inverse proportional to the distance absorber to scatterer
- the shape - depending on the identity of the scattering atom.

For quantitative analysis an equation for $\chi(k)$ including the summation over all scattering

atoms (j) near the probed atom can be derived as

$$\chi_{(k)} = \sum_j \frac{N_j S_0^2 A_{j(k)}}{k R_j^2} e^{-\frac{2R_j}{\lambda_{(k)}}} e^{-2k^2 \sigma_j^2} \sin(2kR_j + \phi_{j(k)}) \quad (4.12)$$

with the primary parameters of interest for the coordination chemistry N_j as the number of scattering atoms and R_j as the distance between absorber and scatterer.

The amplitude $A_{j(k)}$ and the phase $\phi_{j(k)}$ contain the information to identify the scattering atoms, but unfortunately the dependence is very weak and thus a precise identification is often difficult. For example it cannot be distinguished between oxygen and nitrogen or sulfur and chlorine while it can be distinguished between oxygen and sulfur.

Limiting factors for the distance that can be sampled by EXAFS is the decreasing amplitude of the photoelectron ($\frac{1}{R^2}$), the (S_0^2) -term and the two exponential amplitude reduction terms. The (S_0^2) -term considers the inelastic loss processes and is typically taken as constant in a range $0.7 < S_0^2 < 1.0$ for a given absorbing atom. The first exponential term arise from the mean free path of the photoelectron $\lambda_{(k)}$, while the second - expressed by the Debye-Waller factor σ_j - results from the fact that there is more than one absorber-scatterer distance and each distance contributes slightly different to $\chi_{(k)}$. With this terms the EXAFS information is limited to atoms in the near neighborhood (typically within about 5Å) of the absorbing atom.

Equation (4.12) is based on a plane-wave approximation, which for energies far above the edge and long absorber scatterer distances is a reasonable assumption, however for most of the useful EXAFS region it is not. Nowadays various corrections as e.g. a spherical wave correction to amplitude and phase are made leading to a distance dependency of A_j and ϕ_j .

Another important correction is to take into account the possibility of multiple scattering. Multiple scattering pathways like $A \rightarrow S_1 \rightarrow S_2 \rightarrow S_1 \rightarrow A$, as illustrated with green arrows in figure 4.13, are of particular importance for low energy photoelectrons and can contribute much stronger to the EXAFS oscillations than single scattering pathways $A \rightarrow S_2 \rightarrow A$ (illustrated with grey arrows).

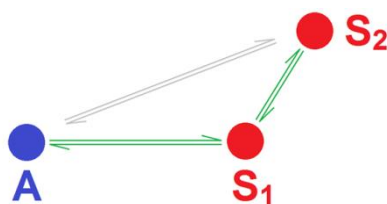


Figure 4.13 Illustration of multiple (green) and single scattering pathways (grey).

Other corrections to equation (4.12) like multiple electron excitation from the absorbing atom creating a double-hole configuration [68, 69] or the scattering at potential barriers from free atoms embedded into the condensed phase [70, 71]. These effects are only visible in the region near the edge which is very sensitive to the background subtraction. Thus it is not always possible to know which phenomenon is responsible for the oscillation. Anyway, since these effects are typically very weak they can be ignored most of the times.

4.3.3 Micro-XRF and micro-XAFS

X-ray absorption spectroscopy (XAS) became one of the most common methods to determine the chemical and structural properties of matter by measuring the spectral features of the X-ray absorption coefficient (μ). These measurements are performed by using a monochromator to tune the energy of the X-ray beam around the absorption edge energy of the studied element.

Due to the analytical power of this method it is not surprising that many synchrotron sources around the world are operating beamlines with high resolution monochromators which provide the possibility of XAS measurements for almost every element. Since the energy resolution of the monochromators is better at lower energies and the lifetime of the excited state is shorter, the XAS measurements for higher Z elements are often conducted at the L-edge, while for medium and low-Z elements the K-edge is used.

As already mentioned in the beginning of this chapter X-ray fluorescence spectroscopy (XRF) is a powerful tool for chemical analysis, which due to the development of new X-ray optical systems [5, 35, 72] during the last years, gained importance as a tool for analyzing samples on a micrometer and sub-micrometer level called micro-XRF. The high spatial resolution has proven to be essential for understanding material properties and for monitoring biological, chemical and physical processes [73-75]. With third generation synchrotron sources micro-XRF setups, having focusing optics with beam sizes down to tens of nm, the analysis of the composition of very small structures is possible.

Combining a focused beam with a high resolution monochromator allows to perform micro-XAS measurements, which is particularly useful in many fields of science as e.g. in geochemistry [76], biology [77] and others [78-80]. The focusing optics used for micro-XAS measurements are capillary lenses [81] or Kirkpatrick-Baez-mirror systems [82-84], and Fresnel zone plates [78] for the sub- μm regime.

Compound refractive lenses (CRL) are also able to produce sub- μm spot sizes but each lens is designed for one certain energy with a narrow bandwidth and therefore the spot size is sensitive to changes in the energy. Preliminary measurements at the *BAMline* already showed that this obstacle may be overcome by accepting a slightly enlarged beam or by adjusting the distance between CRL and sample continuously [10].

5 Experimental setup

5.1 Berliner Elektronen Speicher SYNchrotron (BESSY)

Nineteen-Ninety-Four was the groundbreaking year for the electron storage ring (BESSY II) at the Science and technology park WISTA (Wissenschafts- und Wirtschaftsstandort Adlershof) in Berlin-Adlershof. BESSY II is a 3rd generation synchrotron source consisting basically of an electron gun, a microtron, an injector, the synchrotron with 96 m and the storage ring with 240 m circumference shown in figure 5.1.

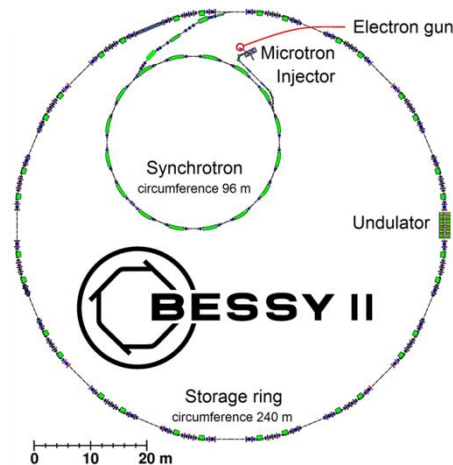


Figure 5.1 Main components and dimensions of BESSY II. (adapted from [85])

The electrons coming from the electron gun with 70 keV are accelerated in a microtron to 50 MeV and reach their final energy of 1.7 GeV within the synchrotron before they are injected in the storage ring where they are permanently accelerated to keep their velocity of $v=299\,792.44$ km/s (cp. $c=299\,792.4581$ km/s).

The storage ring is usually operated in three different modes, the

- **Multibunch mode:** This is the most used operation mode where about 360 electron-bunches are circling the storage ring. The bunches are filled in a so called hybrid mode which means that there are about 360 equally filled bunches with a time gap of 2 ns while there is one more intense bunch in the middle of a 100 ns gap. The interval for the injections is usually eight hours and the ring current after the injection is about 300 mA.
- **Singlebunch mode:** In this mode only one bunch of electrons is in the storage ring passing each station once every 800.5515 ns according to ring energy and circum-

ference. This mode is offered about 4 weeks per year and well suited for time resolved measurements. The interval for the injections is usually 4 hours and the maximal ring current is about 20 mA.

- **Low-Alpha mode:** This mode can be operated in a single- or multi-bunch form. The individual bunches contain only a small amount of electrons but therefore they are spatially concentrated so that the radiation is emitted in very short pulses of 1-2 ps compared to 50 ps in the normal modes. While in Multi- and Singlebunch mode all insertion devices are active, in Low-Alpha mode only a few can be used and therefore this mode is only offered occasionally mostly on Sundays with 0.1 mA per bunch.

During normal operation the 46 beam holes at the undulator, wiggler, and dipole sources emit radiation pulses which are extremely brilliant and range from the long wave terahertz region to hard X-rays (6 meV-150 keV). BESSY II offers users a big variety of energy ranges and polarizations at more than 50 beamlines each with their own outstanding properties. In addition, as a result of the radiometry activities of the Physikalisch-Technische-Bundesanstalt (PTB), BESSY II is the European radiation standard for the calibration of light sources and detectors.

Experimental stations at BESSY offer a big variety of methodical possibilities as e.g.:

- X-ray fluorescence analysis (XRF)
- X-ray absorption spectroscopy (XAS)
- X-ray diffraction (XRD)
- X-ray microscopy
- X-ray lithography
- X-ray emission spectroscopy (XES)
- Photoelectron spectroscopy (PES)
- Photo emission electron microscopy (PEEM)
- Femtoslicing

5.2 BAMline

The Bundesanstalt für Materialforschung und -prüfung (BAM), the German Federal Institute for Materials Research and Testing, and the Physikalisch-Technische Bundesanstalt (PTB), the German National Institute for Metrology, have built the first hard X-ray beamline at the storage ring BESSY II [8]. While most of the beamlines at BESSY II use bending magnet radiation with monochromatic energies up to 10 keV, the usable energy range at the BAMline is about 5 to 60 keV for monochromatic radiation and up to 200 keV for undispersed radiation.

A schematic overview of the elements in the BAMline is shown in figure 5.2.

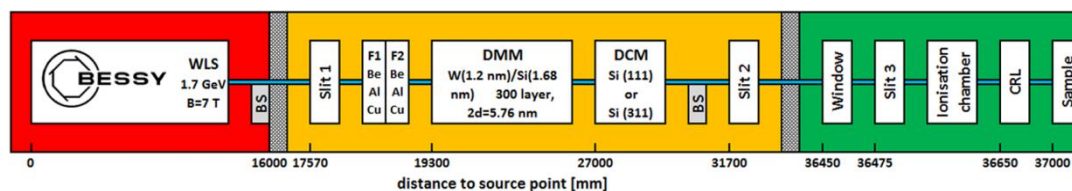


Figure 5.2 Schematics of the BAMline @ BESSY-II. The red marked area is the part of the beamline within the storage ring walls, the orange area the so called optical hutch and the green area the experimental hutch.

The beamline can be divided in 3 areas; the first part (marked in red) is within the storage ring wall and includes the X-ray source for the beamline - the superconducting 7 T wavelength shifter (WLS) - and the main beam shutter. This part is only accessible by BESSY personal and only during a complete shutdown. The main beam shutter guarantees the access to the second part of the beamline even if the Synchrotron is operational. This orange marked part is called the optical hutch and contains the main optical elements of the BAMline, a double-multilayer-monochromator (DMM) and a double-crystal-monochromator (DCM). Next to these devices there are also two racks of filters (F1, F2), two slit systems to form the beam and block scattered radiation (Slit1, Slit 2) and another beam shutter. This beam shutter allows accessing the experimental hutch without closing the main shutter, which has the advantage that the heat load on the optical elements due to the radiation does not change every time this hutch is opened. The green marked part of the beamline has as fixed elements the radiation exit window, another slit system (Slit3) and an ionization chamber. The BAMline is designed as a multipurpose beamline [86] with the possibility of mounting different setups for: X-ray fluorescence analysis (XRF) and μ -XRF by using a CRL, X-ray absorption fine structure (XAS) [87, 88] X-ray diffraction (XRD), absorption topography [89], reflectometry [90], detector calibration and characterization [91], dosimetry [92], μ -CT (Computed Tomography) [93] and more.

5.2.1 The superconducting 7 T wavelength shifter

The WLS is integrated in a straight section of the storage ring and shifts the emitted spectrum, radiated from electrons with moderate energies, to higher energies. For electron energies of 1.7 GeV the characteristic energy of the 7 T WLS at the BAMline is 13.5 keV while for a 1.3 T bending magnet it is only 2.5 keV. This leads for a ring current of 100 mA to calculated spectral photon flux densities as shown in figure 5.3.

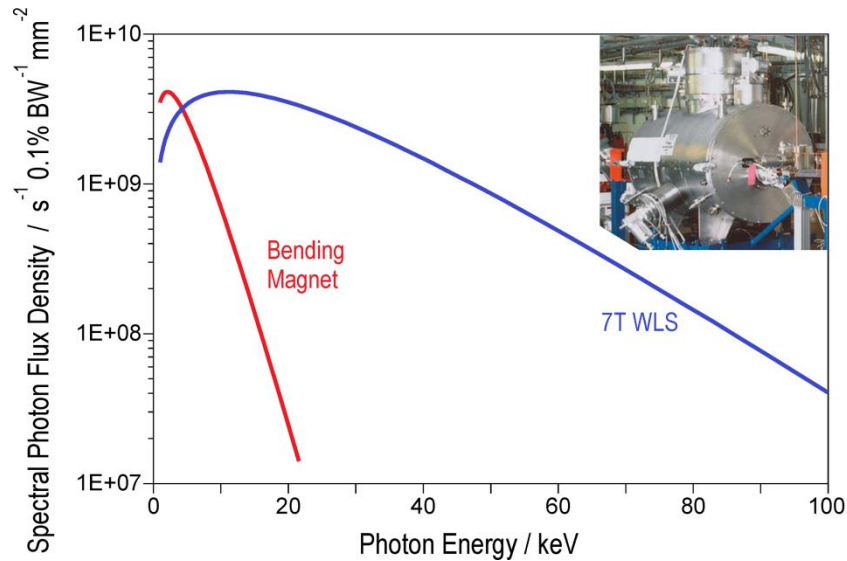


Figure 5.3 Spectral Photon Flux of a 1.3T bending magnet and a 7T wavelength shifter. The inset shows a picture of the WLS installed in the storage ring of BESSY II.

From the three poles of the WLS, only the central pole has a 7 T high magnetic flux density (homogeneity of 10^{-4} at 7 T) and is used for the generation of SR. The two side poles should only compensate the deflection of the beam and their magnetic field should be chosen as low as possible to reduce the contribution of the so-called “second source”. The side poles of the BAMline WLS have about 1.5 T and therefore they radiate a spectrum comparable with the one of the bending magnets. The use of three-pole wigglers cause for example a deviation of the equilibrium electron orbit and a shifting of the radiation point and therefore two additional steering magnets are placed at the both ends of the straight section to compensate the orbit deviation.

The iron yoke is designed to keep the whole magnetic flux inside of the magnet so that the stray field cannot influence other elements of the storage ring. The coils of the superconducting central pole are reeled out of an Nb-Ti wire impregnated with an epoxy compound. The wire has a diameter of 0.85 mm and its critical current is 360 A at 7 T.

The WLS magnets are integrated into a liquid helium cryostat. The liquid helium filled inner vessel is surrounded by two screens (20 K and 60 K) consisting of several layers of super-insulation to reduce the heat flux into the helium volume. The helium vessel is isolated from the external vessel by a 10^{-7} mbar vacuum insulation.

The main parameters of the wavelength shifter are:

- Maximum field (central pole): 7 Tesla
- Field at side poles: 1.5 Tesla
- Liquid helium consumption: 0.2 l/h
- Total radiated power (@ 1.9 GeV, 500 mA): 13 kW
- Field stability (@ 7 T): 10^{-4}
- Field homogeneity (@ 7 T): 10^{-4}

A more detailed description of this particular wavelength shifter can be found at Borovikov et al. [9].

Measurements carried out by S. Zabler [94] using an imaging setup and different gratings showed an average angular divergence of $1.16 \pm 0.21 \mu\text{rad}$ in the vertical and $4.69 \pm 0.17 \mu\text{rad}$ in the horizontal plane. Corresponding to this, the size of the beam at the source is $40.6 \pm 7.2 \mu\text{m}$ in the vertical and $164.0 \pm 5.8 \mu\text{m}$ in the horizontal plane which matches very good with the calculated values. The three-dimensional Gaussian profile in figure 5.4 shows the simulated X-ray intensity distribution at the source.

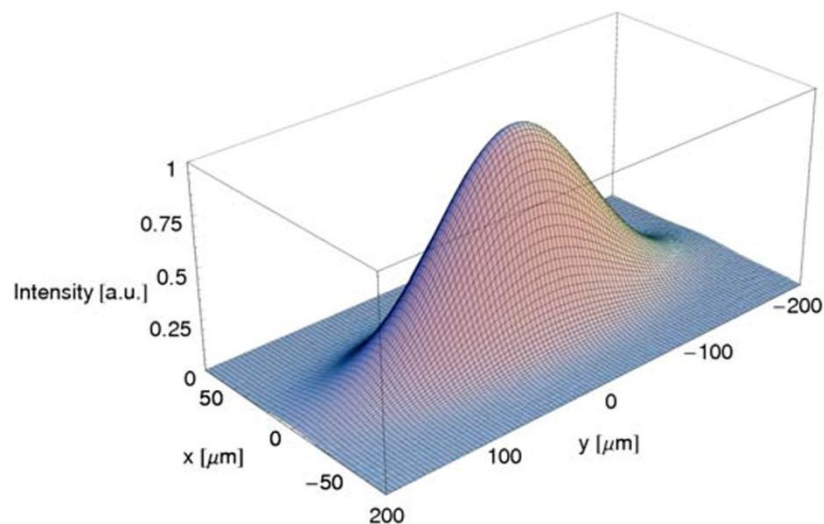


Figure 5.4 Simulation of the X-ray source intensity distribution for the BAMline (from S. Zabler [94])

5.2.2 The beam shutter

The beam shutters are massive blocks of tungsten built to completely absorb the radiation from the WLS. The shutters are part of the radiation protection system and therefore integrated in the interlock system which only allows access to the hutches when there is no radiation.

5.2.3 The slit system

Slit1 is the first optical device of the beamline accessible by the user. The system consists of four independent moveable tantalum plates which are attached to water cooled copper plates to remove the heat load from the impinging radiation. The plates are mounted one after another to avoid collisions of the plates due to handling errors. The last optical device in the hutch is Slit 2 and it is built in the same way.

5.2.4 The filter rack

There are two independent moveable and water cooled filter racks each of them can hold five filters of different material and thickness. The filters are necessary to eliminate low energy photons or generally reduce the photon flux on the sample which is needed for some experiments. The filters chosen for the *BAMline* are listed in table 5.1 and the spectral photon flux density calculated for a ring current of 100 mA and an area of 1 mm² at the place of the experiment is shown in figure 5.5.

Table 5.1 Materials and thicknesses of the filters at the *BAMline*.

Position	1	2	3	4	5
Rack F1	Be 0.6 mm	Cu 0.2 mm	Al 0.2 mm	Al 1.0 mm	no filter
Rack F2	Be 0.2 mm	Cu 0.05 mm	Cu 1.0 mm	Al 0.5 mm	no filter

The filters can be used separately but also every combination of F1 and F2 is possible. For example in the lowest energy range usually both Be filters are used, for the next energy range the Be 0.2 mm plus the Al 0.2, and so on.

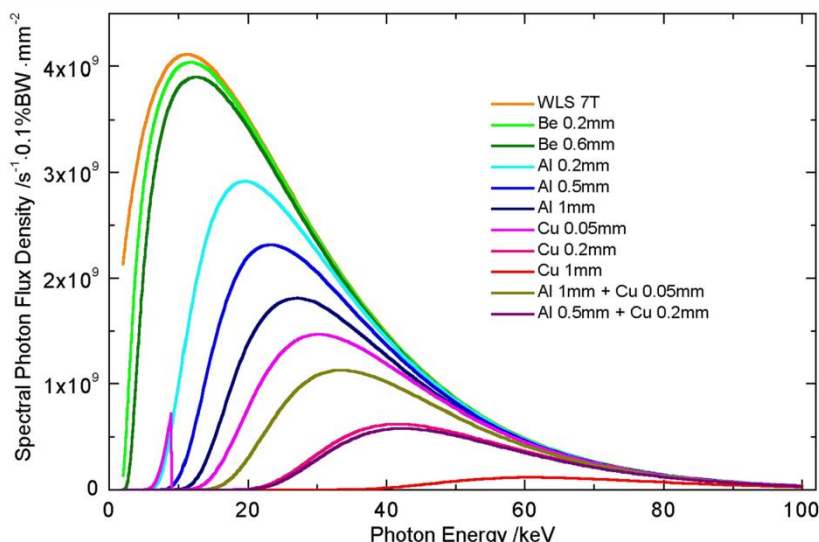


Figure 5.5 Photon flux density after the WLS and with the different filters

5.2.4 The double multilayer monochromator

The mirrors of the DMM consist of a 300 mm × 60 mm single crystalline Si substrate covered with a W/Si multilayer (ML) coating. The thicknesses of the single layers are 1.2 nm for the W- and 1.68 nm for the Si- layers resulting in a $2d$ spacing of 5.76 nm. The ML mirrors are mounted on separate goniometers and the second mirror additionally on a translation stage of 1m range. This allows to operate over a broad energy range with a constant offset (fixed exit mode), e.g. in the range from 8 keV to 35 keV the offset is fixed at 12 mm. Moreover, the second ML it is mounted on a meridional bending mechanism developed at BAM where the radius can be varied from >10 to 1.5 km in order to collimate or focus the beam to a minimum vertical focus size of less than 0.1 mm.

Figure 5.6 shows the calculated spectral photon flux density of the DMM with 100 mA ring current on a 1 mm² area at the site of the experiment.

The black line shows the photon flux density of the WLS calculated with a bandwidth of 2 % and the blue line the one with the DMM ($\frac{\Delta E}{E} = 1.6 \%$). The red graph shows the spectral distribution of the photon flux at an angle of 1.58° or 8 keV (1st order) with the second and third order reflection. The green graph shows the calculated energy resolution of the ML as a function of the energy. Since the transmitted power is proportional to the area under the red curve, while the rest is absorbed within the first ML, the necessity of cooling the mirror is obvious. The strong changes in the reflectance around 10 keV are a consequence of the W-L absorption edges of the ML coating.

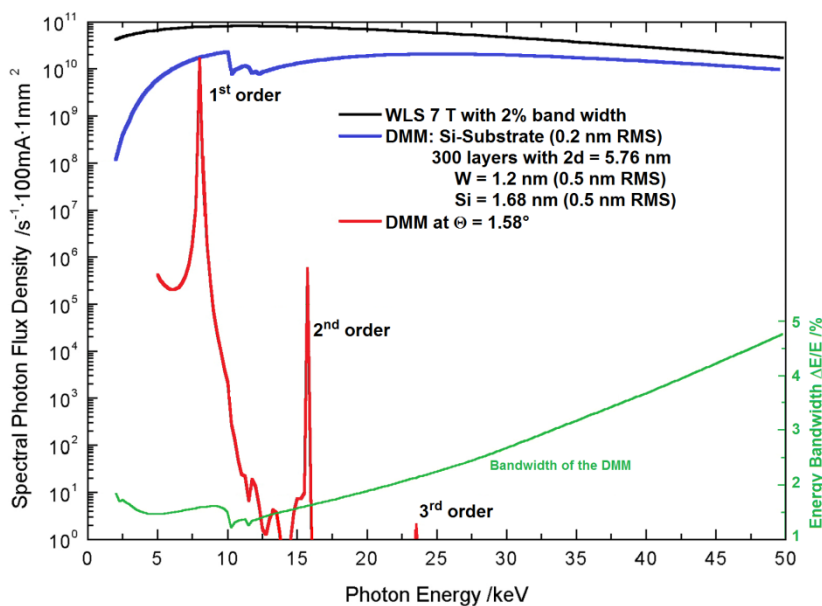


Figure 5.6 Flux and resolution of the BAMline DMM

5.2.4 The double crystal monochromator

The two crystals of the DCM are mounted on the same goniometer, where the first crystal is fixed and the second crystal can be moved in x-y-direction to achieve a fixed exit mode. Since the Bragg condition has to be satisfied for both crystals and the energy bandwidth of the crystals is very low ($\frac{\Delta E}{E} \approx 0.02\%$), a very precise alignment of the two crystals is necessary. Manufacturing tolerances of the linear stages and other mechanical parts can cause a reduction of the photon flux or even the loss of the beam when the energy is adjusted. To compensate this, the second crystal has additional actuators installed (pitch and roll) which allow tilting crystal relative to the first. The angle between the two crystals (pitch) can be also fine-adjusted by a piezo translator which is also used as part of a monochromator flux stabilization scheme called MOSTAB (Modular Stability Derivative Program, a HASYLAB concept). Additionally the second crystal is mounted on a sagittal bender (ESRF type) allowing a bending radius down to a minimum value of 1 m leading to a minimum horizontal focus size of about 0.25 mm.

Due to the smaller bandwidth the heat load on the first crystal is even higher than on the first ML and therefore it is mounted on a water-cooled Cu block. To reduce the heat load on the first crystal when using high energies the water-cooled filters can be used to absorb the low energy photons and for lower photon energies the DMM can be used as a pre-monochromator. Next to the reduction of the heat load the DMM also reduces the higher harmonics very effectively. Also it can be used as a collimator by bending the second mirror and

thus improves the energy resolution of the DCM, which is dominated by the divergence of the incident beam.

The calculated photon flux density of the DCM with the two at the BAMline available crystal pairs is shown in figure 5.7.

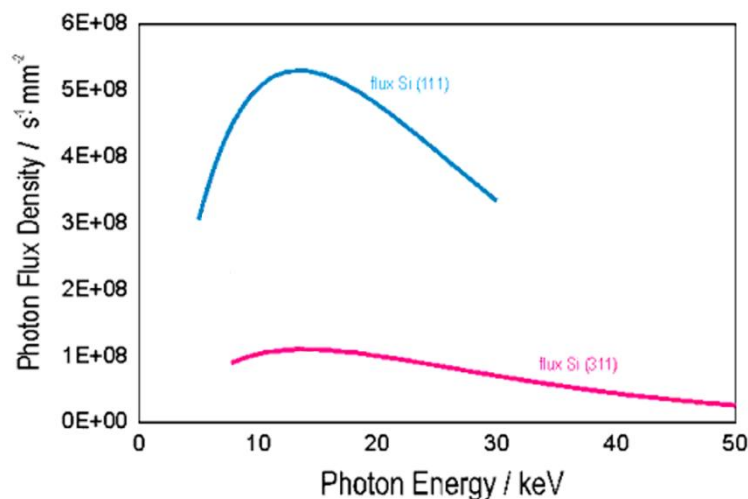


Figure 5.7 Flux and resolving power of the BAMline DCM

It is obvious that the photon flux is much lower than with the DMM but therefore the resolving power is much better.

When bending the second mirror of the DMM and the second crystal of the DCM a focused beam with a size of about 0.25 mm in horizontal and 0.1 mm in vertical direction can be reached. The beam paths are shown in figure 5.8.

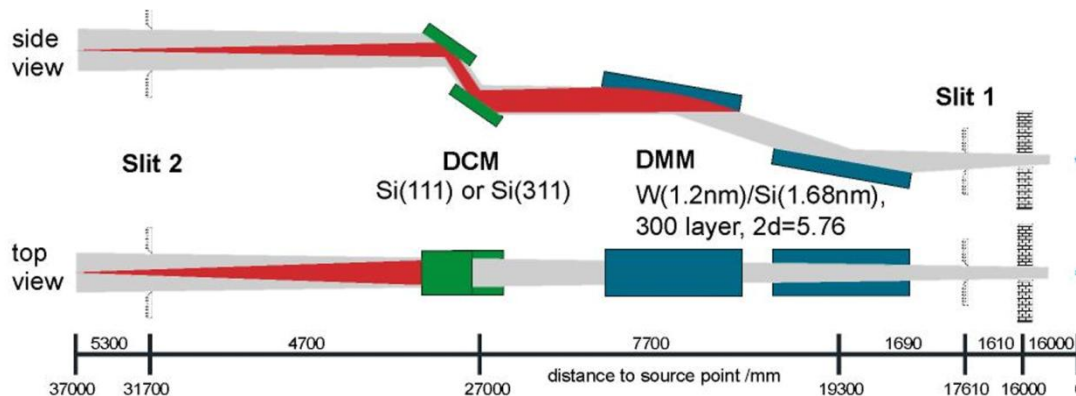


Figure 5.8 Schematics of the beam path of a unfocused (gray) and a focused beam (red) at the BAMline in side and top view.

5.3 The imaging setup

The micro-imaging setup (a detailed description can be found at Rack et al. [95]) is mounted on a table which can be moved in and out of the experimental hutch for a fast exchange with other setups. The table includes a five axis motorized sample stage, a 1.1 m travel range airbeared linear stage and a detector system (see figure 5.9).

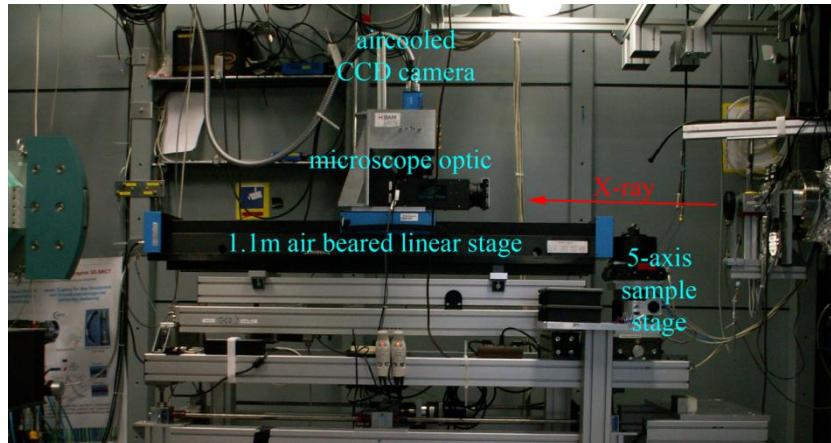


Figure 5.9 Picture of the imaging setup at the BAMline with the sample manipulators, the 1.1 m linear stage and the imaging optic.

The whole setup can be lifted or lowered as well as pivoted to adjust pitch and yaw in order to align the camera translation parallel to the beam. For high resolution imaging a commercial microscope system is used, designed in close cooperation between the ID22 group of the ESRF and Optique Peter (Optical and Mechanical Engineering, France) [96]. The microscope is comparable to a common light microscope with a motorized revolver objective holder for up to three different objectives to obtain resolutions from several micrometers down to the sub-micrometer range. The CCD camera is directly mounted on the microscope, which is attached to a linear stage (Johann Fischer Aschaffenburg, Germany) allowing a precise positioning of the optic at any distance up to 1100 mm from the sample.

The camera used for this work was the high resolution 14 bit Peltier cooled CCD camera system *pco.4000* (PCO AG, Germany [97]). Important features of the camera are:

- a resolution of 4008×2672 pixel
- a pixel size of $9 \mu\text{m} \times 9 \mu\text{m}$
- low noise down to 11e-rms
- fast image recording with 128 MB/s
- exposure times from $5 \mu\text{s}$ to 49 days

5.4 The X-ray fluorescence setup

The X-ray fluorescence (XRF) setup is mounted on an optical table and consists of a 4-axis motorized stage to adjust the sample, a long range microscope to observe and position the sample and an energy dispersive detector to collect the spectra.

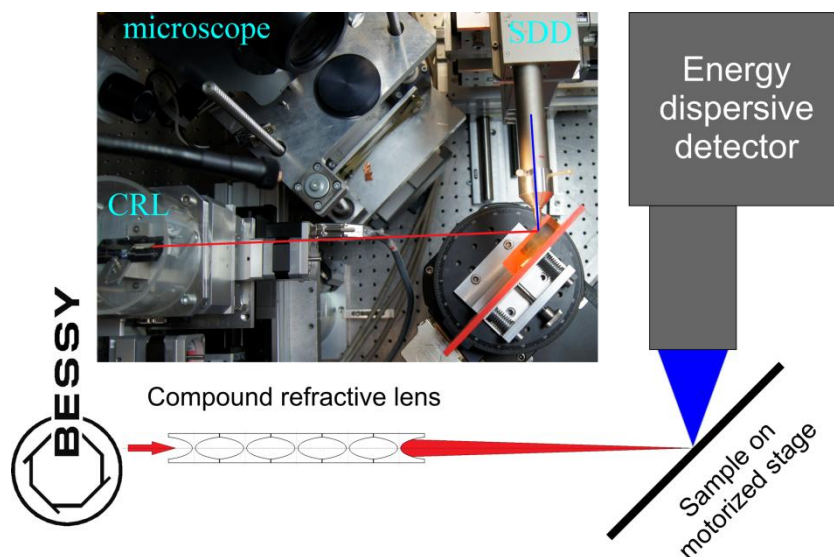


Figure 5.10 Schematics and photograph of the X-ray fluorescence setup at the BAMline with the CRL

A top view of the setup is shown in figure 5.10, where the CRL located at the left side focuses the X-ray beam (displayed in red). The focused beam irradiates the sample mounted on the sample stage equipped with three high precision linear manipulators and a rotation table (x -, y -, z - and ω -axis). With these manipulators the sample can be moved through the beam while the fluorescence radiation from the sample (displayed in blue) is collected with an energy dispersive detector, in this case with a silicon drift detector (SDD).

At the BAMline different Peltier cooled silicon drift detectors, as well as a Si(Li)- and a Ge-detector - both liquid nitrogen cooled and mainly used for high X-ray energies - are available.

5.5 The Color X-ray Camera

The BAM, the Institute for Scientific Instruments GmbH (IfG), the PNSensor GmbH, and the Institut für Angewandte Photonik e.V. (IAP) have developed and tested a novel X-ray detector system. The idea was to combine an energy dispersive array detector for X-rays the pnCCD [98], with polycapillary optics [99] to a so called Color X-ray Camera (CXC), a fullfield XRF imaging device.

The pnCCD chip has a sensitive thickness of about $450\ \mu\text{m}$ and an area of $12.7\ \text{mm} \times 12.7\ \text{mm}$, divided into 69696 (264×264) pixel of about $48\ \mu\text{m} \times 48\ \mu\text{m}$ each. The split frame mode allows a high frame rate of 400 Hz with an energy resolution of 152 eV for Mn-K $_{\alpha}$ (5.9 keV) at 450 kcps. The pnCCD is sensitive to photons up to 40 keV with a quantum efficiency of more than 95 % for energies until 10 keV and still more than 30 % for 20 keV photons. Due to its good spatial an energy resolution the chip was already used as detector in diffraction and scattering experiments.

In order to obtain a fluorescence image of an object an X-ray optic has to be placed between the detector and the object. This optic has to assure that photons originating from different spots on the sample are “guided” to the corresponding pixel of the chip. This can be achieved by a simple pinhole with a diameter in the order of (or smaller than) the pixel size. A big advantage of using such optics is that the magnification can easily be changed by varying the distances between sample, pinhole and detector. The disadvantage is that it leads to a significantly reduced photon flux at the detector chip. For the CXC, a polycapillary optic is used which contains a large number of straight channels to obtain a 1:1 image on the detector. The optics made by the IfG typically has a transparency in the order of 75 % to 80 %, leading to acceptable intensity losses. To magnify images another polycapillary has to be used, consisting also of a bunch of capillaries but conically arranged. Figure 5.11 shows e.g. a photograph of the CXC with a 1:6 magnifying polycapillary optic.

Further information about the Color X-ray Camera including a more detailed description of the pnCCD chip, the optics, the software and first test results can be found in the articles of Scharf, et al. [100] and Ordavo, et al. [101].

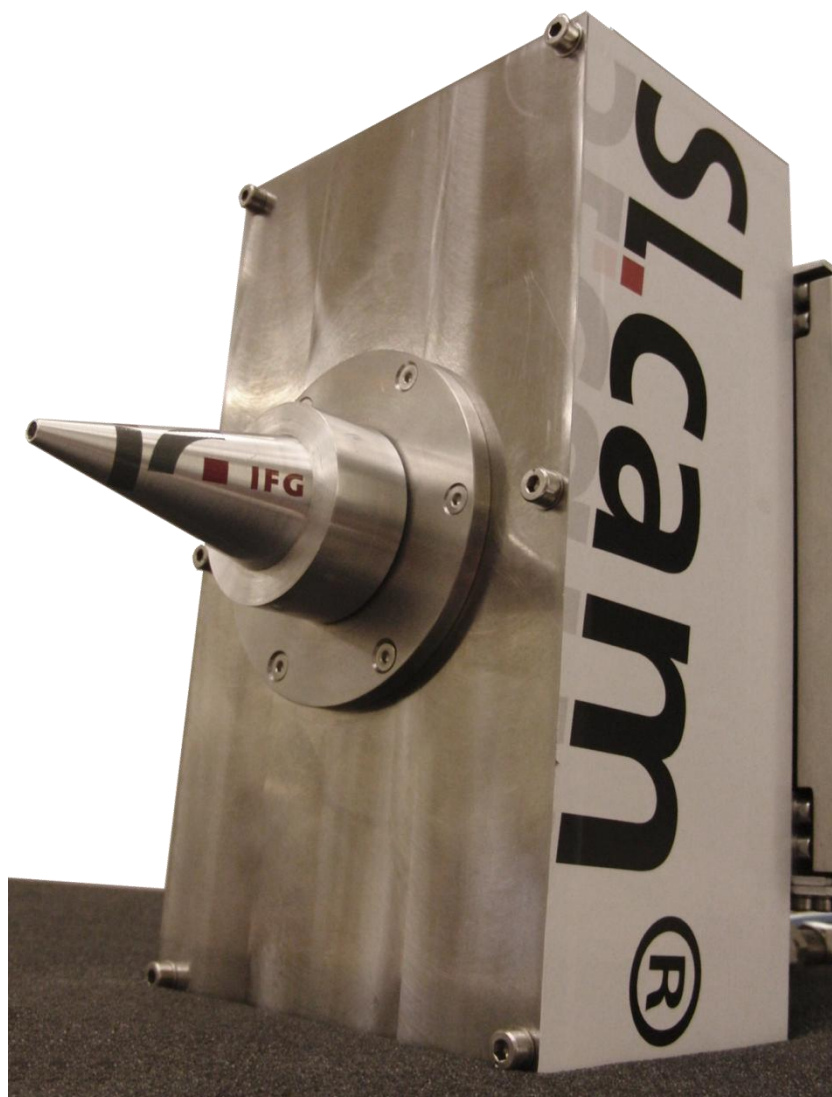


Figure 5.11 The Color X-ray Camera with a 1:6 polycapillary optic

6 Characterization of the CRL

6.1 Polymeric crossed planar parabolic CRL

The lenses used in this work were produced by the Institute of Microstructure Technology (IMT) Karlsruhe[102] using the so called LIGA-process, which is an acronym for Lithographie, Galvanik und Abformung (German for: lithography, electroplating and molding). With this process micro-structures can be manufactured in polymers or metals by electron beam lithography and deep X-ray lithography. The advantages of LIGA compared to other production techniques like embossing are that hundreds of well aligned lenses with a small curvature radius in the micrometer range and a smooth surface with a roughness in the 10 nm range can be made in only one step. The disadvantage is that only planar lenses can be produced by lithographic methods so that, to obtain a point focus, two sets of lenses are necessary. These two sets have to be tilted by 90° to each other (crossed) so that one can focus the beam in horizontal and the other one in vertical direction as shown in figure 6.1.

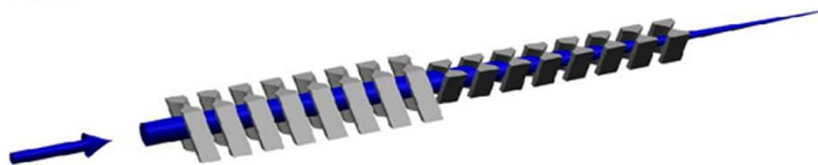


Figure 6.1 Two sets of planar lenses 90° tilted to each other to form a point focus. Source: [37]

The lenses from IMT consist of a stack of vertical and horizontal elements made out of SU-8 polymer, a widely used negative resist. The advantage of SU-8 is together with the transparency for X-rays (high transmission) its durability against radiation damage. More detailed information about the LIGA-process and this kind of compound refractive lenses in general can be found at the Homepage of the IMT (<http://www.imt.kit.edu/>) the webpage of Arndt Last [37] and in various papers like e.g. in Nazmov et al. [103-105].

For this kind of X-ray lenses the reachable focus size is in the 100 nm region depending on several factors like the size of the source, the distance between the source and the lens, the focal distance and the aperture of the lens. Many of these factors are predefined as for example the source size depends on the synchrotron parameters, the distance between lens and source is given by the beamline design and the apertures of the lenses are defined by the manufacturer.

At the 3rd generation synchrotron facility BESSY II the source size is 120 μm in horizontal and 50 μm in vertical direction and the distance between source and lens at the *BAMline* is about 37 m. After defining the energy for the lenses the focal distances can be chosen, only limited by the number of single lenses which fit on the lens plate or by the absorption losses through the lenses.

lens aperture [μm]	Lenses for 9 keV									Lenses for 50 keV			
	shortest poss. focus [mm]	min. focal length [mm]	gain	vert. size [μm]	horiz. size [μm]	const. focal length [mm]	gain	vert. size [μm]	horiz. size [μm]	shortest poss. focus [mm]	gain	vert. size [μm]	horiz. size [μm]
369	210	210	22000	0.46	0.86	250	20000	0.53	1.01	6280	400	10.50	24.70
279	124	124	27000	0.31	0.54	250	18000	0.53	1.01	3638	670	5.60	13.30
215	77	77	32000	0.21	0.36	250	16000	0.53	1.01	2217	1000	3.30	7.80
157	45	45	34000	0.14	0.23	250	13000	0.53	1.01	1227	1800	1.80	4.20
129	33	33	33000	0.12	0.18	250	11000	0.53	1.01	860	2400	1.28	2.95
85	17	30	40000	0.11	0.17	250	7600	0.53	1.01	371	5300	0.56	1.28
60	11	30	38000	0.11	0.17	250	4800	0.53	1.01	200	8700	0.31	0.70
41	8	30	32000	0.11	0.17	250	2600	0.53	1.01	105	13800	0.17	0.37

Table 6.1 Dependencies of focal length, spot size and gain on aperture and energy.

Table 6.1 shows the dependence of focal length and spot size on the aperture and energy for the 8 different apertures on a standard CRL-plate from IMT. As one can see for the three smallest apertures at 9 keV the focal length is limited by the length of the lens plate.

An upper limit for the focal length does not exist since (as shown in chapter 3) this, for a given material, depends only on the radius of the lens. Nevertheless for decreasing focal distances also the spot size decreases (see table 6.1) and therefore shorter foci are usually chosen.

The compound refractive lens plate #08-762P-JW13_a (see figure 6.2) consists of 16 lenses which are mounted on a silicon wafer, custom-made by the IMT, to match the conditions at the *BAMline*. Each lens was designed for a specific energy in the range of 5 keV to 33.2 keV chosen according to the absorption edges of the metallic impurities in solar cells like Ti, V, Cr, Mn, Co, Ni, Fe and Cu and other elements frequently measured in applications at the *BAMline*.

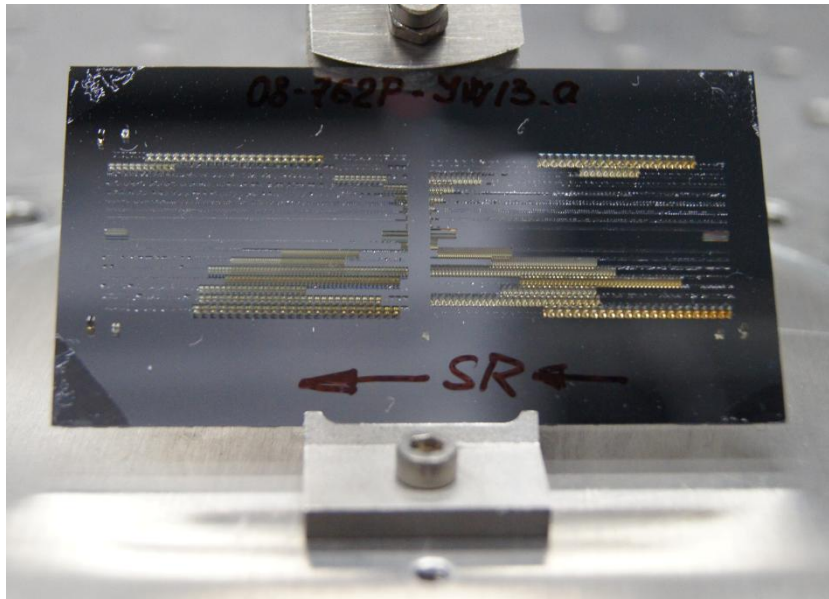


Figure 6.2 Photography of the CRL-plate used at the BAMline

Due to the distances at the experimental station, particularly the distance between beam exit window and sample stage the focal length for all lenses was aimed to be about 350 mm. This leads to a spot size of about 0.5 μm in vertical and 1.2 μm in horizontal direction. The key parameters of the lens plate like focal distance, focal size or number of single lenses can be found in table 6.2.

CRL-Plate #08-762P-JW13 a											
name of the lens	nominal energy [keV]	nominal focal length [mm]	lens elements vertical	misalignment vertical [μm]	lens elements horizontally	misalignment horiz. [μm]	lens aperture [μm]	estimated intensity gain	min. vertical focus size [μm]	min. horizont. focus size [μm]	lens for element
8t	9.0	350	21	-4.0	19	8.5	369	13900	0.50	1.21	Cu
7t	7.1	349	10	-1.0	9	9.5	279	10000	0.54	1.21	Fe
6t	8.3	348	10	10.0	10	6.5	215	13000	0.53	1.25	Ni
5t	7.7	359	6	-0.5	6	4.5	157	11300	0.56	1.19	Co
4t	6.5	318	4	0.5	4	9.0	129	9200	0.55	1.07	Mn
3t	6.0	341	2	3.0	2	6.0	85	5600	0.61	1.17	Cr
2t	5.5	400	1	3.5	1	6.0	60	2600	0.73	1.38	V
1t	5.0	220	1	2.5	1	5.5	41	2900	0.52	0.83	Ti
ADJUSTMENT DEVICE											
1b	13.4	317	5	1.5	5	0.5	41	3400	0.44	1.03	Ir-L
2b	33.2	350	43	0.5	41	-4.0	60	4900	0.47	1.18	I
3b	29.2	350	48	3.5	45	-0.5	85	10000	0.47	1.16	Sn
4b	25.5	350	58	4.0	54	-3.5	129	18000	0.46	1.17	Ag
5b	20.0	350	43	3.5	40	-3.0	157	22000	0.46	1.18	Mo
6b	11.6	350	20	8.0	18	-5.0	215	19000	0.48	1.21	Pt-L
7b	11.9	350	27	7.0	25	-4.5	279	19600	0.48	1.19	Au-L
8b	9.7	350	24	7.5	22	-5.0	369	15000	0.50	1.21	Zn

Table 6.2 Key parameters of the lens plate #08-762P-JW13_a.

6.2 Alignment of the CRL at the beamline

A precise alignment of the CRL according to the beam is crucial to achieve the best possible focus and therefore the lens plate has an adjustment device consisting of 2 vertical and 3 horizontal microstructures. To adjust the lens the vertical structures have to lie precisely on top of each other, while the 3 horizontal structures should not overlap. A radiograph of the well aligned lens plate is shown in figure 6.3.

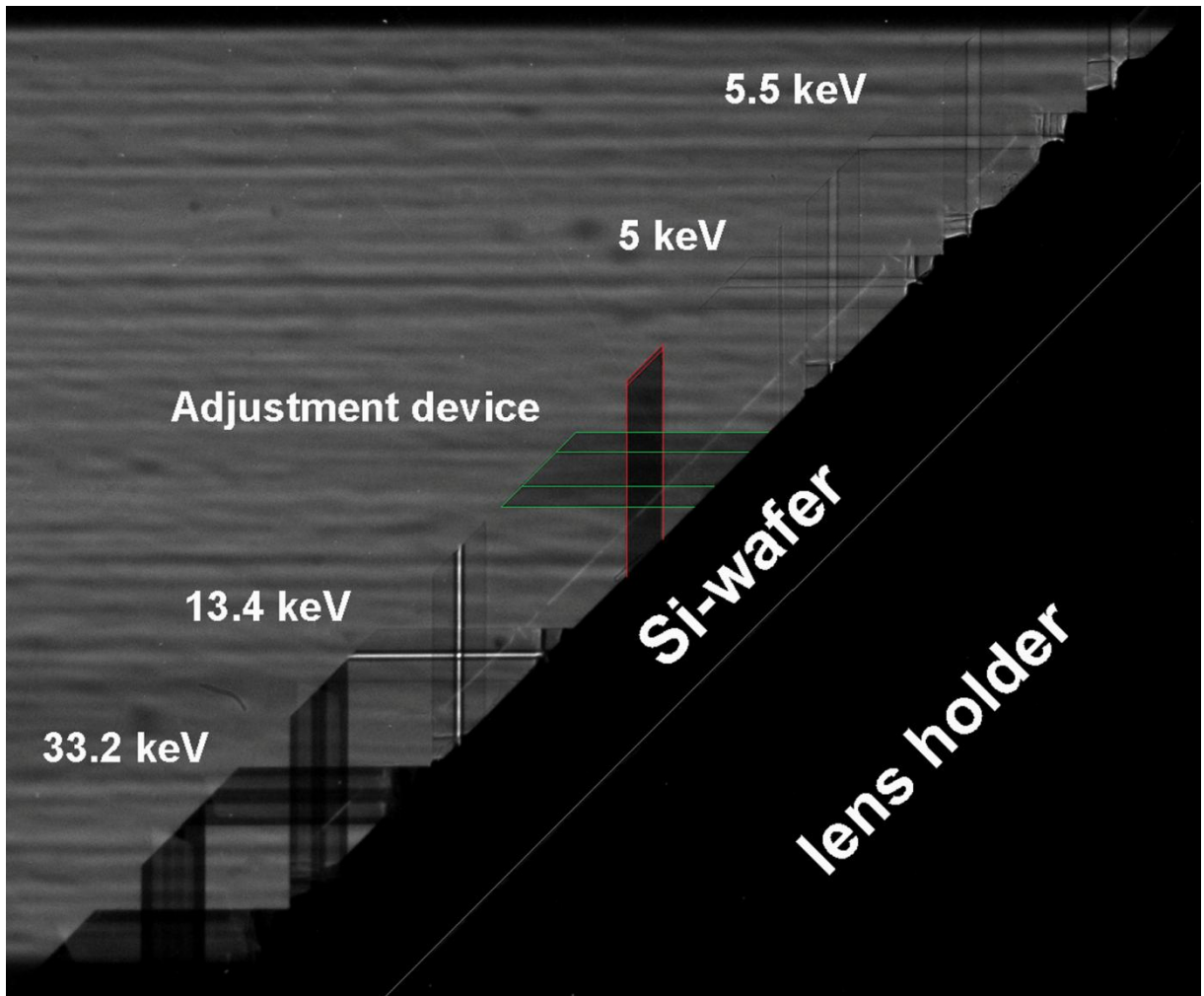


Figure 6.3 Radiograph of the adjusted lens plate. The two vertical structures (marked in red) lie on top of each other, while the three horizontal structures do not overlap and appear only as one structure.

For a precise alignment the compound refractive lens plate has to be mounted on a stack of 5 motorized stages (see figure 6.4), including two horizontal stages, one in direction (z-axis, E) and one perpendicular to the beam (x-axis, D), and a vertical stage (y-axis, C) as well as a circle goniometer (B) and a rotation stage (A) for the alignment of the horizontal plane and vertical plane of the lens respectively. In principle the precision of the linear stages which

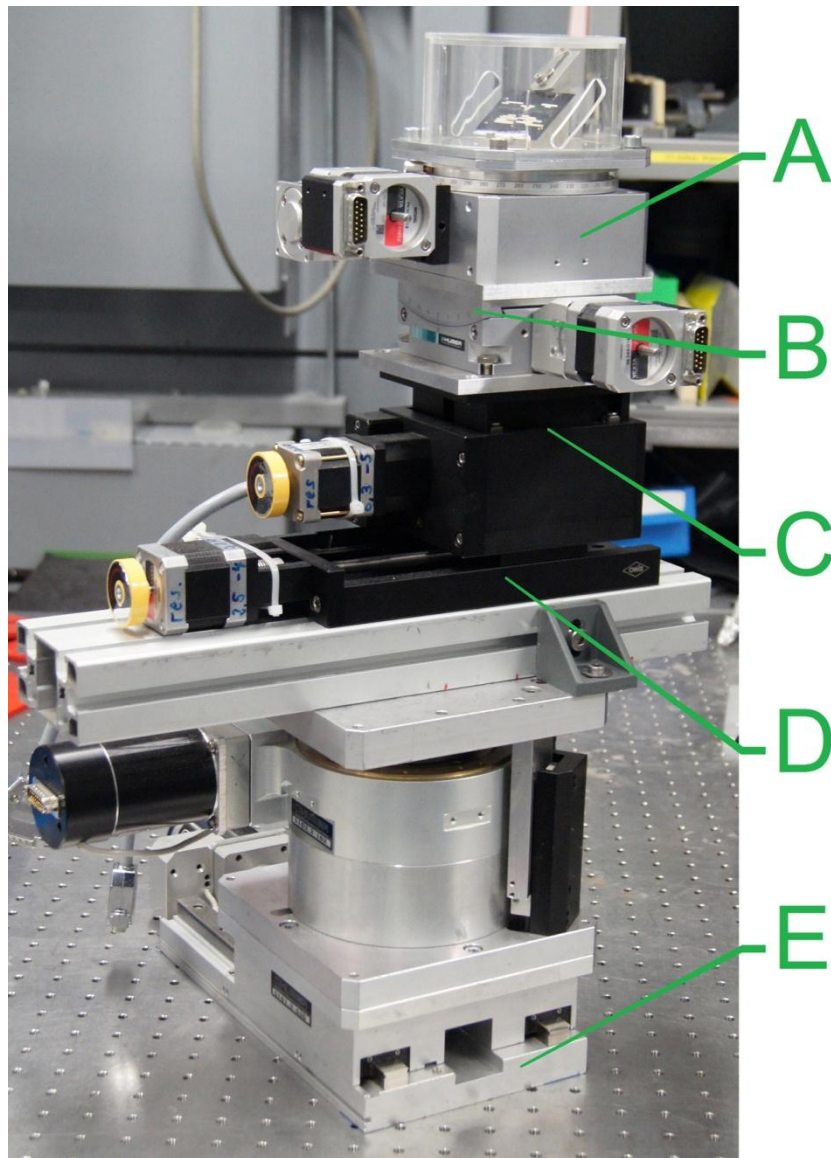


Figure 6.4 Photography of the motorized stage for the adjustment of the CRL.

move the lens in front of the beam does not have to be too good, but since it is sometimes necessary to move the lens unobserved in and out of the beam stages with repeatability in the μm range should be chosen. Hence the alignment of the vertical and horizontal plane is much more crucial, the precision of the goniometer and the rotation stage should be in the range of 0.001° ($\sim 17 \mu\text{rad}$).

Worth mentioning for figure 6.3 is that this picture was captured with the monochromator set to 13.4 keV which is the nominal energy of the lens 1b and therefore this lens produces a very well formed focal spot. Looking at the 33.2 keV lens (2b) in this radiography it is to see that the lens is opaque for the 13.4 keV photons, while the lenses for 5 keV and 5.5 keV seem completely transparent. This is of course just a matter of the focal distance which for these lenses would be about 1.8 meters at 13.4 keV, while the picture is taken in a distance of 317 mm from the center of the lens.

6.3 Focal distances of the lens plate

Because of the strong energy dependence of the refractive lenses they have to be operated with a monochromatic beam to reach the smallest possible spot size. At the *BAMline* two monochromators are available, a Double Crystal Monochromator (DCM) and a Double Multi-layer Monochromator (DMM). As shown in section 3.4 the spot size of refractive lenses is very sensitive to the photon energy bandwidth and therefore the DCM with an energy bandwidth of $\frac{\Delta E}{E} \approx 0.02\%$ should be used. Because of this small energy bandwidth the photon flux density of the DCM at 9 keV is about $5 \times 10^8 \text{ s}^{-1} \text{ mm}^{-2}$ (Goerner et al. [86]) which is about 100 times smaller than the one of the DMM with $7 \times 10^{10} \text{ s}^{-1} \text{ mm}^{-2}$ (Rack et al. [95]). The higher flux is caused by the much broader energy bandwidth of $\frac{\Delta E}{E} \approx 1.6\%$ of the DMM and therefore it is not the suitable device for reaching the smallest possible spot size. Since for many applications a smaller resolution might be sufficient and a higher flux preferred the influence of both monochromators was investigated.

To measure the focal distance of the lenses the imaging setup described in chapter 5 was used. Due to its design with the long linear stage aligned in direction of the beam is perfectly suitable for measurements of the spot size as a function of the distance. Even if the spot size cannot be distinguished as precise as with for example knife edge scans it does not matter since for this measurement only the changes in the spot size are relevant.

To conduct this investigation the CRL-plate was mounted on the sample stage (see figure 6.5) and adjusted using the adjustment device and the camera picture (see figure 6.3). The actual distance between the center of the lens and the scintillator was determined as precise as possible with a measuring tape and the motor position of the linear stage was correlated to this value by applying an offset.

To measure the focal length of the lens the camera unit was positioned according to the nominal focal distance of the lens and scans along the optical axis in a range of ± 50 mm with 2 mm step width and ± 25 mm with 1 mm step width were performed. At each point of the scan a picture was recorded with an exposure time between one and five seconds. The spot size was then calculated from the 16 bit pictures recorded from the camera as the sum of the pixels in the image where the grayscale value was higher than 50 % of the maximum (FWHM) under consideration of the background value.

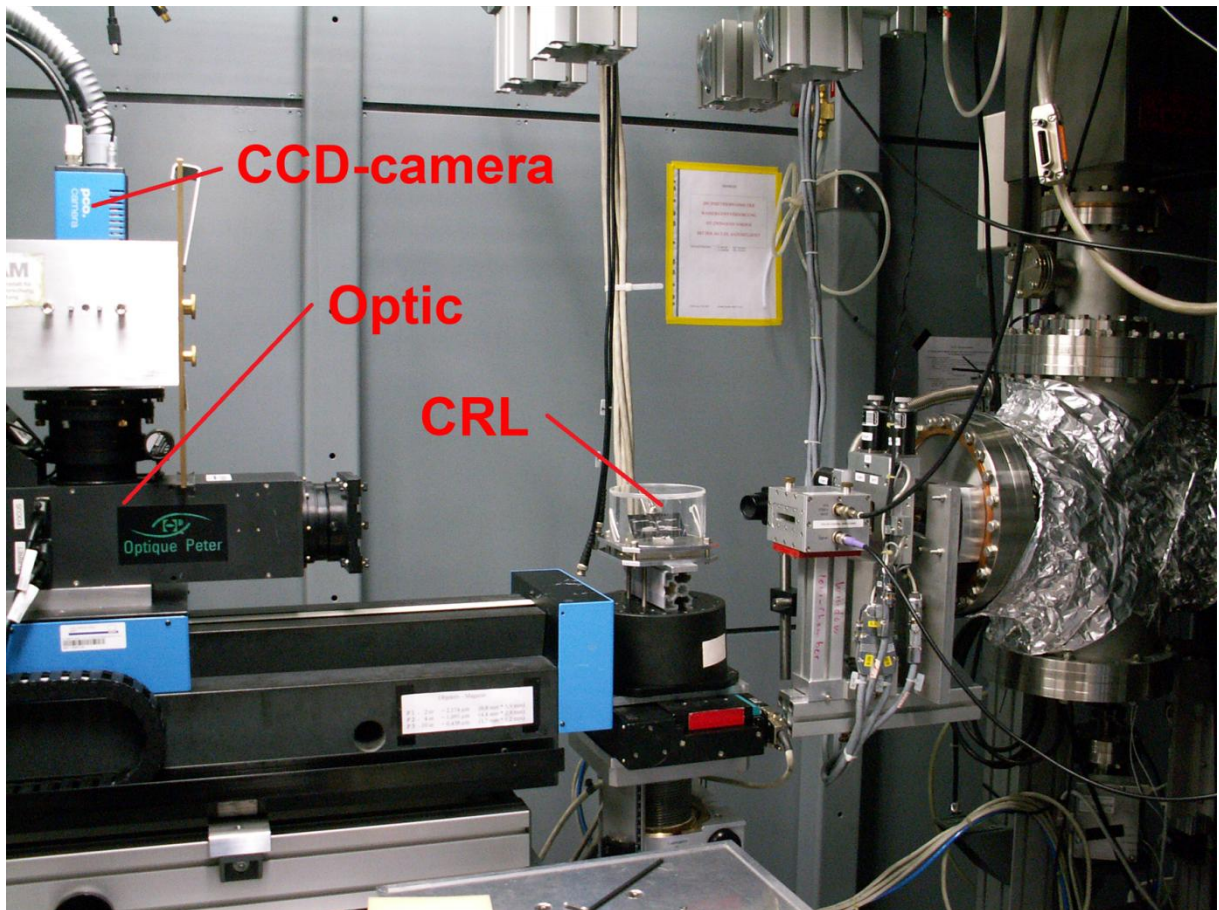


Figure 6.5 Imaging setup with mounted CRL-plate.

To analyze the images a program written in IDL (Interactive Data Language) was used to fit the brightness distribution with a 2 dimensional Gaussian distribution curve. The full width half maximum (FWHM) of the Gaussian distribution in horizontal and vertical direction was then assigned to be the spot size.

The size of the spot in each position was plotted as function of the distance and the distance where the smallest spot size was measured was assigned to be the focal length of the according lens.

6.3.1 Focal length of lens 8t

The lens 8t is the lens for the Cu-K absorption edge with a nominal energy of 9 keV, a nominal focal length of 350 mm and an estimated beam size of $0.5 \mu\text{m}$ times $1.21 \mu\text{m}$.

Since the aim here was to monitor the change in the spot size it was sufficient to just sum up the pixel with a brightness higher than the threshold. The analysis of the pictures resulted in a certain number of pixel for each position which was divided by the smallest value of the according set of values.

The left graph in figure 6.6 shows a scan of lens 8t from position 300 to 400 in steps of 2 mm while the right graph show a narrower range (325 mm to 375 mm) with a higher resolution of 1 mm steps.

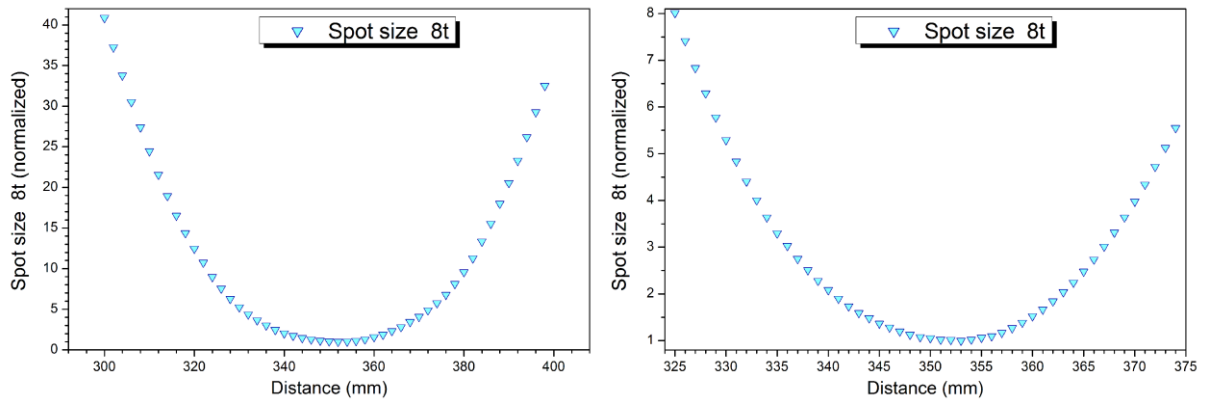


Figure 6.6 Scans of the spot size with 100 and 50 mm range from lens 8t

Figure 6.7 provides a detail of the region around the minimum of the spot size and shows the smallest spot size of this lens at position 353 mm which was defined as the measured focal length.

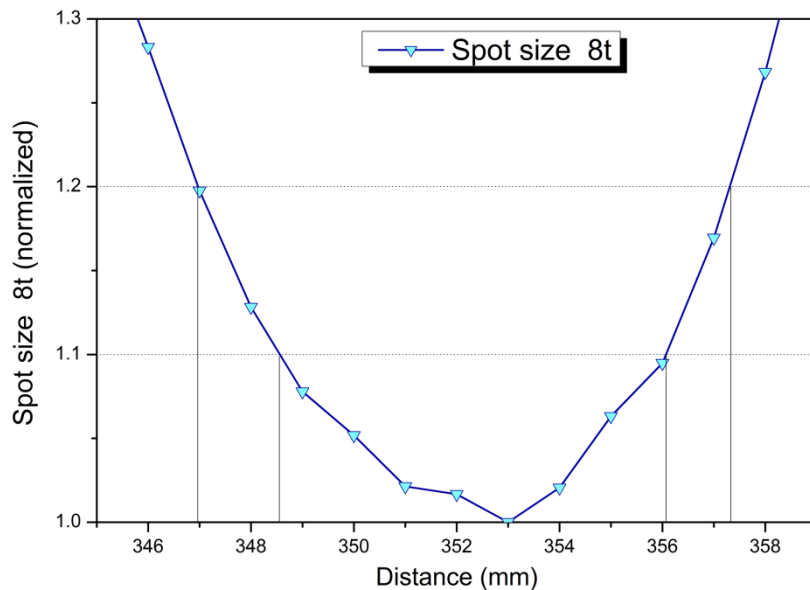


Figure 6.7 Detail of the region around the focal length

If a change of the spot size of 10 % or even 20 % - corresponding to a spot size of $1.32 \mu\text{m} \times 0.55 \mu\text{m}$ or $1.4 \mu\text{m} \times 0.6 \mu\text{m}$, respectively - is seen as not significant the focal length of this lens can be defined as $352.5 \text{ mm} \pm 3.5 \text{ mm}$ or $352 \text{ mm} \pm 5 \text{ mm}$.

6.3.2 Measured focal lengths of lens plate #08-762P-JW13_a

The data for the other lenses on the lens plate were collected in the same way and for the values given in the following paragraph the threshold for the change of the spot size was set to 20%. The signal to noise ratio in the pictures were especially for the lenses for low energies - due to the absorption in air - not very good but sufficient. For the lens 1t with a nominal energy of 5 keV the focal spot could not be defined properly because of a too low signal to noise ratio. Figure 6.8 and figure 6.9 show the spot size as function of the distance for the upper and lower half of the lens plate.

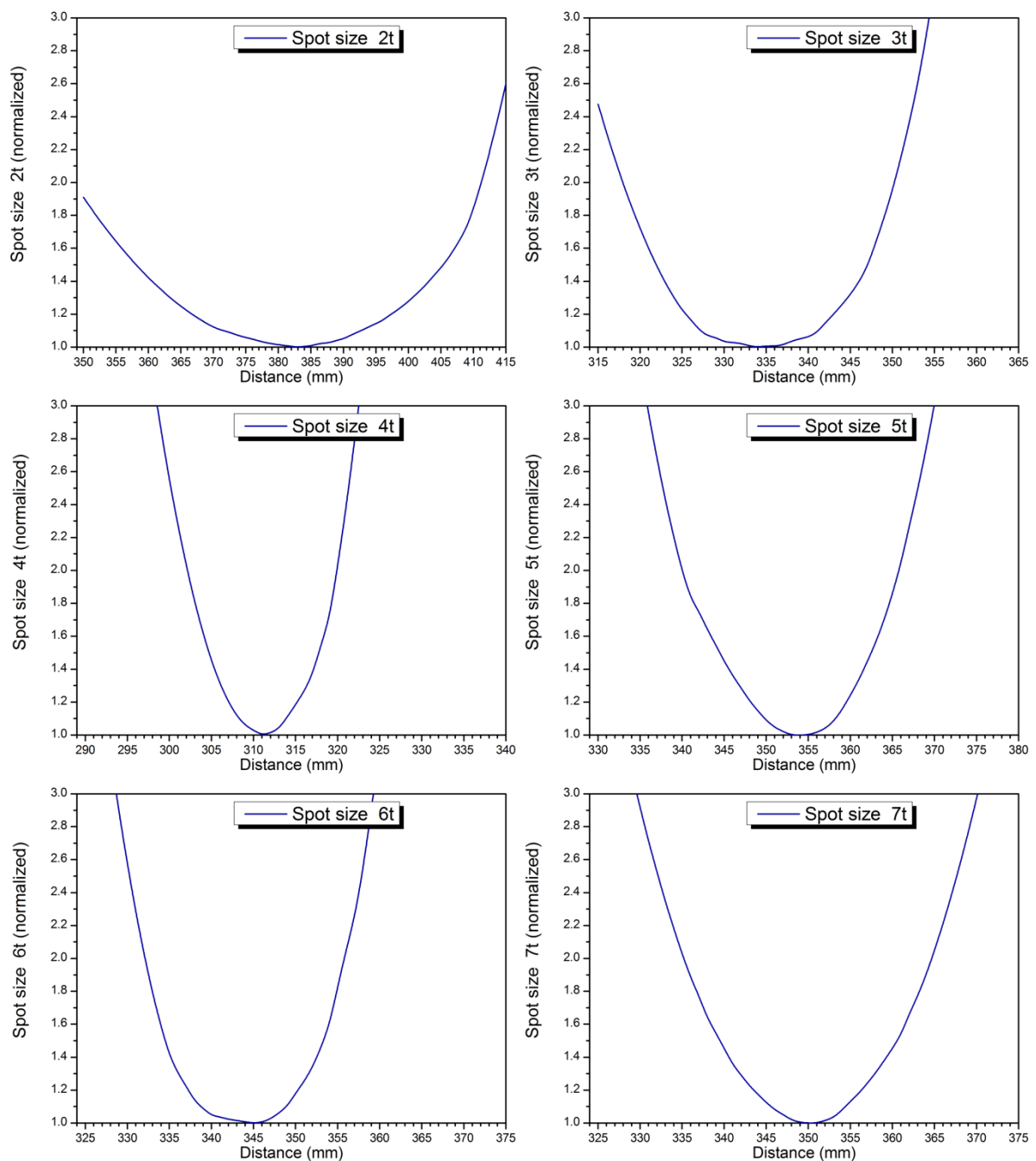


Figure 6.8 Scans to determine the focal distance of the lenses from the upper half of the lens plate

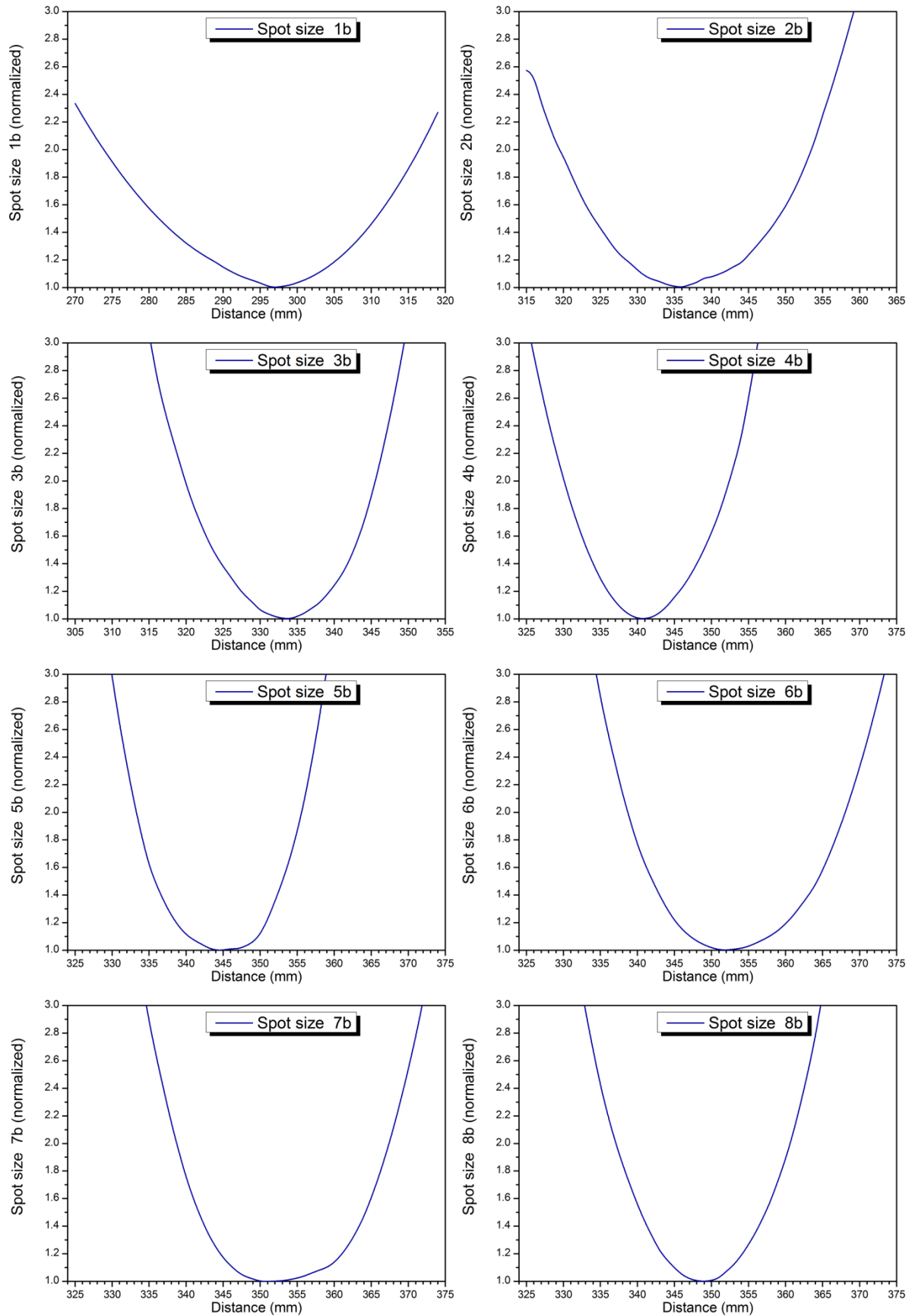


Figure 6.9 Scans to determine the focal distance of the lenses from the lower half of the lens plate

Lens	8t	7t	6t	5t	4t	3t	2t	1t	1b	2b	3b	4b	5b	6b	7b	8b
nominal focal length [mm]	350	349	348	359	318	341	400	220	317	350	350	350	350	350	350	350
measured focal length [mm]	352	350	344	354	311	334	382	X	297	336	333	341	345	352	352	349
range [mm]	± 5	± 6	± 7	± 6	± 5	± 9	± 15	X	± 10	± 9	± 6	± 5	± 6	± 8	± 8	± 6
difference [mm]	-2	-1	4	5	7	7	18	X	20	14	17	9	5	-2	-2	1

Table 6.3 The nominal, the measured focal length and the difference between these values and the range.

In table 6.3 a summary of the measured values for the focal length of the different lenses is shown together with the range for a threshold of 20 % of the spot size. Comparing these values with the nominal values it is to see that for the inner lenses the difference between the values gets quite big, even exceeding the range of the 20 % threshold.

By the date this work was presented the origin of this discrepancy was not known, but the investigation was still ongoing.

6.4 Spot size and spot geometry

As shown above and in chapter 3 the size of the spot depends on various factors. Some of these factors are fixed like the source size and the distance between source and lens which depend on the synchrotron facility and the design of the beamline. Other parameters of the lens, like the aperture sizes, are given by the producer of the lens, while the energy and the focal distance can be chosen by the customer.

For a given lens changes in the spot size and geometry may occur due to differences in the beam characteristics. The results from investigations using different settings at the *BAMline* are shown below.

6.4.1 Influence of the DMM on the spot size

The originally calculated flux densities for the beamline were confirmed by measurements with a calibrated ionization chamber provided by the Physikalisch-Technische Bundesanstalt (PTB - the national metrology institute of Germany). The flux on the sample after the DMM and DCM respectively, was calculated for different apertures and the CRL. Table 6.4 shows as an example the lens 8t which has a nominal intensity gain of 13900 leading to a flux of 5.84×10^8 (4.2×10^6 for the DCM) photons per second in the spot of the lens.

Aperture [μm]	Flux DMM [ph/s]	Flux DCM [ph/s]
1000 \times 1000	$7.0 \cdot 10^{10}$	$5.0 \cdot 10^8$
360 \times 360	$9.0 \cdot 10^9$	$6.5 \cdot 10^7$
1.2 \times 0.5	$4.2 \cdot 10^4$	$3.0 \cdot 10^2$
CRL (1.2 \times 0.5)	$5.84 \cdot 10^8$	$4.17 \cdot 10^6$

Table 6.4 Calculated flux densities after different apertures and the CRL 8t.

As already mentioned before this about 100 times higher flux of the DMM may be preferred for some applications and therefore the influence of this monochromator was studied.

The graphs in figure 6.10 show the size of the focused beam as a function of the distance between the CRL plate and the sample. Though the nominal spot size, specified by the manufacturer, is $1.21 \mu\text{m} \times 0.5 \mu\text{m}$ - which would give (5.5 and 2.25) \sim 12.4 pixel - the solid line in the figure shows that the spot size with the DMM is about 25 pixel at a focal distance of about 352.5 mm (compare table 6.3). The reason for the increased spot size is the broad energy bandwidth of $\frac{\Delta E}{E} \approx 1.6 \%$ (Gaussian distribution with 144 eV FWHM at 9 keV) of

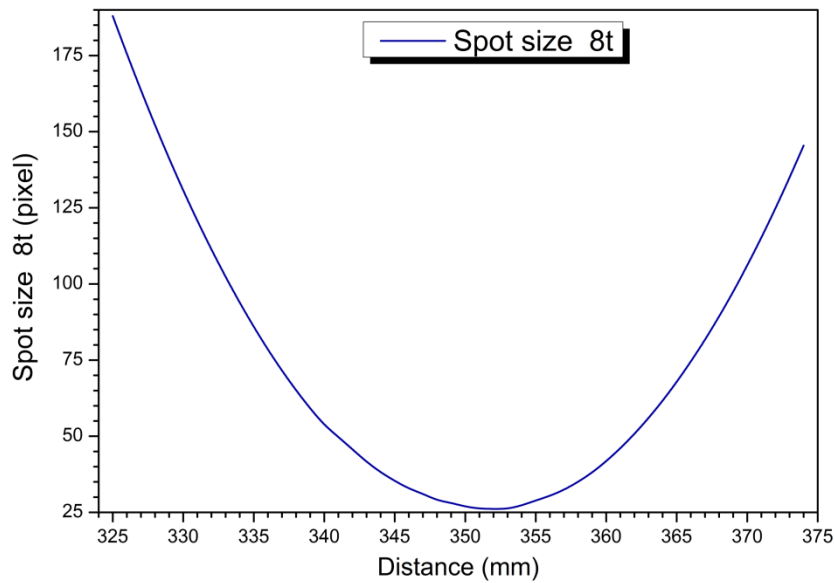


Figure 6.10 Spot size after the DMM in pixel as function of the distance

the DMM photons compared with the DCM with a bandwidth of only $\frac{\Delta E}{E} \approx 0.02\%$ (1.8 eV FWHM). This means that the DMM transmits a significant amount of photons with lower and higher energies than the nominal. Since photons with lower energies have a shorter and with higher energies have a longer focal distance they produce a bigger spot at the nominal distance.

6.4.2 Changes of the spot geometry due to pre-focusing

A big advantage of the DMM is that the second mirror is mounted on a meridional bending mechanism which allows varying the radius of the multilayer in order to achieve a focused or collimated beam. By bending the DMM to provide a parallel beam the impinging photon flux is increased by a factor of 2 - measured with the ionization chamber - to about 1.8×10^{10} photons s^{-1} through the lens aperture and 1.16×10^9 photons s^{-1} in the spot. The blue lines in figure 6.11 show the spot size of the CRL when using the DMM and the red lines after parallelizing the beam by bending the second multilayer. When looking to the solid lines for the horizontal axis it is to see that the spot size increases only from about $1.5 \mu m$ to $1.6 \mu m$, while the enlargement in the vertical axis - the dashed lines - from about $0.8 \mu m$ to $1.45 \mu m$ is significant. This behavior was predictable since the bending of the DMM only parallelizes the beam in the vertical direction. Two magnified details of recorded pictures, one with and the other without bended multilayer, are shown on the right side of figure 6.11.

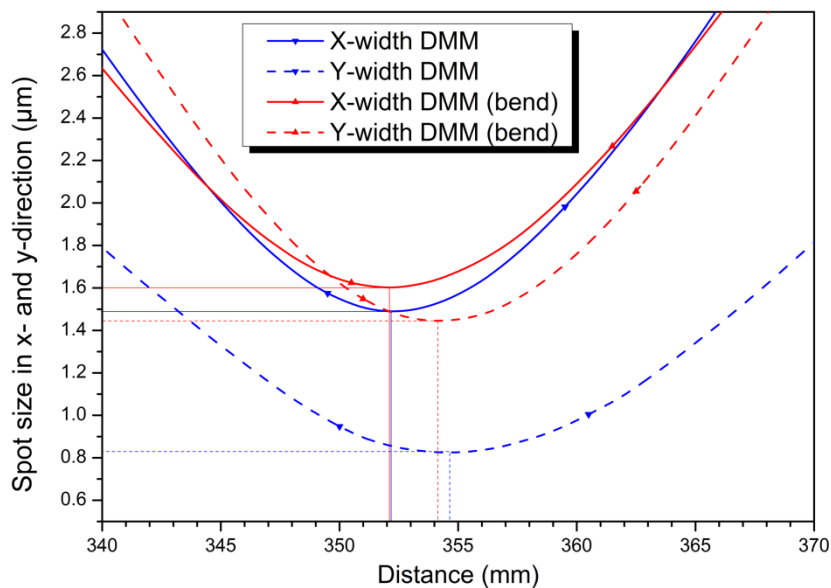


Figure 6.11 Influence of the DMM bender on the spot in x- and y-direction

6.4.3 Spot size depending on the energy

Figure 6.12 shows the spot size as a function of the distance for four different energies which were chosen to cover the interval used for XANES measurement.

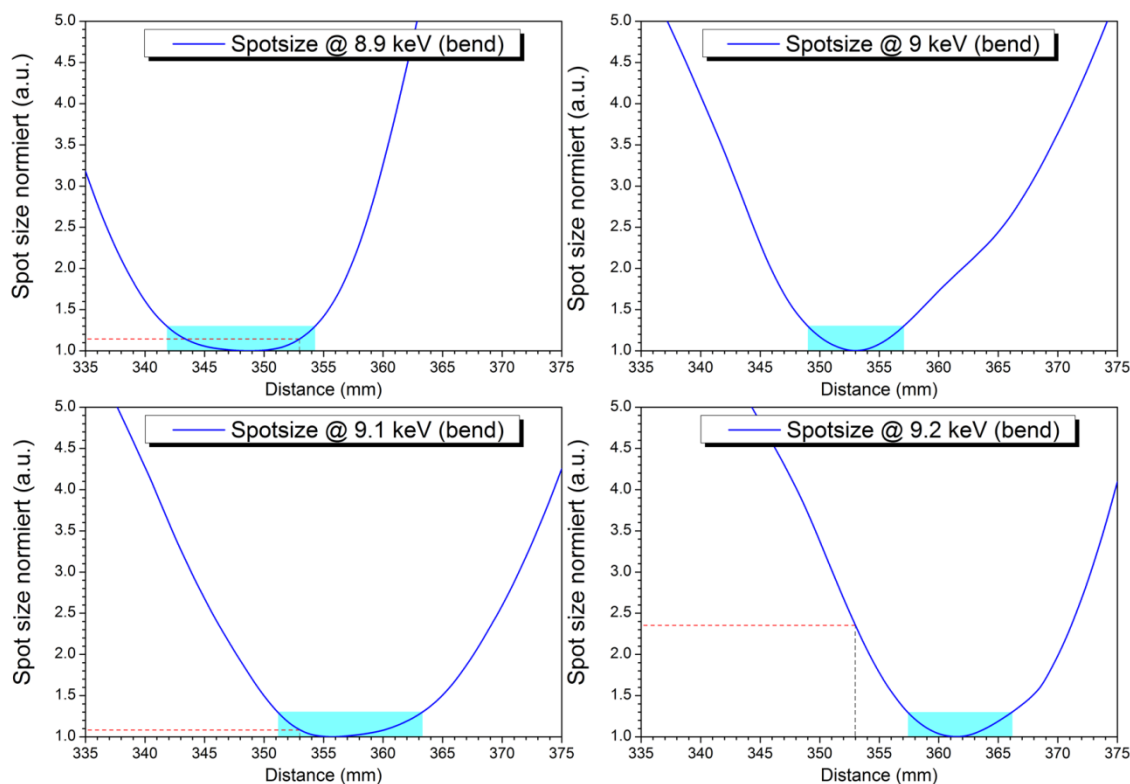


Figure 6.12 Influence of different energies from a narrow range on the spot size

The spectra are normalized to the measured spot size of $1.3 \mu\text{m} \times 0.6 \mu\text{m}$ for the DCM. It is obvious that within this energy region the best achievable spot size keeps the same, only the

focal distance changes from -4 mm at 8.9 keV to +3 mm and +8 mm for 9.1 keV and 9.2 keV respectively. If the distance between sample and lens is adjusted accordingly the spot size is constant within the energy range needed for XANES measurements. Defining ranges in which the spot size does not change significantly leads to a range of ± 4 mm for 9.0 keV around a focal distance of 352 mm or ± 4 mm at 361 mm for 9.2 keV as indicated in figure 6.12 by the cyan rectangles. With the gray dotted lines marking the focal distance of 352 mm the red dotted lines mark the corresponding spot sizes at the different energies. These markers show that for energies between 8.9 keV and 9.1 keV the spot size changes less than 15 % ($\sim 1.5 \mu\text{m} \times 0.7 \mu\text{m}$).

A more detailed measurement for the near edge energy region between 8.95 keV and 9.25 keV at a fixed distance of 352 mm between the lens and the scintillator is shown in figure 6.13.

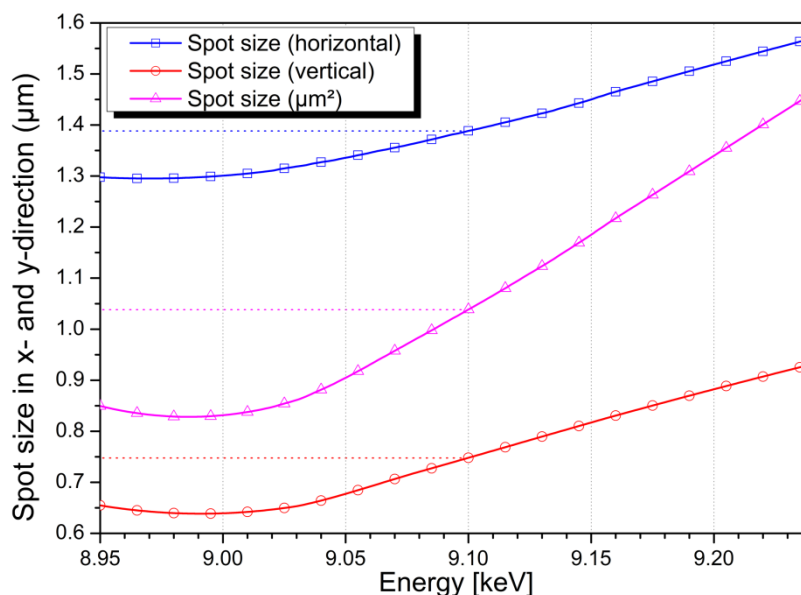


Figure 6.13 Spot size at the focal distance of 352 mm as a function of the energy.

This particular lens (8t) has a nominal energy of 9 keV which was chosen to perform XANES measurements at the Cu-edge. The XANES region for Cu compounds usually ends before 9.1 keV where the spot size of the lens is $1.4 \mu\text{m} \times 0.75 \mu\text{m}$. For many applications this increase of the spot size can be seen as not significant since the samples are homogeneous over an area of at least this size.

This result is one of the most important from the present work, namely that XANES measurements can be performed without adjusting the distance between sample and lens [106].

6.4.4 Spot size for energies much higher than the nominal

Figure 6.14 shows the spot size of the CRL with a nominal energy of 9 keV as function of the distance when using a monochromatic beam with 9 keV, 11 keV and 13 keV, respectively.

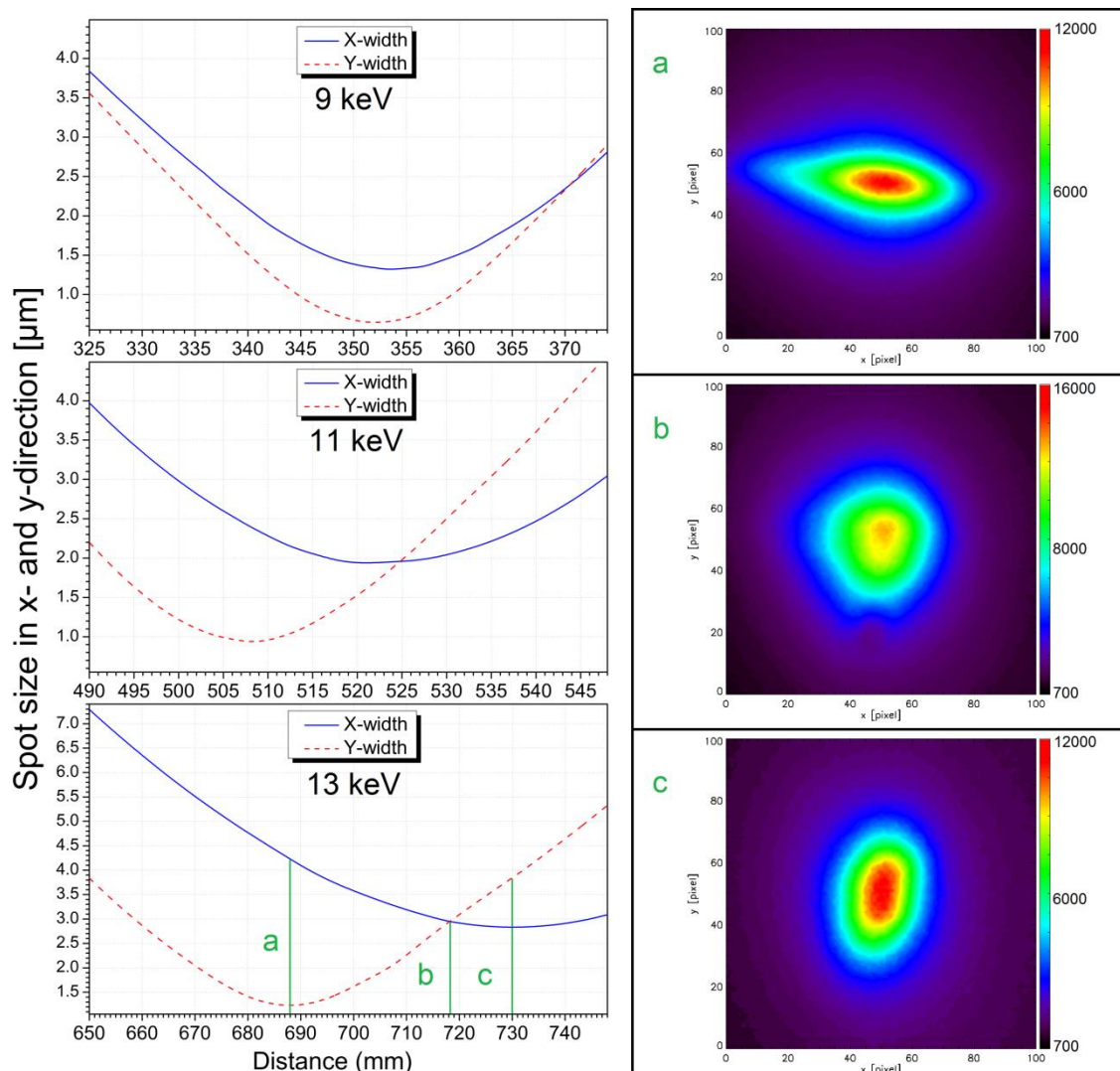


Figure 6.14 Spot size of the compound refractive lens (8t) at high energies

The spot size at 9 keV is, as already mentioned above, $1.3 \mu\text{m} \times 0.6 \mu\text{m}$ at a focal distance of 352 mm. There is a slight shift of about 2 mm noticeable between the vertical and the horizontal focus but this does not have any effect on the spot size.

Using the same lens to focus photons with 11 keV the spot size increases to $1.9 \mu\text{m}$ in horizontal and $0.9 \mu\text{m}$ in vertical direction, unfortunately at different distances of 520 mm and 509 mm respectively. Here the shift is about 11 mm and already affects the spot size. The smallest spot with respect to the area is at 509 mm with $2.3 \mu\text{m} \times 0.9 \mu\text{m}$ ($\sim 2.0 \mu\text{m}^2$) while at 520 mm distance the spot is about $1.9 \mu\text{m} \times 1.5 \mu\text{m}$ ($\sim 2.8 \mu\text{m}^2$).

When the energy is increased to 13 keV the lens can produce a spot with a size of 2.8 μm in width and 1.2 μm in height at distances of 730 mm and 688 mm. This 42 mm shift influences the spot size significantly, as e.g. at the position of the vertical foci (688 mm) the horizontal spot size is 4.2 μm while at 730 mm (horizontal foci) the height of the spot is 3.9 μm . On the right hand side of figure 6.14 details are shown from the spot at 688 mm (a), 718 mm (b) and 730 mm (c) distance from the lens. The gray value of the original pictures are for better illustration converted into color while the values of the color bar on the right show the original gray values.

6.5 Influence of the CRL on the features of XAFS spectra

As shown in chapter 6.4.3 the spot size after the CRL does not change significantly within the energy range for Cu-XANES measurements, but there are also other parameters which may influence the measurement as for example changes in the absorption. To study whether the CRL influences or not the shape of the XAFS spectra several different Cu compounds were chosen to analyze. The standards were prepared by simply applying a thin film of powder on scotch tape and cover it with another stripe of the tape to assure that the sample kept in position during the measurement.

The standards could have been measured in absorption mode, but since most of the samples which should be analyzed at this beamline are too thick to be measured in absorption mode the XAFS measurements on the standards were also conducted in fluorescence mode. Figure 6.15 shows a comparison of the XAFS spectra - recorded with and without the CRL - of the six standards:

- | | | |
|----|--|---|
| a) | Cu (metal): | Copper metallic - foil with a thickness of 0.45 μm |
| b) | $\text{Cu}(\text{Cys})_4$: | Copper-cysteine complex |
| c) | $\text{CuSO}_4(5\text{H}_2\text{O})$: | Copper sulfate pentahydrate (Chalcanthite) |
| d) | CuCO_3 : | Copper carbonate |
| e) | $\text{K}_2\text{Cu}(\text{OX})_2$: | Dipotassium bisoxalato copper |
| f) | CuO : | Copper oxide |

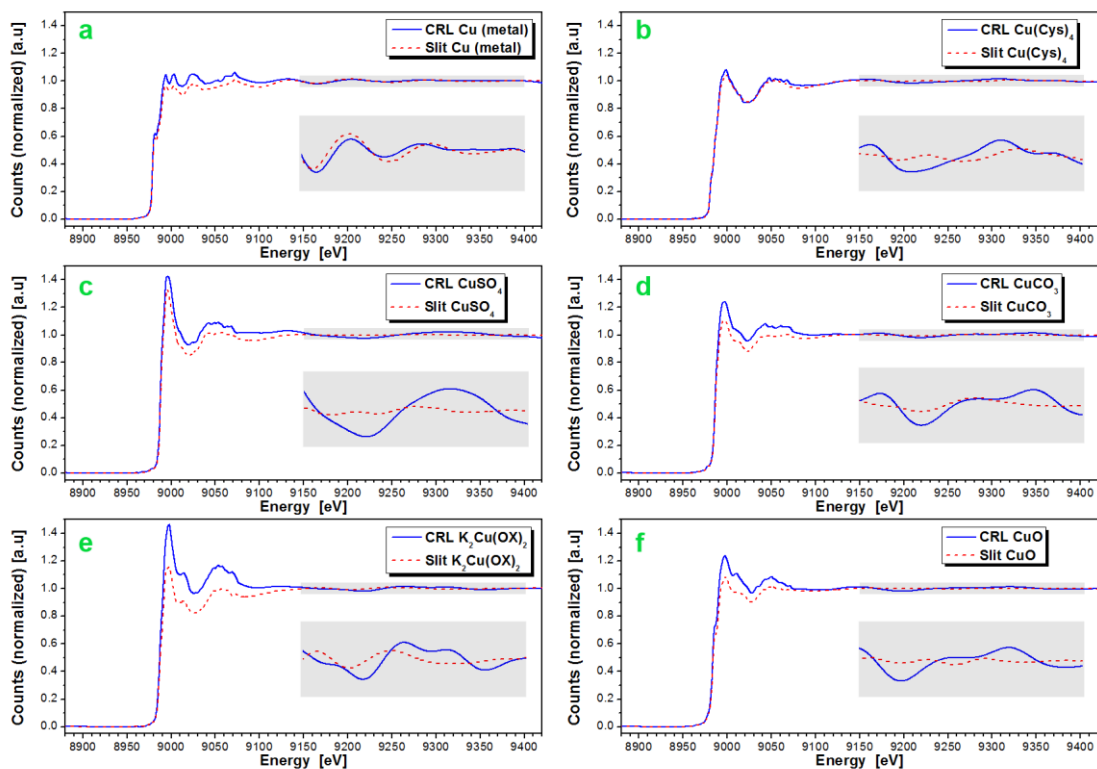


Figure 6.15 Normalized spectra of six different Cu-standards measured with and without lens. The insets (highlighted in gray) show an enlargement of the EXAFS region.

The solid lines represent the spectra collected with the lens and the dashed lines the ones recorded with a slit aperture. In order to have equal excitation conditions the size of the slit aperture was chosen to be the same as for the lens, which was about $360 \mu\text{m} \times 360 \mu\text{m}$.

Using the software ATHENA [107], included in the package IFEFFIT the spectra shown in figure 6.15 were normalized using a pre-edge and post-edge line. In the XANES region from about 8.9 keV up to 9.1 keV a good correlation of the spectral features is observed, although the graphs from the measurement with the CRL show an overestimation of the count rate. The oscillations in the EXAFS range on the other hand do not coincide that well, as shown in the gray highlighted insets in figure 6.15.

A general problem with the sample preparation for high resolution analysis is that inhomogeneities on a sub-micrometer scale already influence the measurement. Since the used standards were prepared from powders a sub- μm homogeneity was almost certainly not given. This in combination with tiny instabilities of the beam position on the sample and/or the changes in the spot size lead to fluctuations in the quantity of the illuminated sample and most probably caused this behavior. In the XANES region, due to the small changes of the spot size and the higher amplitudes of the oscillations, these effects are not visible, but due to the lower amplitudes and the bigger changes of the beam size in the EXAFS region they get evident. The fact that the best match in the EXAFS range is found for the rolled Cu-foil (sample (a)) - which is the most homogeneous of the samples - hardens this theory. Further investigations with much more accurate prepared samples should give a better understanding of these phenomena. At the time the work was presented this investigation was still ongoing, while the main focus of this work was on other influences.

Figure 6.16 shows the comparison of the two XANES spectra recorded with a slit aperture and the CRL, on a dipotassium bisoxalato copper(II) tetrahydrate ($\text{K}_2\text{Cu}(\text{OX})_2$) sample. In figure 6.16a the spectra, normalized using a pre-edge and post-edge line, show an overestimation of the count rate in the XANES region for the measurement with the CRL. Since this behavior could not be explained, the spectra were displayed normalized to match the count rates in the near edge region (see figure 6.16b). This “normalization” shows up to about 9075 eV a very good correlation between the two graphs, from 9075 eV to higher energies the CRL overestimates the count rate compared to the one with the aperture. This behavior however can be easily explained as an influence of the lens, since the absorption decreases with higher photon energies which is why the photon flux increases and so does the fluorescence signal. Anyway, this effect of the CRL can be compensated, as shown in figure 6.16c, by calculating

the change in the absorption and correct the measured signal. Another possibility is to measure the photon flux between the lens and the sample, e.g. with an ionization chamber, and use this signal for the correction of the spectra.

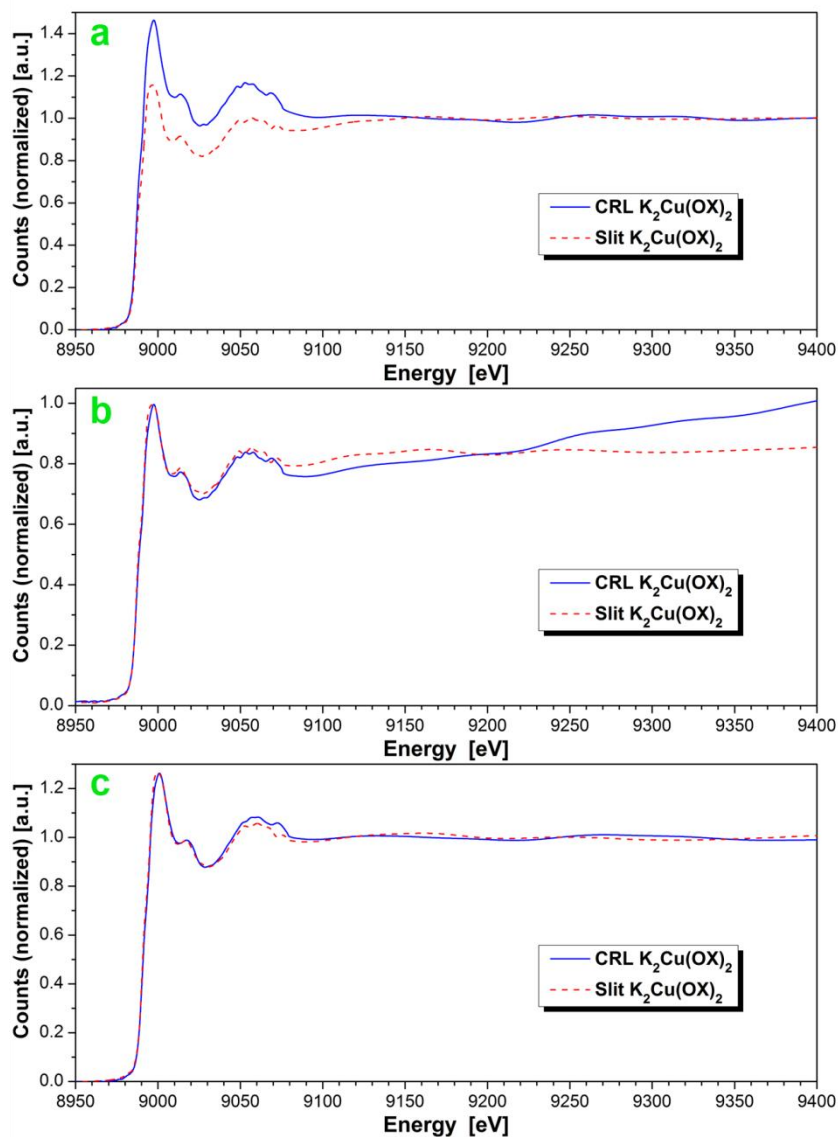


Figure 6.16 Comparison of XANES spectra from $K_2Cu(OX)_2$ with CRL and Slit.

In figure 6.17 the six different Cu samples are shown again. The spectra are normalized to 1 and additionally the spectra obtained with the CRL are corrected regarding the changes of absorption within the lens. Anyway, for all cases, even the ones without correction, a good agreement of the features in the XANES region can be observed (see figures 6.15 and 6.16a).

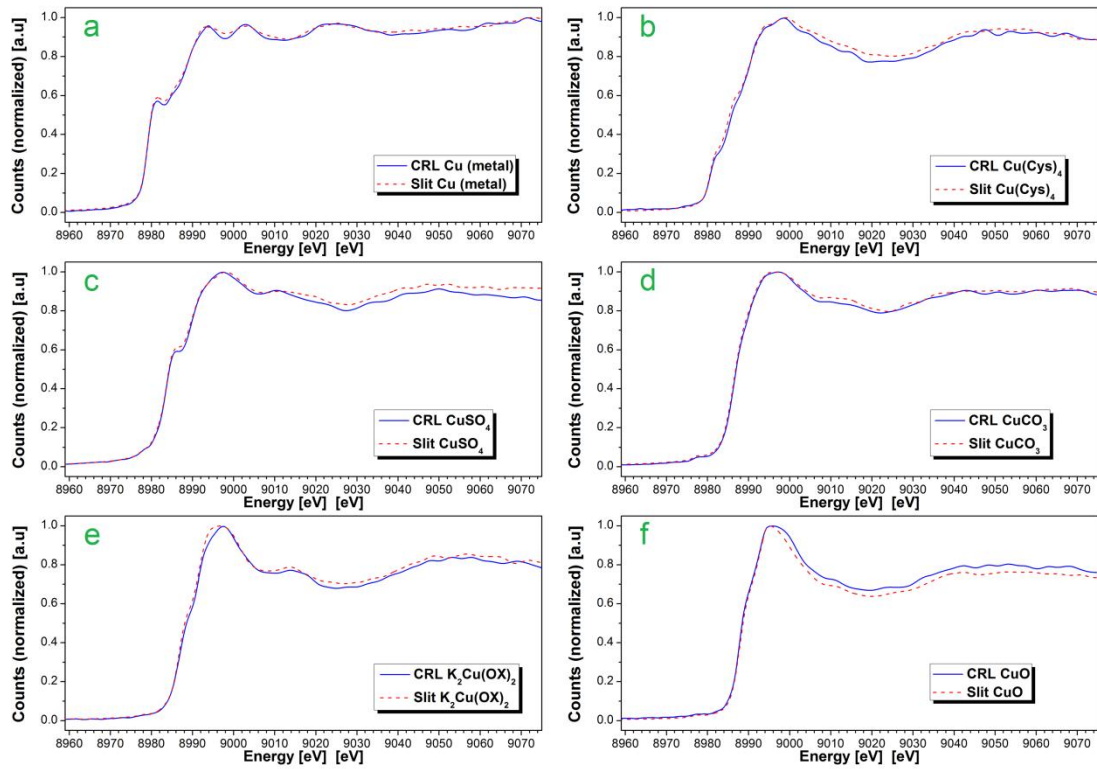


Figure 6.17 Comparison of the XANES spectra normalized to 1 and absorption corrected for the CRL.

6.6 Conclusions and outlook

In chapter 6.4.3 it was shown that for the near edge energy region the spot size does not change significantly and the results presented in chapter 6.5 showed that it is possible to conduct these measurements without taking into account the change in the absorption of the lens. Therefore it can be concluded that, on samples only slightly bigger than the spot size of the lens, XANES measurements can be performed with compound refractive lenses without the necessity to adjust the distance between sample and lens or consider the absorption of the lens material.

For samples smaller than the spot size XANES analyses should also be possible, but for this purpose reference materials with appropriate well known sizes smaller than 1 μm have to be produced and measured. With the data of these measurements a correction of the spectra from unknown samples can be made.

For the higher energies, needed for EXAFS scans, the distance between sample and CRL has to be adjusted simultaneously to the tuning of the energy and the absorption of the lens has to be taken into account. While the absorption correction is a solvable problem, the correction of the distance is a technical challenge. To correct the distance either the lens or the sample and the detector has to be moved along the beam. Having a beam with a Gaussian distribution and a particle size in the range of the beam size already little differences in the position how the beam hits the sample can change the signal significantly. These changes influence the results of the measurement since they can be easily bigger than the changes in the EXAFS signal which are often very small. This means that only tiny imperfections in the mechanical parts or in the alignment of the whole system can be tolerated. Solving this problem is difficult but once it is overcome EXAFS measurements with compound refractive lenses are possible. The size of the sample thereby has to be at least two times the spot size.

7 Applications

This chapter gives an overview of applications of the compound refractive lens at the *BAMline*. A big part of the applications during the last years was the investigation of polycrystalline solar cells [108], but also samples from scientific fields like geology, biology, cultural heritage and others were examined. Most of this work is still ongoing and not published yet except of the investigation of Portuguese glazed ceramics from the XVIth to XVIIIth centuries by Guilherme et al. [109].

Increasing requirements for accurate measurements of trace elements in many areas of daily life, for example, the analysis of toxic elements in food and environmental samples [110] or in industrial applications such as semiconductor-grade silicon [111, 112], has stimulated a rapid improvement in highly sensitive analytical methods. It has been shown that the LOD values are in the order of a picogram per gram ($\text{pg}\cdot\text{g}^{-1}$) for neutron activation analysis (NAA), synchrotron radiation-induced total reflection X-ray fluorescence (SR-TXRF) and mass spectrometry (MS) - in particular, for inductively-coupled plasma mass-spectrometry (ICP-MS).

Mass spectrometry techniques are destructive since the samples have to be dissolved. On the other hand, separation and removal of matrix elements make LOD values below $\text{pg}\cdot\text{g}^{-1}$ available. In contrast, conventional XRF is a non-destructive technique for trace element analysis with an LOD in the order of $\mu\text{g}\cdot\text{g}^{-1}$. Despite this drawback of a six orders of magnitude larger LOD, XRF is widely used because it is non-destructive and requires no sample preparation.

The analysis of inhomogeneous samples is always problematical especially if the applied analytical method does not allow processing of large specimen sizes. Inhomogeneous samples are typically homogenized by dissolving them in an acid or by milling them to a fine powder. In cases of very large samples, where only selected parts of a specimen can be homogenized, the selection of the specimen for analysis can dramatically influence the results. On the other hand, cases in which only small amounts of sample are available also exist. For example, one can only remove tiny pieces from hidden parts of an object when analyzing art objects, which can result in non-representative results and misinterpretations.

Analysis with high spatial resolution is often essential for the understanding of material properties and in monitoring biological, chemical and physical processes [73-75]. In the last several decades, great improvements have been achieved in focusing X-rays for this purpose.

Today X-ray beams are available with sizes in the order of several micrometers for laboratory sources and down to nanometers for synchrotrons [5, 35, 72]. As a result of these developments, XRF has gained increasing importance for analyzing samples on a micrometer and sub-micrometer level in material and art research [113-115], in geology and environmental science [116-118], in biology and medicine [119-121] or in forensics [122]. High-resolution line scans on the cross sections of layered samples with a micro focus can provide information about production of and diffusion processes in ceramics [114]. Furthermore, two- and three-dimensional mapping is used to better understand, e.g., the role of trace elements in cancer biology [121] and osteoarthritis [123]. In addition to the fact that the knowledge of the localization of trace elements in the sample is important, the use of micro-sized beams has the advantage of an increased sensitivity, which results from a smaller irradiated volume with a higher flux density when using focusing X-ray optics.

7.1 Polycrystalline solar cells ^[108]

When a photon hits a solar cell it can be absorbed by the silicon, when its energy is higher than the energy difference between the silicon bands. The energy of the absorbed photon is then transferred to an electron which is excited into the conduction band where it is free to move within the semiconductor. The removed electron leaves a "hole" in the valence band which allows a bonded electron of a neighboring atom to move there while leaving behind another hole and so on. The basic structure of a Si based solar cell and its working principle is shown in figure 7.1.

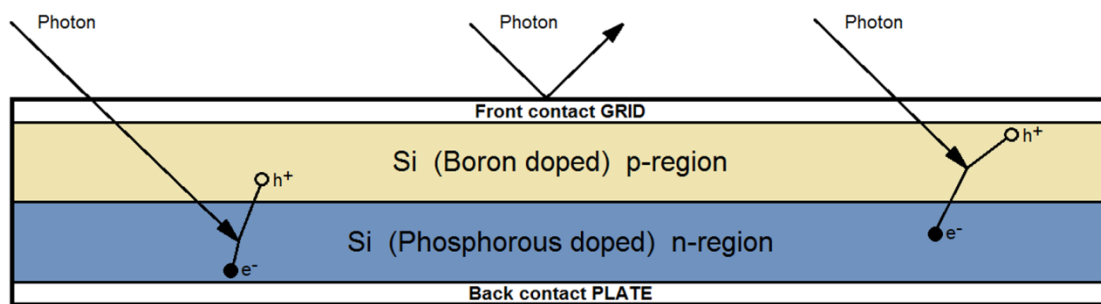


Figure 7.1 Basic structure of a silicon based solar cell and its working mechanism

An upper theoretical limit for the efficiency of silicon based p-n junction solar cells has been calculated by Shockley and Queisser in 1961 [124]. They calculated the so called detailed balance limit of efficiency for the ideal case to be about 30 % for an energy gap of 1.1 eV. These assumptions were that the sun and the cell are blackbodies with temperatures of 6000 K and 300 K respectively and the only electron-hole pair recombination mechanism is radiative. One reason for the low efficiency value is that for the calculations the whole solar spectra (blackbody) is used where a part has too low energies to create electron-hole pairs, while on the other hand the probability for the interaction of photons with electrons becomes smaller the higher the energies are. Nowadays the value for the Shockley-Queisser limit is 33.7 % for a single p-n junction with a band gap of 1.1 eV. The IEC (International Electrotechnical Commission [125]) standard 61215 is used to compare the performance (power and efficiency) of solar cells, using terrestrial standard temperature and conditions (STC): irradiance of 1 kW/m^2 , a spectral distribution close to solar radiation through AM (airmass) of 1.5 with a cell temperature of $25 \text{ }^\circ\text{C}$. The resistive load is varied from short circuit ($R = 0 \ \Omega$) until the maximum of the power output called Watt-peak (W_p) is achieved.

It is common knowledge that recombination of electron-hole pairs takes place on crystal impurities which dramatically lowers the efficiency of solar cells, and therefore silicon of

high purity is required. However, for financial reasons, solar cell manufacturers must use "dirty" silicon, so-called solar-grade silicon (SoG-Si), for the production of polycrystalline solar cells. It contains impurities with concentrations in the order of 10 to 100 ng·g⁻¹. In contrast, the much more expensive semiconductor-grade silicon displays total contamination levels of one ng·g⁻¹ and below.

More specifically, tolerable impurities of copper are approximately 10¹⁵ atoms per cm³. To achieve an acceptable energy efficiency level in polycrystalline solar cells, only 2×10^{12} iron atoms per cm³ (0.4 ng·g⁻¹) are permissible [126]. However, the iron content in multicrystalline silicon, where typical concentrations of 10¹⁵ to 10¹⁶ iron atoms per cm³ are found depending on the feedstock and purification method - is much higher than this threshold. Obviously, these high levels of impurities must result in very low solar cell efficiencies if the iron is homogeneously distributed throughout the entire wafer volume. Fortunately, most metal impurities are located at grain boundaries of silicon crystals or cluster within crystals. This means that the impurities in the wafer are locally concentrated. The resulting inhomogeneity of impurity distribution has the advantage that a sufficient charge carrier lifetime may remain in the silicon allowing a solar cell efficiency of about 20%. Thus, it is obvious that the knowledge of the spatial distribution of relevant impurities is even more important than their total quantity for understanding and optimizing solar cell efficiency. Due to its good sensitivity and high resolution, synchrotron based μ -XRF was often chosen to study the metal impurity distribution in polycrystalline solar cells.

In the scope of a long-term project, the objective in the present study was to localize these contaminations within solar cells using high resolution μ -XRF. In performing such measurements on multicrystalline silicon wafers (mc-Si), the spatial (3-dimensional) and not only a 2-dimensional distribution of impurities, as already investigated and reported by several other groups [127-131], should have been determined.

7.1.1 Theoretical considerations

A typical texture of a multicrystalline silicon wafer in which impurities, for example, iron, nickel, copper and other elements accumulate in precipitates is shown schematically in figure 7.2. A standard XRF setup, in which the incident X-ray beam illuminates a large volume of the microcrystalline silicon wafer, is illustrated in the upper part (A) of figure 7.2, where the particle occupies only a small fraction of the illuminated volume. The XRF conditions when using focusing optics is shown in the lower part (B) of figure 7.2. In this case only a

small total volume is illuminated, and the relative volume occupied by the metallic particle is much larger. It is obvious that the relative fluorescence signal intensity from an included particle is much higher in scenario B than in A.

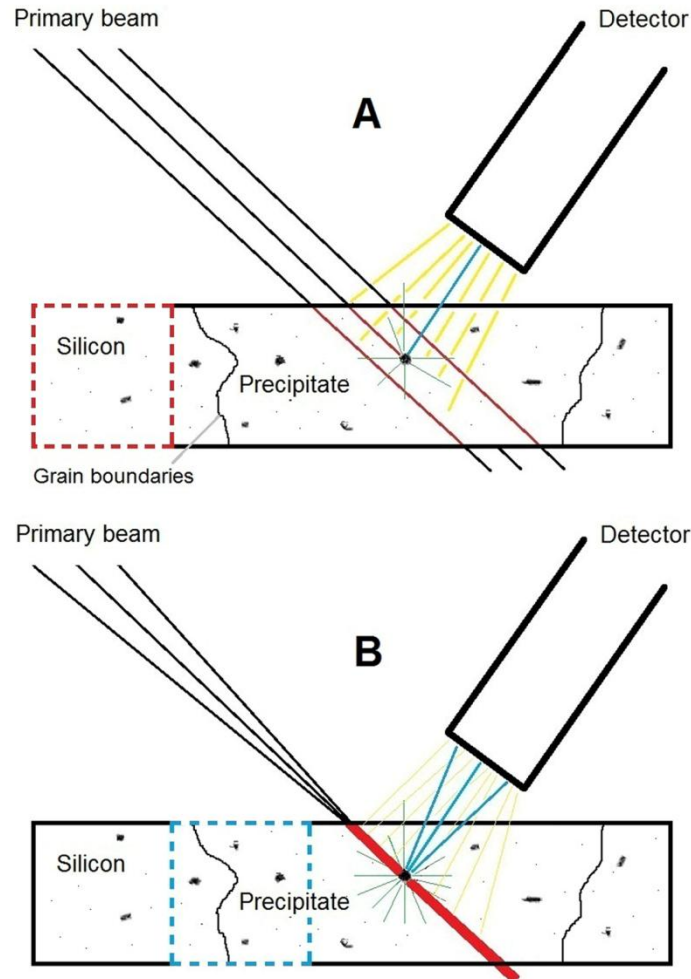


Figure 7.2 Schemes of the analysis conditions of a silicon wafer with standard XRF and μ -XRF (A and B, respectively). The specimen is illuminated without (A) and with (B) a focused beam. Grain boundaries and precipitates of impurities are shown in black. Fluorescence light from the impurity is depicted as blue and fluorescence from the matrix elements as yellow lines. The dotted red box in the upper and the dotted blue box in the lower scheme indicate regions with the same volume but impurities of different quantities and sizes.

Based on the work of other groups like Buonassisi et al. [130] or Macdonald et al. [131], showing that the size of the precipitates is within a range of several nanometers up to tens of micrometers, the precipitate size for Cu was assumed to be about $1 \mu\text{m}^3$. With 10^{15} copper atoms per cm^3 in a multicrystalline silicon wafer ($\sim 45 \text{ ng}\cdot\text{g}^{-1}$) this would give 10^4 precipitates in a volume of $10^{12} \mu\text{m}^3$ and only one per 1 mm^2 area in a wafer with a thickness of $100 \mu\text{m}$. Table 7.1 shows the calculated concentrations for $1 \mu\text{m}^3$ copper in a $100 \mu\text{m}$ thick silicon wafer when irradiated with different aperture sizes.

Table 7.1. Apparent copper concentrations in a silicon wafer when using different XRF beam size apertures corresponding to defined illuminated sample volumes. The copper is assumed to be present as a precipitate with a volume of $1 \mu\text{m}^3$ located in a silicon wafer with a thickness of $100 \mu\text{m}$.

Beam size	Illuminated volume	Cu [$\mu\text{g/g}$]
$(3.162 \times 3.162) \text{ mm}^2$	1 mm^3	0.0038
$(1 \times 1) \text{ mm}^2$	0.1 mm^3	0.038
$(400 \times 400) \mu\text{m}^2$ (CRL)	0.016 mm^3	0.24
$(100 \times 100) \mu\text{m}^2$	0.001 mm^3	3.8
$(50 \times 50) \mu\text{m}^2$	$250000 \mu\text{m}^3$	15
$(30 \times 30) \mu\text{m}^2$	$90000 \mu\text{m}^3$	43
CRL $(1 \times 1) \mu\text{m}^2$	$100 \mu\text{m}^3$	37366

Given the detection limits of an XRF spectrometer, which are on the order of $\mu\text{g}\cdot\text{g}^{-1}$, it is to see that the spot size has to be approximately $100 \mu\text{m} \times 100 \mu\text{m}$ or smaller to detect the Cu precipitate. In figure 7.3 the relative concentration of different Cu precipitates in a $100 \mu\text{m}$ thick wafer is plotted against the spot size.

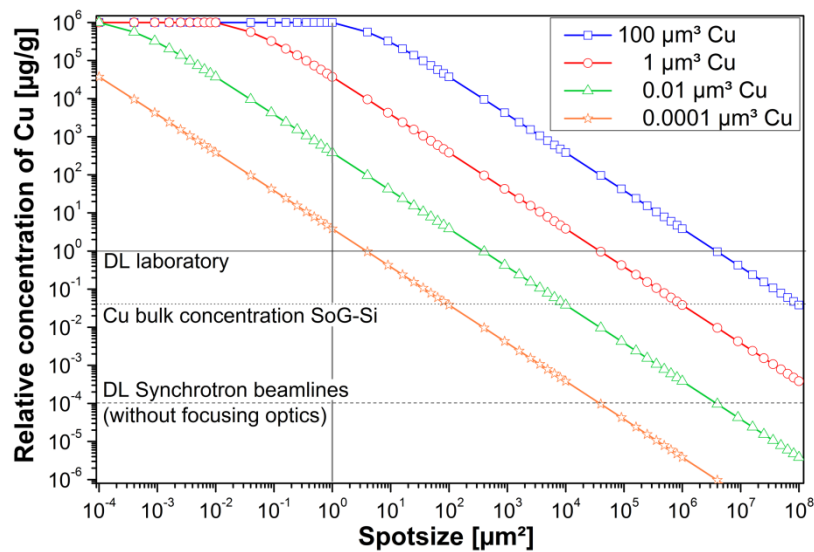


Figure 7.3 Relative concentrations for different copper impurities as a function of the spot size of the X-ray beam on a $100 \mu\text{m}$ thick wafer (weight-averaged copper per weight of silicon).

The copper is assumed to be present in form of discrete particles or crystals with volumes of $100 \mu\text{m}^3$ (blue), $1 \mu\text{m}^3$ (red), $10^{-2} \mu\text{m}^3$ (green) and $10^{-4} \mu\text{m}^3$ (orange), respectively. The vertical line indicates the spot size of the CRL; the horizontal line (solid), the detection limit of XRF for laboratory sources; the dashed line, the detection limit (DL) for Synchrotron radiation X-ray fluorescence analysis (SRXRF) (e.g. at the *BAMline*) without focusing optics; and the dotted line, the bulk concentration of solar grade silicon.

The LOD (Limit Of Detection) for XRF methods using laboratory sources is on the order of 1 to $100 \mu\text{g}\cdot\text{g}^{-1}$, whereas at synchrotron beamlines the limit is much lower due to the higher

flux density, which depends on the synchrotron source, for example, on the order of $\text{ng}\cdot\text{g}^{-1}$. For laboratory sources focusing optics are available with a beam size on the order of $10\ \mu\text{m}$; this means that the minimum detectable size of a copper particle would be about $0.01\ \mu\text{m}^3$. Focusing optics for synchrotron beamlines producing smaller beams down to the order of $10\ \text{nm}$, and due to the higher fluxes, the limits of detection are extended down to the $\text{pg}\cdot\text{g}^{-1}$ region.

Measurements to distinguish the LOD were carried out using a $0.45\ \mu\text{m}$ thin Cu-foil and monochromatic excitation with $9.7\ \text{keV}$. With this setup, the detection limits using the DMM at the BAMline could be calculated with $130\ \text{pg}$ and combined with the CRL the limit is at $5\ \text{fg}$, both with a $95\ \%$ level of confidence. In table 7.2 the average values from 5 measurements are shown together with the results of the calculation for the minimal detectable precipitate size.

Table 7.2 Detection limits at the BAMline with and without CRL (Aperture $360\ \mu\text{m} \times 360\ \mu\text{m}$)

	Live-time	Cu-foil thickness	Density [$\text{g}/\mu\text{m}^3$]	Cu- K_α net-signal	Cu- K_α background	Detection limit	Precipitate size in μm^3	Cube edge length
Slit	60	0.45	$8.96\text{E-}12$	1007345	6597	$130\ \text{pg}$	14.71	$2.4\ \mu\text{m}$
CRL	60	0.45	$8.96\text{E-}12$	175480	921	$5\ \text{fg}$	0.00056	$80\ \text{nm}$

Practical areas for μ -beam scans are in the order of about 100×100 points. In this case this would give a scan area of about $150\ \mu\text{m} \times 150\ \mu\text{m}$ and with a thickness of $100\ \mu\text{m}$ a volume of $2.25 \cdot 10^{-3}\ \text{mm}^3$. Assuming one $5\ \text{fg}$ Cu precipitate in this volume leads to a LOD of about $250\ \text{pg}\cdot\text{g}^{-1}$.

7.1.2 Sample and sample preparation

The sample used for this investigation was the fragment of a solar cell which is shown in the photograph in figure 7.4. The size of the piece was about $8\ \text{mm}$ times $10\ \text{mm}$.

When performing XBIC studies the electron-hole pairs are created very locally around the area where the focused beam hits the sample. Since the diffusion length for electrons and holes is short it necessary to apply a contact over the entire surface of the sample to keep the ways as short as possible. A proper ohmic contact can be made e.g. by rubbing gallium or indium on the surface of the sample, which is possible and was made for the back contact.

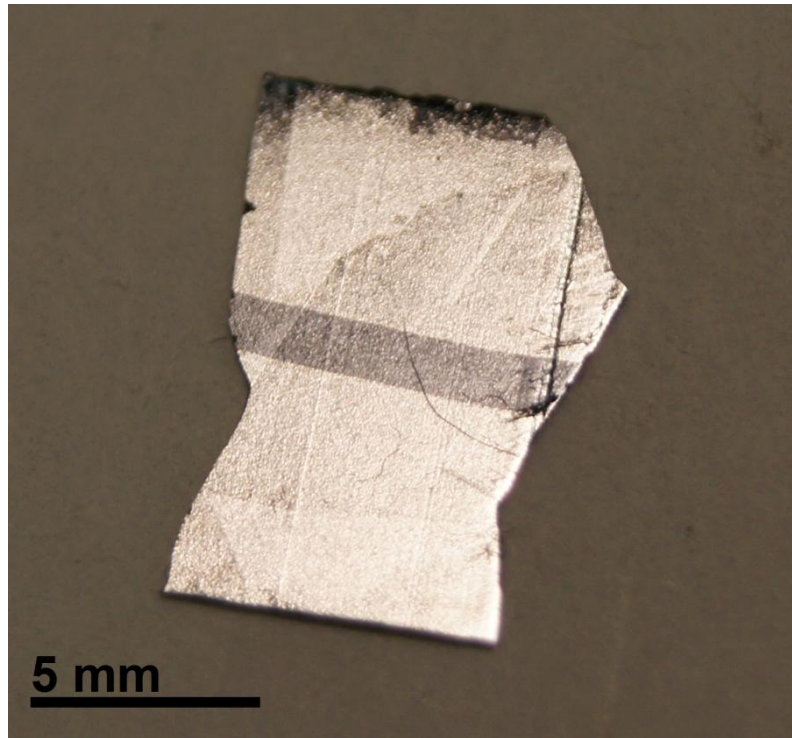


Figure 7.4 Photography of the investigated fragment of a solar cell

For the front contact on the other hand it has to be considered that the radiation has to pass through the contact to reach the sensitive volume of the wafer. Furthermore, if combined XBIC/ μ XRF studies should be conducted, also the fluorescence radiation has to pass to this contact. To keep the absorption low a thin layer of a low Z material has to be applied and therefore an only about 20 nm thick Aluminum layer was applied as front contact. The advantage of having a Schottky contact on the front of the sample and an ohmic contact on its back surface is that no external bias needed to be applied to the contact since the built-in voltage of the Schottky diode was used to collect the charge carriers. To measure the current induced in the cell the contacts were connected with thin gold wires to a sensitive current amplifier.

7.1.3 Preliminary investigations

To save valuable synchrotron beamtime preliminary LBIC (Laser Beam Induced Current) measurements were performed and showed that an interesting area of the piece is near the grain boundary marked in figure 7.5 with the red circle.

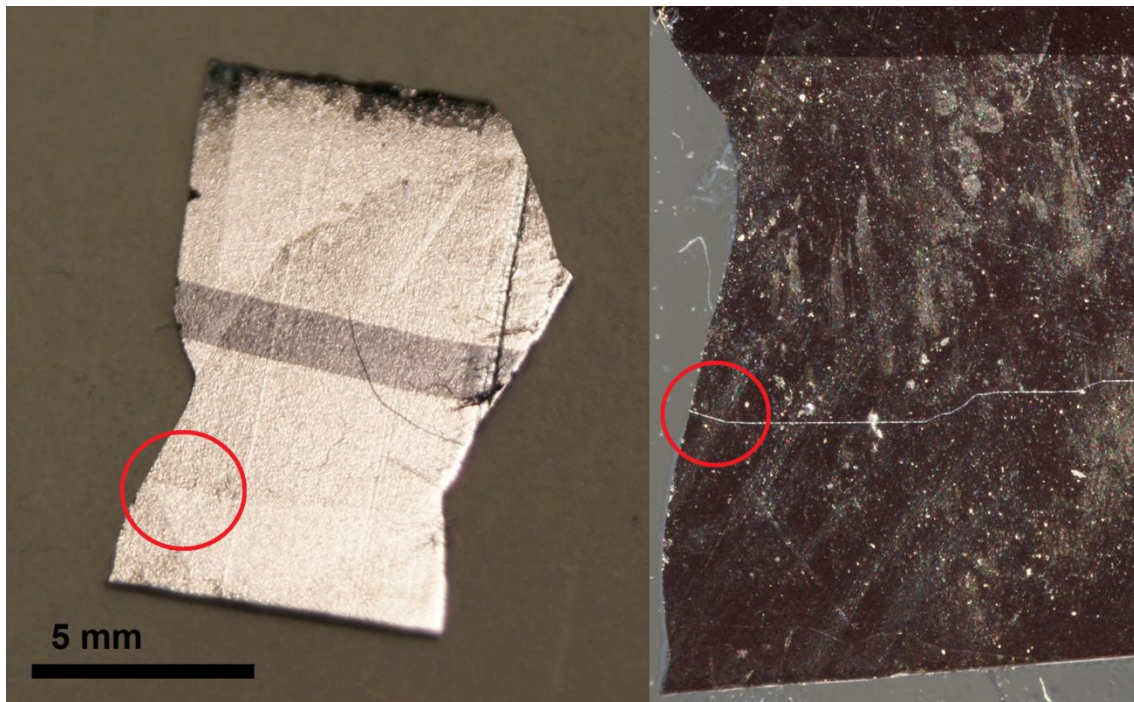


Figure 7.5 Area of interest marked with red circles at a photograph of the solar cell fragment (left) and a detail of the area (right). On the right picture the grain boundary is due to skillful illumination very well visible.

The results of the electron beam induced current (EBIC) measurements and a picture taken with a scanning electron microscope (SEM) are shown in figure 7.6.

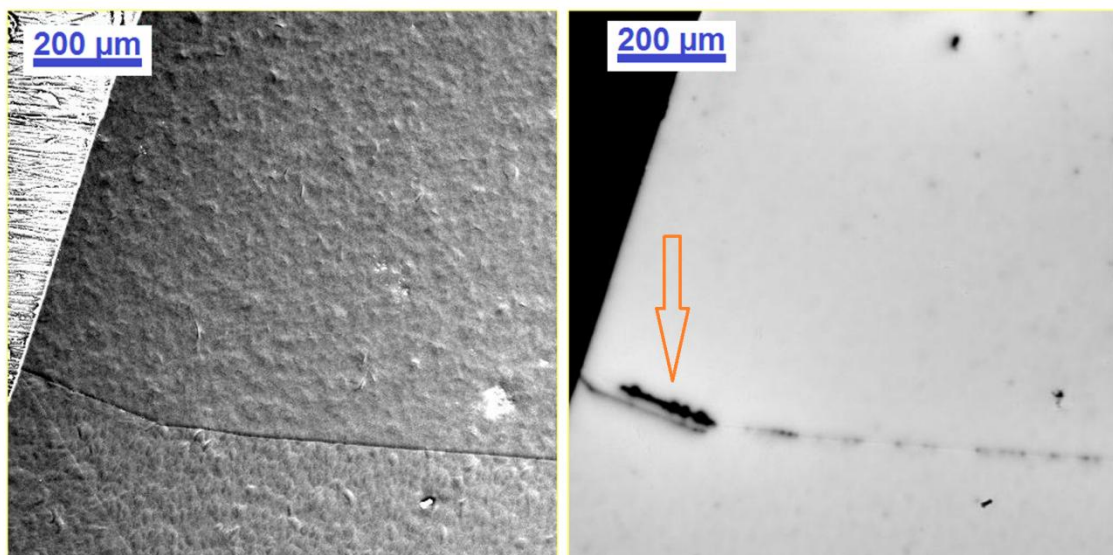


Figure 7.6 SEM picture on the left and the according EBIC mapping on the right hand side.

The EBIC map is scaled from low minority carrier life time in black to maximum lifetime for this cell in white. It is to see that there are some dark spots within the crystal and an almost continuous line of low efficiency along the grain boundary which also can be identified easily in the SEM picture. For this investigation the black area (marked by the orange arrow) near the grain boundary was chosen to investigate more detailed.

7.1.4 XBIC and XRF measurements

Since mainly the transition metals until copper were of interest in this study the CRL designed for a nominal energy of 9.0 keV was chosen. This particular lens has a focal length of 350 mm and a focal spot size of $1.2 \mu\text{m} \times 0.5 \mu\text{m}$, as well as the biggest aperture of all available lenses with $370 \mu\text{m} \times 370 \mu\text{m}$. For large area scans the measuring time per point has to be as short as possible and therefore the highest possible flux through the CRL is needed. This was obtained by bending the second multilayer of the DMM to parallelize the beam in the vertical direction. In chapter 6 it was shown that under this conditions the photon flux on the sample increases by a factor of 2 ($\sim 1.16 \times 10^9 \text{ photons}\cdot\text{s}^{-1}$) leading to a spot size of about $1.6 \mu\text{m} \times 1.5 \mu\text{m}$, which was acceptable for this study.

A restriction when making high resolution measurements is that within reasonable time frames only small areas can be investigated. To cover large areas of the sample a lot of time has to be invested, as for example, to scan an area of $1 \text{ mm} \times 1 \text{ mm}$ with $1 \mu\text{m} \times 1 \mu\text{m}$ resolution (10^6 points) and a measuring of 1 s per point would take approximately 12 days. New developments in silicon drift detectors allowing much higher pulse loads, leading to measuring times in the order of milliseconds per point when combined with very intense, focused X-ray beams. For these scans the sample is moved continuously through the beam and spectra are taken in synchronization with the sample movement ("on the fly"). Using arrays of such fast detectors, the measuring time per pixel can be reduced down to 50 μs [132], if the primary flux and the concentration of the element in question are sufficiently high enough.

A recently developed detector - termed Color X-ray Camera (CXC) [100] - is able to map an area of $12 \text{ mm} \times 12 \text{ mm}$ with a resolution of about $50 \mu\text{m} \times 50 \mu\text{m}$ in a single shot measurement. The measuring time for this map is less than one hour, while to scan the same area point by point at intervals of 1 s each would take about 20 hours. Due to an ongoing development of magnifying polycapillary optics for the CXC a resolution of $10 \mu\text{m} \times 10 \mu\text{m}$ is already available. As an example a fluorescence mapping of the solar cell taken with the

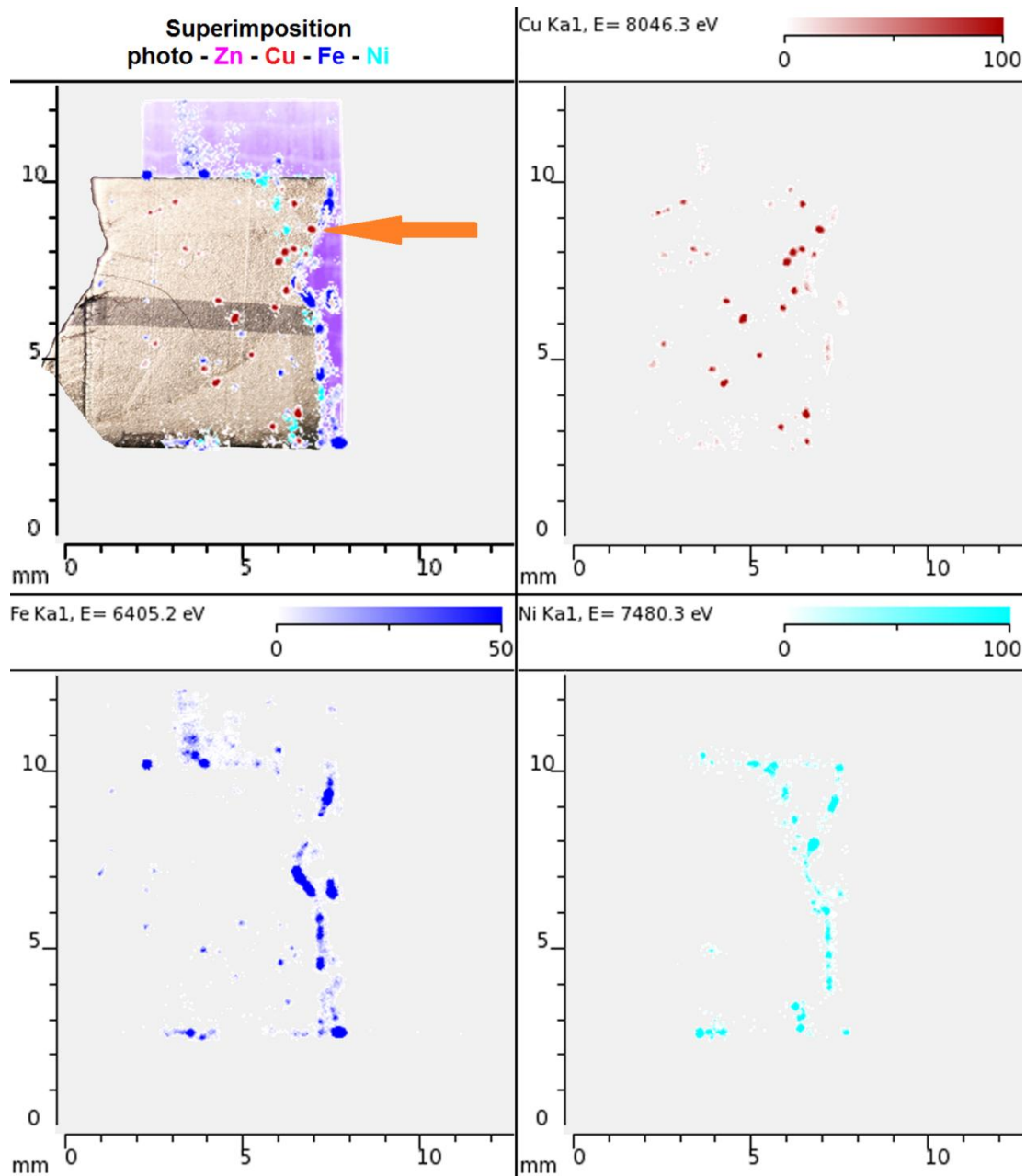


Figure 7.7 Mapping of the solar cell with the color X-ray camera and a 1:1 polycapillary optic.

CXC using a 1:1 optic is shown in figure 7.7. The signal of the $\text{Cu-K}\alpha_1$ is plotted in red, the $\text{Fe-K}\alpha_1$ in blue and the $\text{Ni-K}\alpha_1$ in cyan. The upper left mapping shows these elements superpositioned with the picture of the sample and the $\text{Zn-K}\alpha_1$ signal from the sample holder. The picture of the sample is distorted since the mappings are recorded under an angle of 45° . It is obvious that there are many areas with high Cu concentration as well as some with high Fe and Ni concentration. That Fe and Ni is found in bigger amounts on the borders of the fragment might be due to a contamination from the many times the fragment was handled with a pair of tweezers. The orange arrow points to a bigger Cu precipitate which is in the low efficiency area indicated in figure 7.6 also by an orange arrow.

As mentioned above the amount of Cu precipitates in a solar cell is very low and for a fragment of this size (80 mm²) there should be about 80 precipitates, assuming a volume of 1 μm³ each and therefore it is necessary to scan large areas of the sample to find them. Beside of that a fraction of the copper is not detectable since the local concentration is too low as e.g. at the grain boundaries or in very small precipitates. Therefore the mapping in figure 7.7 shows only about 40 precipitates which is just half of what was expected.

When attempting to develop a procedure for locating precipitates in multicrystalline silicon and considering the values in table 7.1, a scan with a 100 μm × 100 μm aperture provides initial screening and at a measuring time of 5 seconds per pixel and a scan of 1 mm × 1 mm

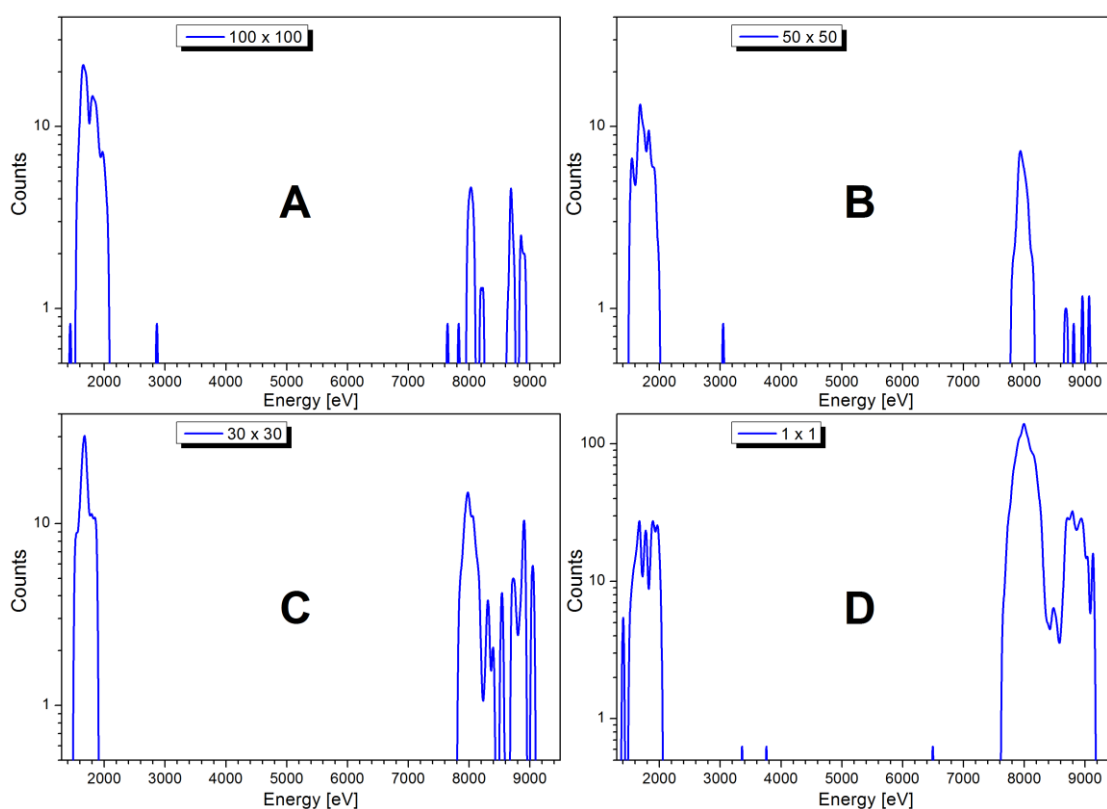


Figure 7.8 Fluorescence spectra of the highest Cu signal with different square apertures and the CRL

is completed in less than 9 minutes. Since the background of these spectra is practically zero (see figure 7.8 left hand side) it is appropriate to just add up all the counts in a ROI around the Cu-K_α energy to obtain a fast online analysis.

In figure 7.8 the spectra of measurements with square apertures with an edge length of 100 μm (A), 50 μm (B) and 30 μm (C) and with the CRL (D) are shown, representing the spectra with the highest Cu signal from the according scans shown in figure 7.9. For the mappings the spectra were normalized with the ionization chamber current and the sum of 7 channels (±80 eV) around the Cu-K_α energy was plotted.

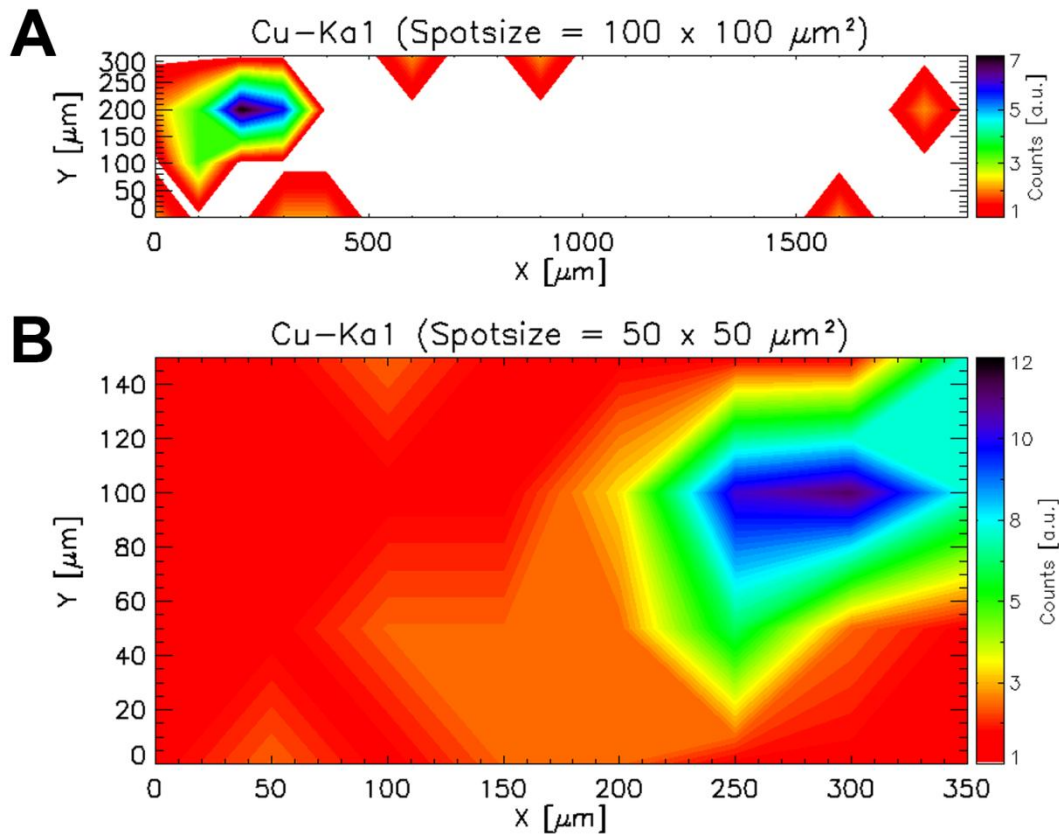


Figure 7.9 Fluorescence mappings with different square apertures with an edge length of 100 μm (A) and 50 μm (B) measured for 5, and 10 seconds, respectively.

Figure 7.9A shows the mapping of the copper ROI data for a 2 mm \times 0.3 mm scan of a single crystal in a polycrystalline solar cell, in which a picture of the copper content can be drawn with a total of just seven counts at the maximum. The area in which a precipitate is most likely to be found has a size of approximately 350 μm \times 150 μm , which was scanned with a 50 μm \times 50 μm aperture and 10 s per pixel. Under these conditions, the map in figure 7.9B was obtained within 4 minutes.

Figure 7.10 shows a scan with a 30 μm \times 30 μm aperture over an area of 390 μm \times 360 μm with a measuring time of only 2 s per point that requires less than 6 minutes.

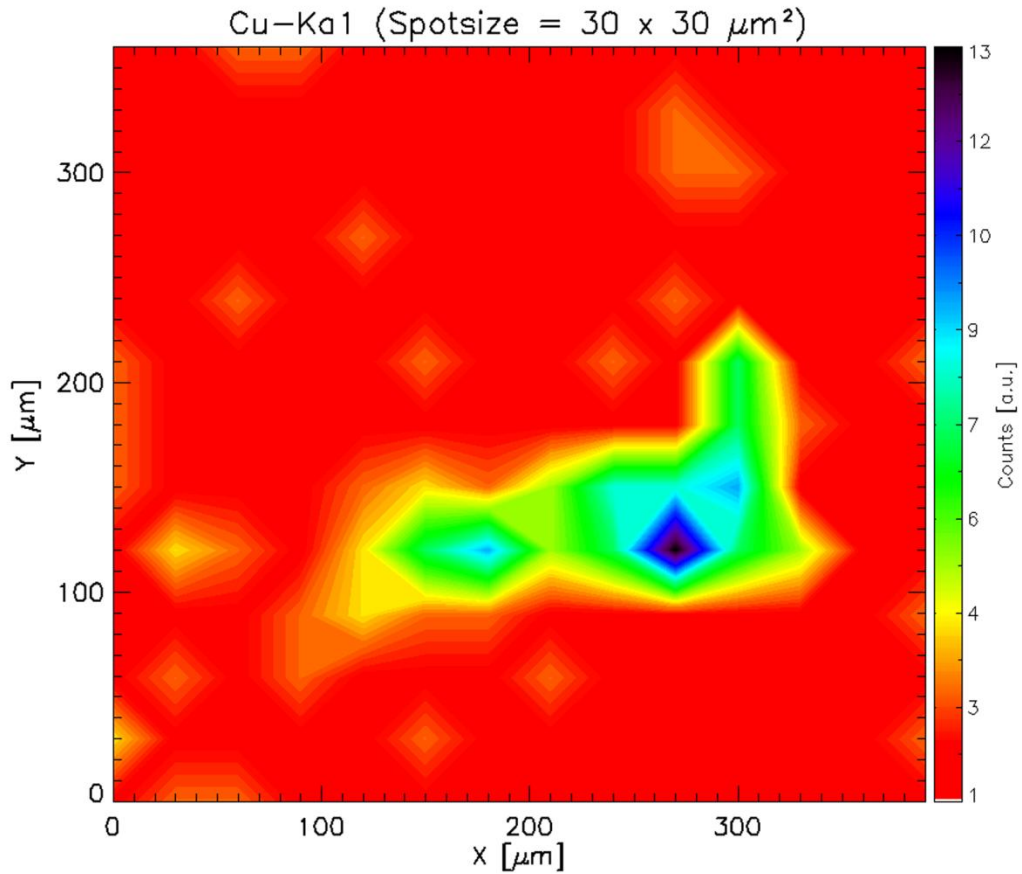


Figure 7.10 Fluorescence map with a aperture of 30 μm \times 30 μm

With this resolution it already might be suspected that there is more than one precipitate in this area, because the dimensions of the area with a high concentration here is about 30 μm \times 210 μm (1 pixel \times 7 pixel) and the maximum size of the precipitates is usually just several μm . Figure 7.11 shows a CXC map of this area with a 1:6 magnifying optic.

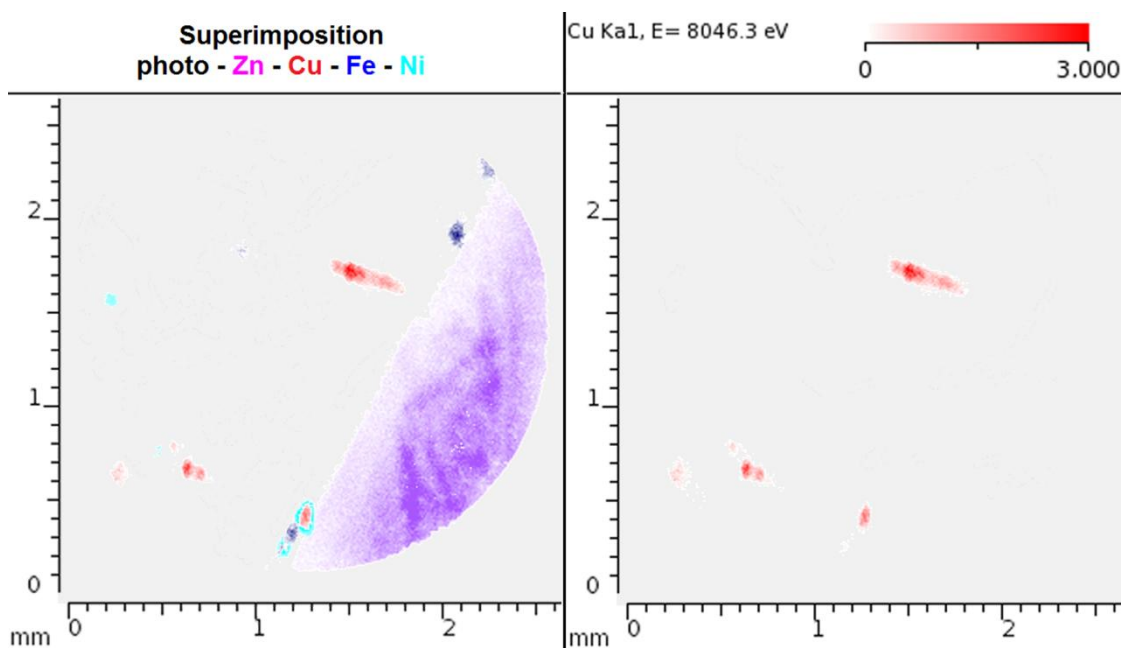


Figure 7.11 Mapping of the solar cell with the color X-ray camera and a 1:6 magnifying optic.

When using this polycapillary optic in front of the CXC the resolution is increasing to about $10\ \mu\text{m} \times 10\ \mu\text{m}$ and it becomes even more evident than in figure 7.10 that there are several precipitates.

A scan of a $300\ \mu\text{m} \times 140\ \mu\text{m}$ area was made with a monocapillary optic with a spot size of about $4\ \mu\text{m}$. Figure 7.12 shows the XBIC- and the Cu-map of this scan as well as to compare the EBIC picture form above.

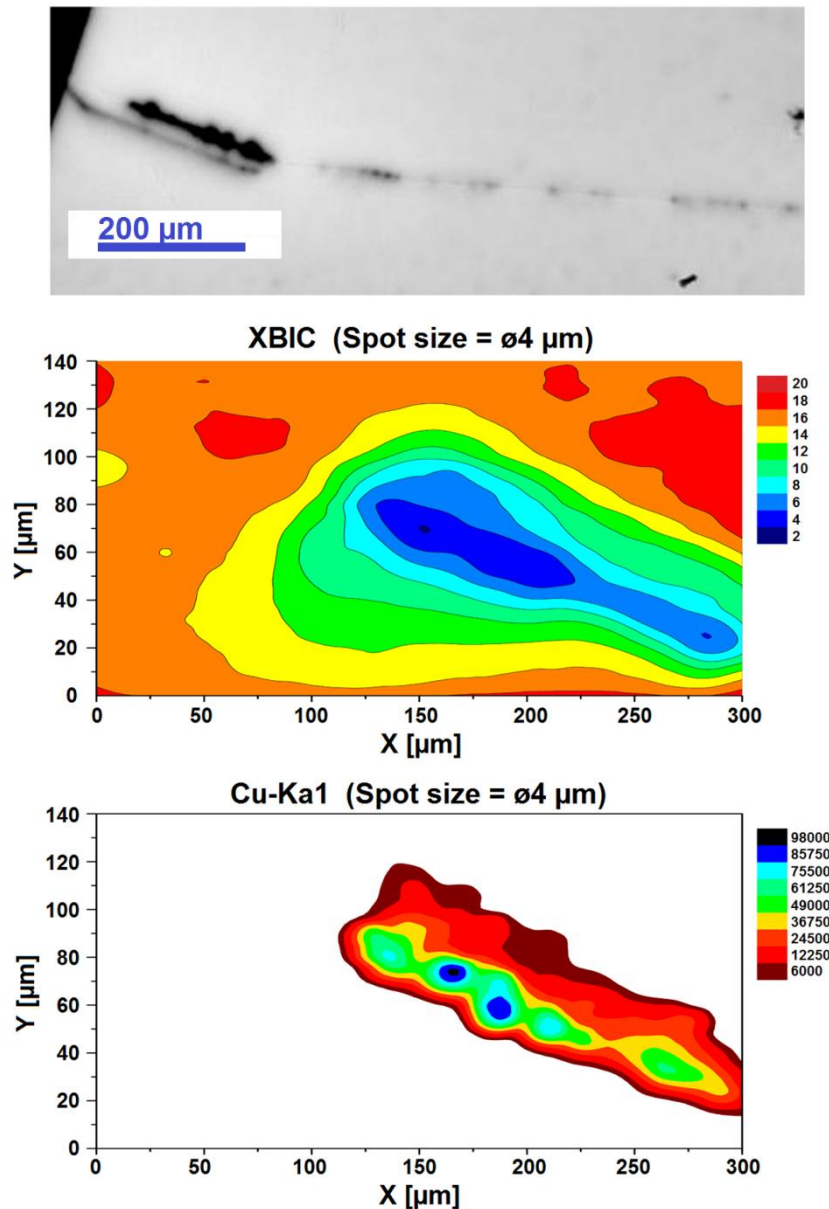


Figure 7.12 EBIC, XBIC- and μ -XRF Cu-maps of an electrically ineffective area

It is evident that the EBIC picture and the mapping of the XBIC signal look quite similar, showing a low efficiency area near the grain boundary, which is as to see in the μ -XRF map rich on Cu. With this resolution it is clearly to see that there should be at least five Cu precipitates within the area.

Finally an area of $270\ \mu\text{m} \times 130\ \mu\text{m}$ was selected from the mapping with the $30\ \mu\text{m} \times 30\ \mu\text{m}$ aperture for the high resolution scan with the CRL. Figure 7.13 shows an overlay of two pictures of the solar cell taken with the long-range microscope, where the cross-hairs within the small white squares are marking the beam position at the starting and the end point of the scan.

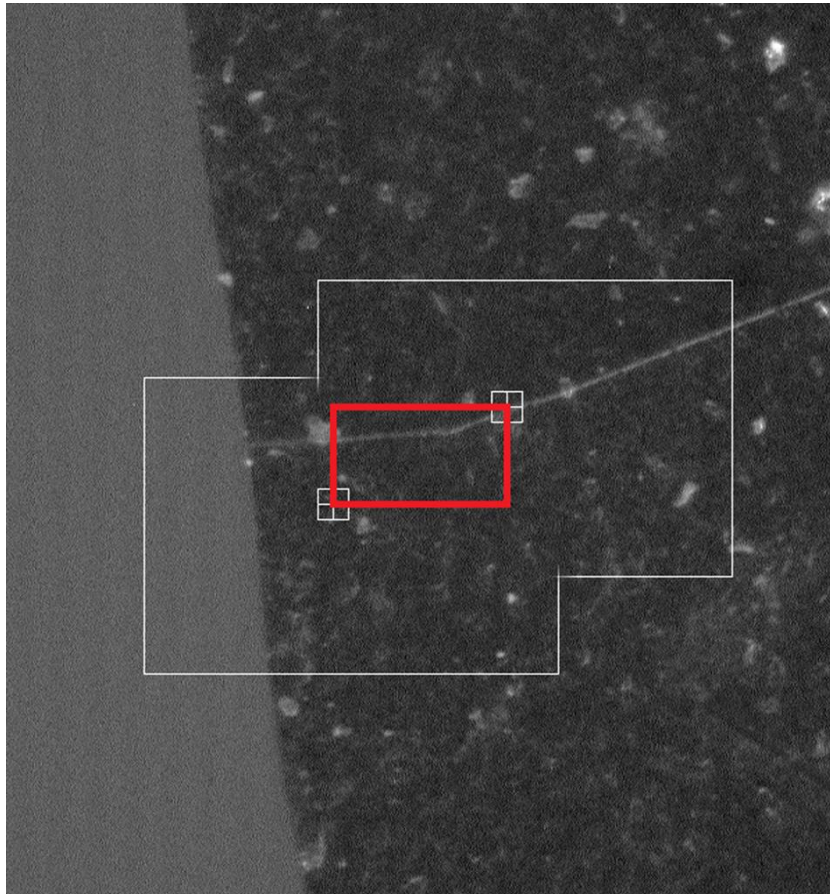


Figure 7.13 Microscope picture of the high resolution scan area

The red rectangle marking the scan area has about $35000\ \mu\text{m}^2$ which, with the DCM and a spot size of $1\ \mu\text{m}^2$ a measuring time of 2 s per point was necessary which lead to a total scan time of about 20 hours.

Figure 7.14 shows a 3D- and 2D-mapping of the Cu-K_α signal from this scan. It is clearly to see that there are three precipitates at the coordinates $(x,y) = (172,105)$, $(148,102)$ and $(200,90)$ with a strong signal and several precipitates with weaker signals.

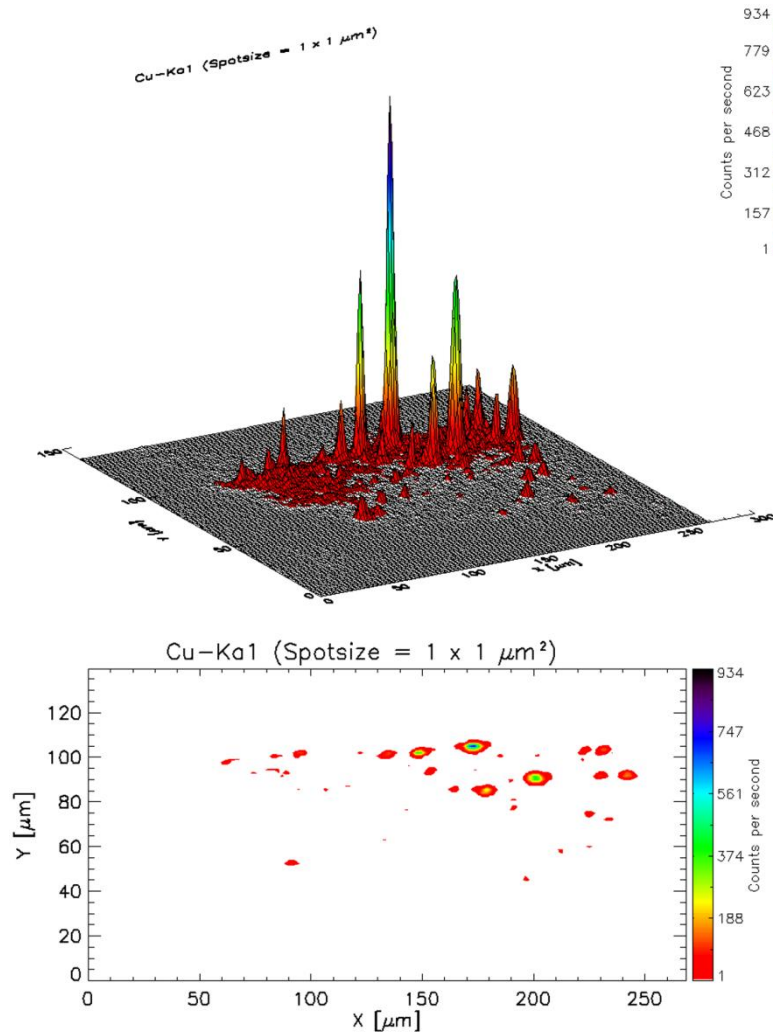


Figure 7.14 Mapping of the Cu-signal for the high resolution scan

The Fe-signals in this area were very weak as shown in figure 7.15, but still exhibited some iron contamination even if in the maximum were only 7 counts (~ 4 cps) compared to the 934 counts (~ 470 cps) for Cu.

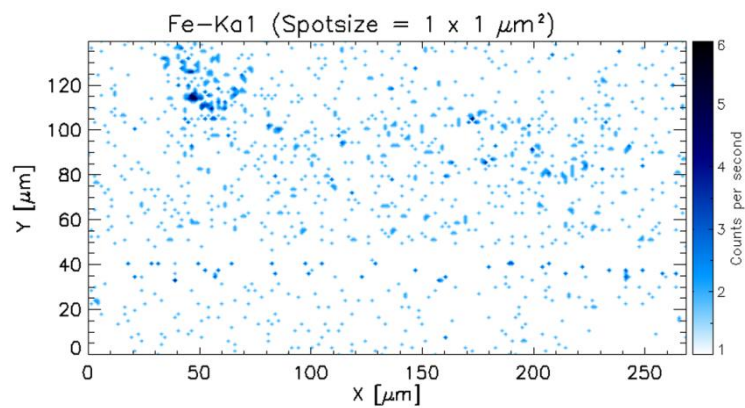


Figure 7.15 Fe map for the high resolution scan with a maximum of 7 counts

Due to the low count rate for Fe and the other impurities besides Cu, a significant increase of the measuring time per point would have been necessary to get a better mapping of their distribution in the solar cell. Since high resolution measurements already require a lot of valuable synchrotron beamtime, an obvious option was to switch to the DMM for higher flux and better count rates. Due to the broader energy bandwidth of the DMM a lower resolution of $1.5 \mu\text{m} \times 1.5 \mu\text{m}$ had to be taken into account, but therefore a measuring time of 1 s per point was sufficient. An area of $250 \mu\text{m} \times 60 \mu\text{m}$ around the copper and iron precipitates was scanned again and the mappings of the Cu and Fe distribution in this area is shown in figure 7.16. Note the count rates of about 48500 cps for Cu and 470 cps for Fe.

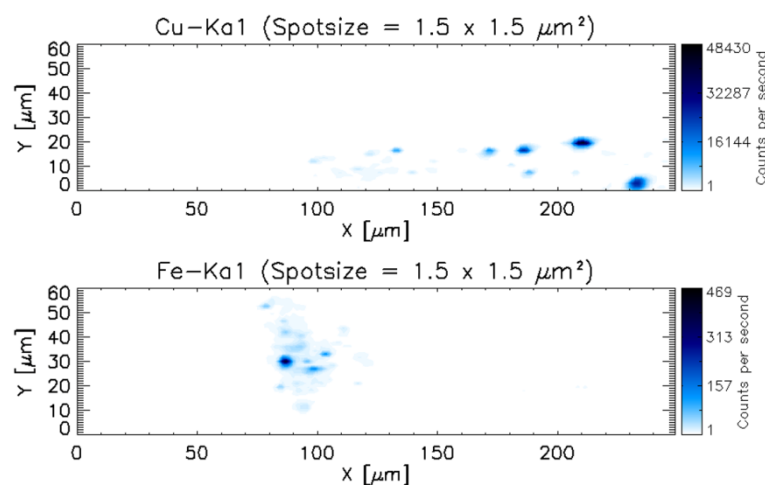


Figure 7.16 Cu- and Fe-map with $1.5 \mu\text{m} \times 1.5 \mu\text{m}$ resolution measured with the DMM.

An interesting fact to notice here is that Fe and Cu are in separate areas within the solar cell.

In figure 7.17 mappings of the elements Ni, K, Ca, Cl, Ti, Co, Cr and Mn can be found. While Ni, K, Ca, and Cl are only to find in the Fe rich area, it appears that Ti, Co, Cr and Mn are present in both areas but in low concentrations. Even if a lot of elements are present in the Fe rich area except of the Co none of them matches with the Fe maxima. Obviously there is no correlation between Cu and any other element and furthermore the other elements also do not show any strong correlation with each other.

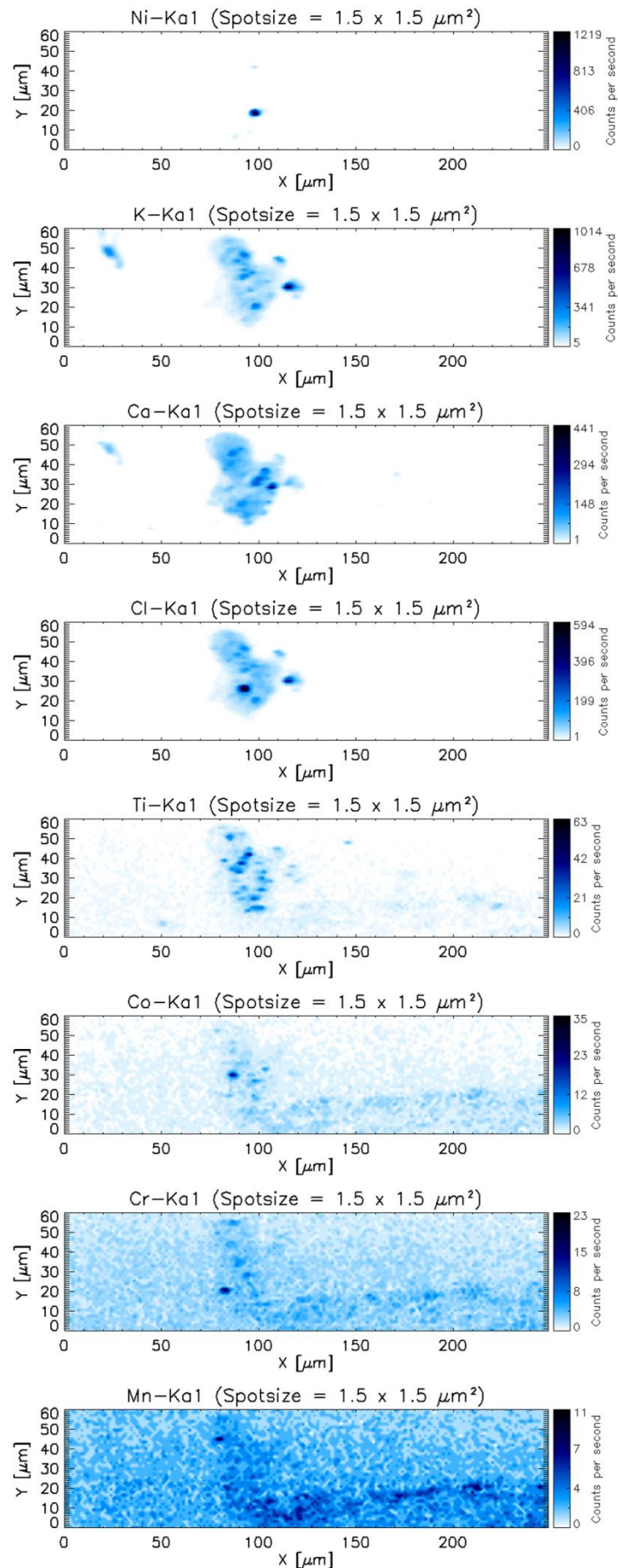


Figure 7.17 Fluorescence mappings of different elements measured with the CRL using the DMM.

7.1.5 Detailed analysis of the Cu precipitates

A good statistic is always an important objective of quantitative analysis. If the statistical error should be, for example, in the order of 1 % of the signal, the measuring time had to be increased - according the Poisson statistics - until more than 10^4 counts are collected; for an error in the order of 0.1 % a total of 10^6 counts is required.

Before conducting quantitative measurements on the sample, areas around the precipitates had to be scanned with a smaller step size (e.g. $0.5 \mu\text{m}$), to ensure that the beam irradiates the precipitate under optimal conditions. The energy region around the Cu- K_β fluorescence line, normalized by the Cu- K_α intensity, is plotted in figure 7.18 for measurements of the selected precipitates as labeled in the upper right corner of figure 7.18.

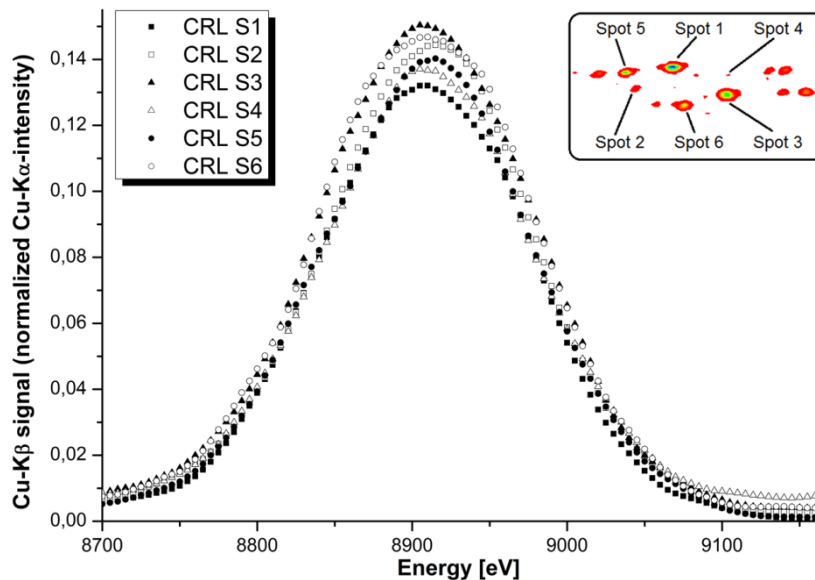


Figure 7.18 Fluorescence spectra of the Cu- K_β signal of different precipitates, normalized by the Cu- K_α intensity. The difference in the Cu- K_β signal intensity is produced by a difference in the ratio of the Cu-K line signals for precipitates located at different depths in the silicon wafer. Inset: Selected precipitates taken from figure 7.14.

It became evident from their normalization that the relative intensity of the Cu- K_β lines is not constant. Instead, the K_α to K_β ratio varies between different spots. The reason for this finding is that the precipitates are not only located in the wafer surface but also deeper inside the wafer. Therefore, the emitted fluorescence radiation has to pass through different thicknesses of silicon material, where it is partially absorbed. The relative intensity of the K_β line increases with respect to the K_α line for deeper positions of the copper precipitates since the absorption coefficient of silicon for the Cu- K_α line is larger than for the Cu- K_β line.

The analysis of a reference material with known composition is necessary in order to determine the nominal K_α/K_β ratio as well as to calculate the size of the precipitates. A thin Cu-

foil with 0.45 μm thickness was used as reference and measured using the DMM and a recording time of 1 s at an average ring current of 200 mA. The data show that the nominal ratio for the Cu-K lines is 7.26. Estimations for the depths of precipitates can be made by calculating the K_{α}/K_{β} ratio through different thick layers of silicon. The graph in figure 7.19 shows the change in the ratio of the copper lines as a function of the overlying silicon thickness.

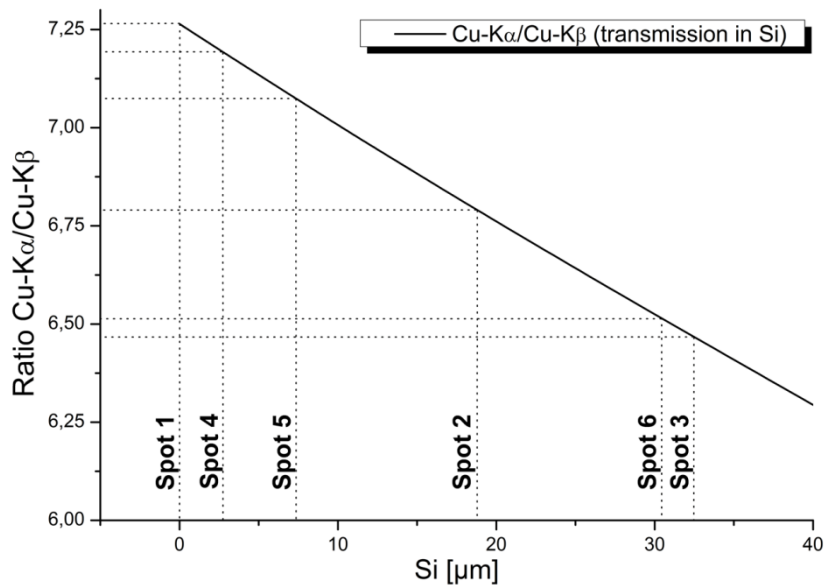


Figure 7.19 Calculated $\text{Cu-K}_{\alpha}/\text{Cu-K}_{\beta}$ intensity ratios as a function of the thickness of the transmitted silicon layer. The measured ratios in the different spots of a solar cell were used to determine the depth of the precipitates within the wafer.

The horizontal and vertical lines assign the measured ratios to the depth of different precipitates in the sample. Taking the depth into account, by considering the absorption of the overlying Si, the “real” Cu-K_{α} count rate from the precipitates was calculated. Finally, with the Cu-K_{α} count rate of the 0.45 μm thick copper foil as reference, the volume of the Cu precipitates was determined and the sizes were then calculated by assuming a cubic symmetry. The corresponding results of the sizes and depths of the labeled precipitates are summarized in table 7.3.

Table 7.3 Depth and sizes of copper precipitates detected in a mc silicon wafer.

Label of precipitate	Count rate Cu-K_{α} [cps]	Time [s]	Depth in Si [μm]	Volume Cu (corrected) [μm^3]	Size [nm]	Error of not corrected values
Cu-foil	36421	60	0	1	1000	1
Spot 1	2627	120	0	0.0721	416	0.00 %
Spot 2	471	600	18.8	0.0197	270	13.04 %
Spot 3	2419	120	32.4	0.1368	515	21.40 %
Spot 4	150	1800	2.7	0.0044	163	1.99 %
Spot 5	1322	240	7.4	0.0428	350	5.35 %
Spot 6	337	900	30.4	0.0182	263	20.22 %

Column 2 and 3 of table 7.3 show the actual count rate and the measuring time to collect more than 10^4 counts for the Cu-K $_{\beta}$ line. The calculated depth values (see figure 7.19) are shown in column 4 and the corrected volumes of the precipitates according to their depths can be seen in column 5. It is obvious that precipitates are at different depths in the solar cell when comparing the precipitates labeled Spot 1 and Spot 3 by looking at the K $_{\alpha}$ /K $_{\beta}$ ratio of 7.26 and 6.47. The impurity in Spot 1 is located on the surface and that of Spot 3 at a depth of about 32 μm . By taking this into account, calculation of the size of the precipitate leads to the conclusion that the one in Spot 3 is about two times larger than the one in Spot 1. Without this depth information, the calculations would have led to the wrong conclusion that the two precipitates are of similar size.

The values in table 7.3 are estimations afflicted with systematical and statistical errors. In the absence of better results, the systematical error for Cu is 5.85 %, which was calculated from a measurement series on a gold reference material (Aurubis NA-Au 31) including $1062 \mu\text{g}\cdot\text{g}^{-1}$ Cu; this results in an overall error on the order of 10 % for all values in table 7.3.

The two bigger spots, Spot 1 and Spot 3, were chosen to carry out μ -XANES measurements. To calibrate the edge energy a Cu-foil was measured as standard and the offset of the monochromator was adjusted to fit the edge energy of 8979 eV. The resulting XANES spectra and the comparison with the Cu-foil can be seen in figure 7.20

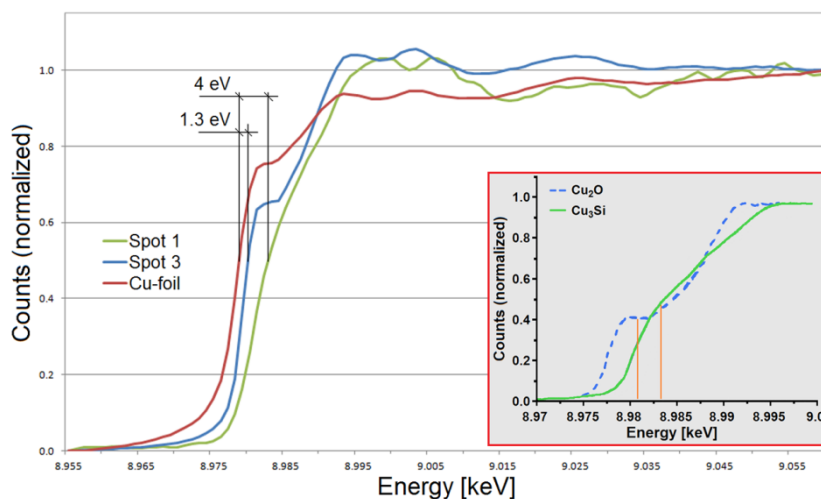


Figure 7.20 XANES measurements with the CRL on Spot1, Spot3 and a Cu-foil. The inset shows graphs from Cu-standards adapted from literature sources (e.g. [133, 134])

The measurements showed that these precipitates are not metallic copper since the spectra are shifted by 1.3 eV and 4 eV respectively. Comparing the form of the spectra and the edge shift to spectra measured by other groups [133, 134] it is most probable that the precipitate in Spot 1 is a copper silicide (Cu_3Si) and the one in Spot 3 is a copper oxide (Cu_2O).

7.2 Portuguese glazed ceramics ^[109]

Ceramic fragments (XVI-XVIII centuries) from two production centers in Portugal (Coimbra and Lisbon) were studied to gain a better understanding about the production technologies used during this time. Two different kinds of samples were available from Coimbra namely faiences and tiles, while from Lisbon only tiles were investigated.

This type of ceramics consists of three main parts, the ceramic support (body), the glaze and the surface decoration (color). Within this study only the system decoration/glaze was investigated to distinguish if there are differences in mixing procedures, firing steps or firing temperatures between the two kinds of ceramic and the production centers. Also the diffusion ability of the pigments into the base glaze depending on their compositions was studied. The way these layers interfere with each other depends on the chosen materials and on the manufacturing process. Previous studies with different analytical techniques revealed already valuable information about these pieces [114, 135, 136] while the aim of this investigation was to give complementary information about the possible production techniques. In order to examine these effects, high resolution scans (μ -XRF) at well prepared cross sections of the samples were performed to provide profiles of characteristic elements from the surface to the body. The key elements distinguish by previous studies are Co for the blue, Mn for the purple, Cu for the green and Sb for the yellow color as well as Pb for glaze and Fe for the body.

7.2.1 Samples and sample preparation

Table 7.4 shows a list of the analyzed fragments which were chosen to provide a sample from each production center and color.

Table 7.4 Analyzed samples significant from each production centre and type.

Sample	Origin	Type	Color	Detected elements	Key elements
C34	Coimbra	Faience	Blue	Fe, Co, Ni, As	Co
AZCO7	Coimbra	Tile	Blue	Fe, Co, Ni, As	Co
AZLX1	Lisbon	Tile	Blue	Fe, Co, Ni, As	Co
C29	Coimbra	Faience	Purple	Mn, Fe, Ba	Mn
AZCO3	Coimbra	Tile	Purple	Mn, Fe, Ba	Mn
			Green	Cu	Cu
AZLX3	Lisbon	Tile	Purple	Mn, Fe, Ba	Mn
			Green	Cu	Cu
C41	Coimbra	Faience	Yellow	Fe, Sb, Pb	Sb
AZCO1	Coimbra	Tile	Yellow	Fe, Sb, Pb	Sb
AZLX2	Lisbon	Tile	Yellow	Fe, Sb, Pb	Sb

The elemental composition of the used pigments was obtained previously by X-ray fluorescence measurements [114] and the last column of table 7.4 shows the key elements chosen to represent the respective color. Since the fracture surface of the pieces is rough and not perpendicular to the sample surface, small areas of the sample had to be polished to perform the μ -XRF cross section scans.

7.2.2 Experimental setup

Figure 7.21 shows the setup for this study which is basically a standard XRF setup with the detector perpendicular to the X-ray beam. To avoid the excitation and detection of more than one layer as shown on the right side of figure 7.21 (A), the sample was mounted horizontally (B) and the scan was conducted by moving the sample in vertical direction.

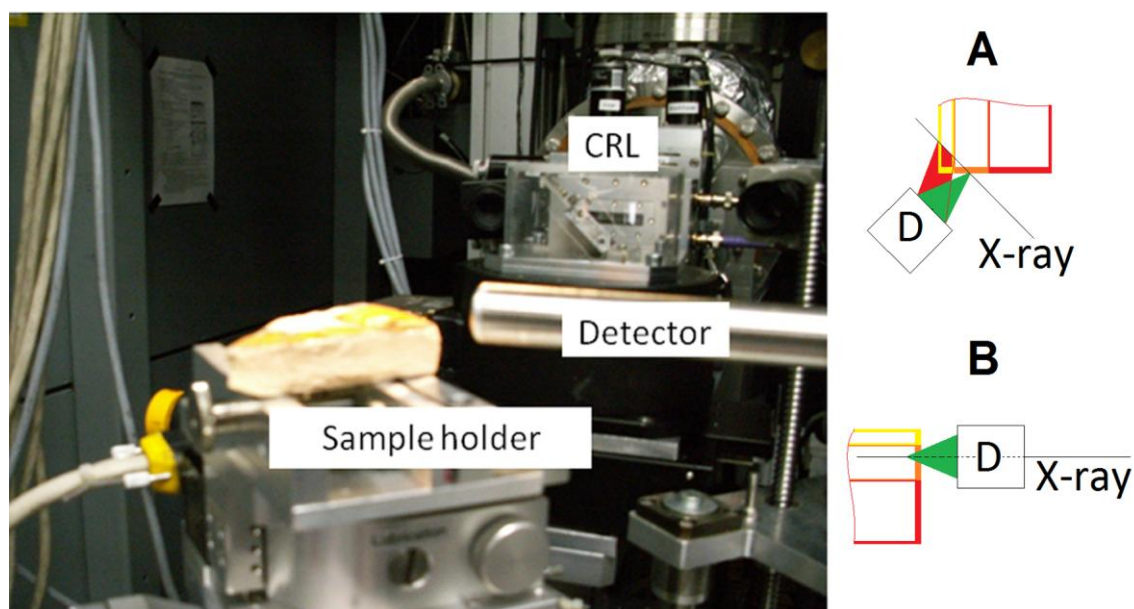


Figure 7.21 Setup of the μ -XRF experiment at the BAMline. Inset A and B shows the differences in the excitation and detection paths when mounting the sample horizontally or vertically.

In order to analyze the yellow pigment, with the key element Sb (K-edge at 30.491 keV), the lens with a nominal energy of 33.2 keV, an aperture of 60 μm and a gain of 4900 had to be used. Although this lens would have been suitable to monitor the key elements of the other pigments (Co, Cu, Mn), the glaze (Pb L3-edge at 13.035 keV) and the body (Fe) the lens with 20 keV nominal energy was chosen to perform this scans. This has the advantages that the absorption efficiency for the monitored elements is better and the photon flux on the sample through this lens is more than 4 times higher due to the bigger aperture of 157 μm (gain \sim 22000). Since the expected layer thickness was in the order of tens of μm , the DMM with a spot size of 1.6 $\mu\text{m} \times$ 1.5 μm could be used for this measurements.

7.2.3 Results

The cross section scans were conducted by scanning the sample vertically through the beam with a step size of 1 μm collecting fluorescence spectra for 30 seconds at each point. For each sample and color the scans were repeated at two positions on the sample about 100 μm to 250 μm next to the previous scan. After collecting the data the spectra were fitted with PyMCA [137] and the fitted values were used for plotting elemental profiles.

Comparing the profiles from the repeated scans on the same pigment showed for all cases only small differences. Due to this the results in the following section are presented as the averaged data from these three scans.

7.2.3.1 Blue decorations

Figure 7.22 shows pictures of the samples and the cross sections as well as the elemental profiles of the key elements Co for the blue color, Pb for the glaze and Fe for the body. The red lines in the microscope pictures indicate the scan regions for each sample.

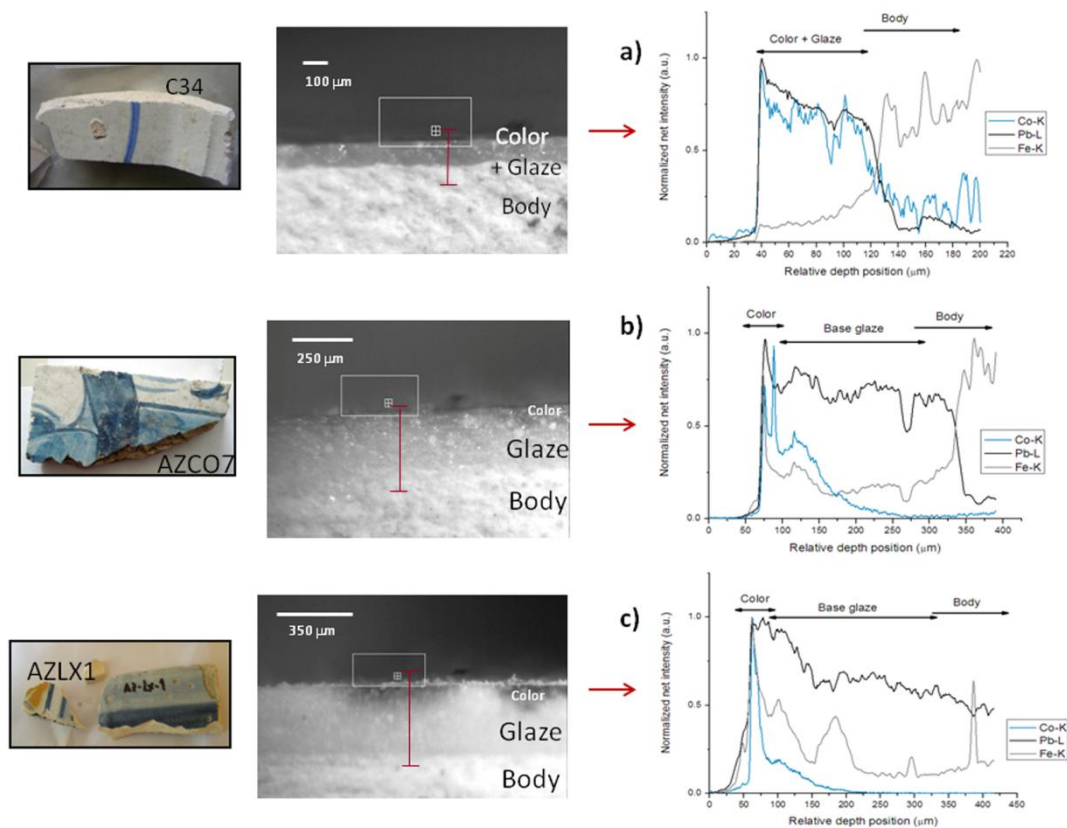


Figure 7.22 Elemental profiles from cross-section scans of two samples from Coimbra C34 (a) and AZCO7 (b) and one sample from Lisbon AZLX1 (c).

Monitoring the Pb signal shows that the thickness of the glazes is one major difference between these samples. While in the faience sample C34 (figure.7.22a) the glaze is approximately 120 μm thick, the tile samples (AZCO7 and AZLX1) have glaze thicknesses between 350 μm and 400 μm (figure 7.22b and c). Another difference can be seen by tracking the Co signals, where for the tiles it is obvious that they have two layers (glaze and pigment separated), while the faience has only one layer. This means that the pigment was applied together with the glaze in only one firing process.

Comparing the two tiles (AZCO7 and AZLX1) it is to see that the Co-signal vanishes at a depth of about 150 μm in the sample from Coimbra and at about 125 μm in the one from Lisbon. The deeper penetration of the pigment particles through the glaze can have different reasons as e.g. a higher content of fusible components in the glaze (lead oxides and alkaline compounds) or a higher firing temperature. Furthermore there is a big difference in the profiles of the Pb-signals. While in sample AZCO7 the signal drops abrupt at the glaze/body interface there is almost no change in sample AZLX1, meaning that this ceramic body allows a higher intake of the glaze.

7.2.3.2 Purple decorations

For the purple color the compound *Psilomelane* $[(\text{Ba},\text{H}_2\text{O})_2\text{Mn}_5\text{O}_{10}]$ was used and therefore Mn was chosen to be the monitored element. Figure 7.23 shows pictures of the samples C29 and AZCO3 (a faience and a tile from Coimbra) and AZLX3 (from Lisbon) together with pictures of their cross sections and the elemental profiles for Mn, Pb and Fe. Again the red lines in the microscope pictures indicate the regions where the cross section scans were performed.

Once again it is to see that there is no interface between color/glaze and the glaze thickness is about 150 μm in the faience sample (figure 7.23a). There is however a stronger connection between glaze and body in this sample as seen before (figure 7.22a), to observe by the smoother decrease of the Pb and increase of the Fe profile.

Comparing the tiles it is to see that the pigment is equally well dispersed through the glaze (figure 7.23b and 7.23c). However, the Mn profile in the sample C29 shows a broader maximum at the surface (~ 50 μm) than sample AZLX3 (< 25 μm). Since the purple motifs were applied together with a green colored layer the Cu signal (key element for the green color) was also plotted and shows the same behavior as Mn. The glazes are about 250 μm and

300 μm thick and again a smoother elemental exchange at the interface glaze/body is observed in the sample from Lisbon.

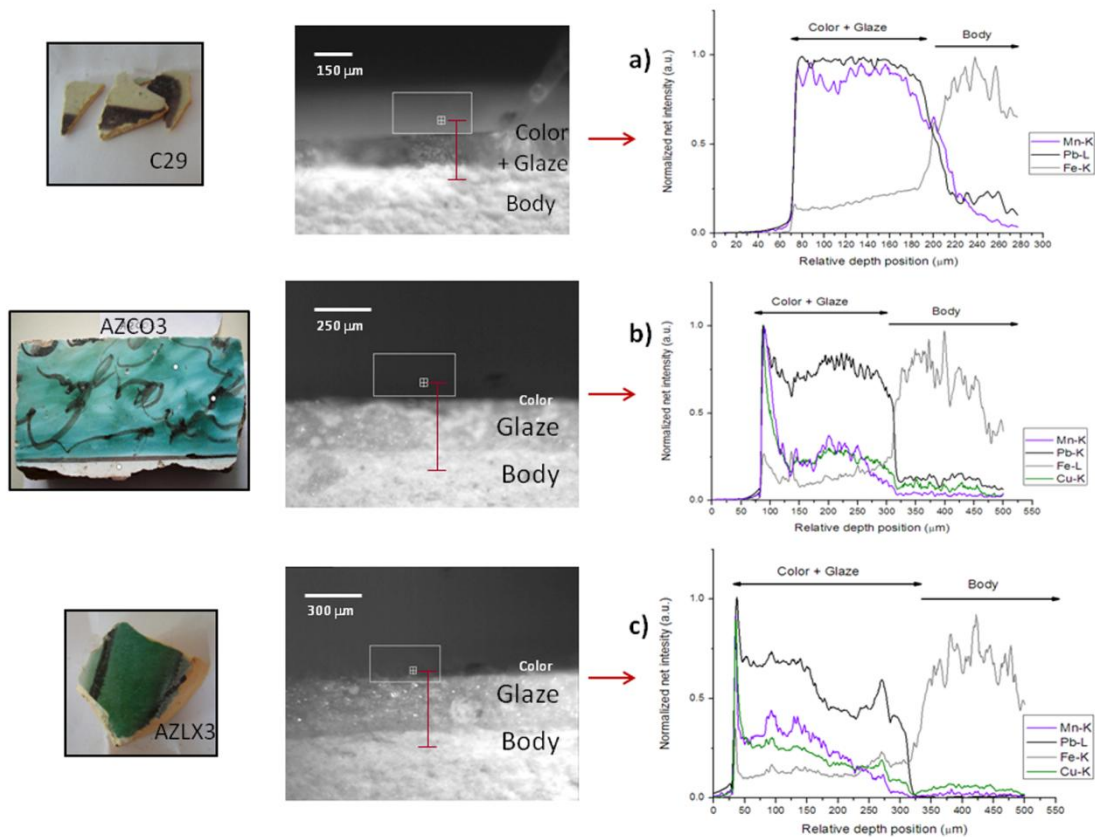


Figure 7.23 Elemental profiles from cross-section scans of two samples from Coimbra C29 (a) and AZCO3 (b) and one sample from Lisbon AZLX3 (c).

7.2.3.3 Green decorations

In figure 7.24 cross-section scans of samples containing green decorative motifs are shown. Since no faience with green motifs was available only a tile from Coimbra (AZCO3) and one from Lisbon (AZLX3) could be compared. These samples are the same as the ones where the purple color was monitored, but here the scans were carried out in regions where only the green color was present. The Cu signal shows that the intake into the glaze is higher in sample AZLX3, while a broader maximum is observed at the surface of sample AXCO3 from Coimbra. Furthermore, the chemical exchange between glaze and body seems to be more pronounced in the sample from Lisbon than in the sample from Coimbra. The glazes are - as already seen when monitoring the purple pigment - about 250 μm and 300 μm thick.

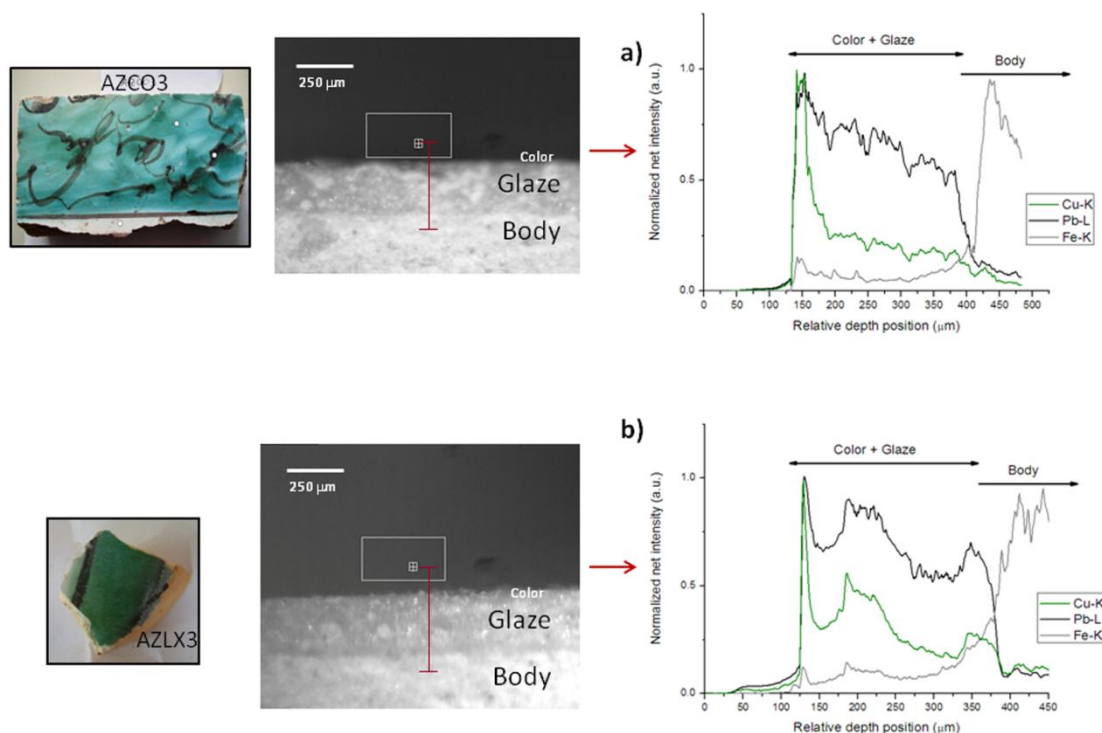


Figure 7.24 Elemental profiles from cross-section scans of a tile from Coimbra AZCO3 (a) and one tile from Lisbon AZLX3 (b).

7.2.3.4 Yellow decorations

In figure 7.25 the elemental profiles of sample C41 a faience and AZCO1 a tile from Coimbra as well as sample AZLX2 a tile from Lisbon all containing yellow decorations are compared.

Conversely to what has been seen before regarding the faiences features, new aspects arise when investigating the yellow pigment. When looking at figure 7.25a it is obvious that there is a pigment layer of about 30 μm applied on a glaze layer of about 180 μm thickness. This separation may occur due to a separate firing stage just for the pigment and/or due to the fact that the lead-antimony composite which gives the yellow color forms large crystals which make it difficult for the pigment to disperse through the glaze. At the interface glaze/body once again the smooth decreasing of the Pb signal and smooth increasing of the Fe signal is to observe.

Comparing the profiles of the tiles (figure 7.25b and 7.25c), the pigment layer on both samples has the same thickness of about 100 μm . However the drop of the Pb signal at the color/glazer interface is higher at sample AZCO1, indicating the possibility of separate firing stages for glaze and pigment. Again at the interface glaze/body the elemental exchange between Pb and Fe is smoother in the sample from Lisbon (AZLX2).

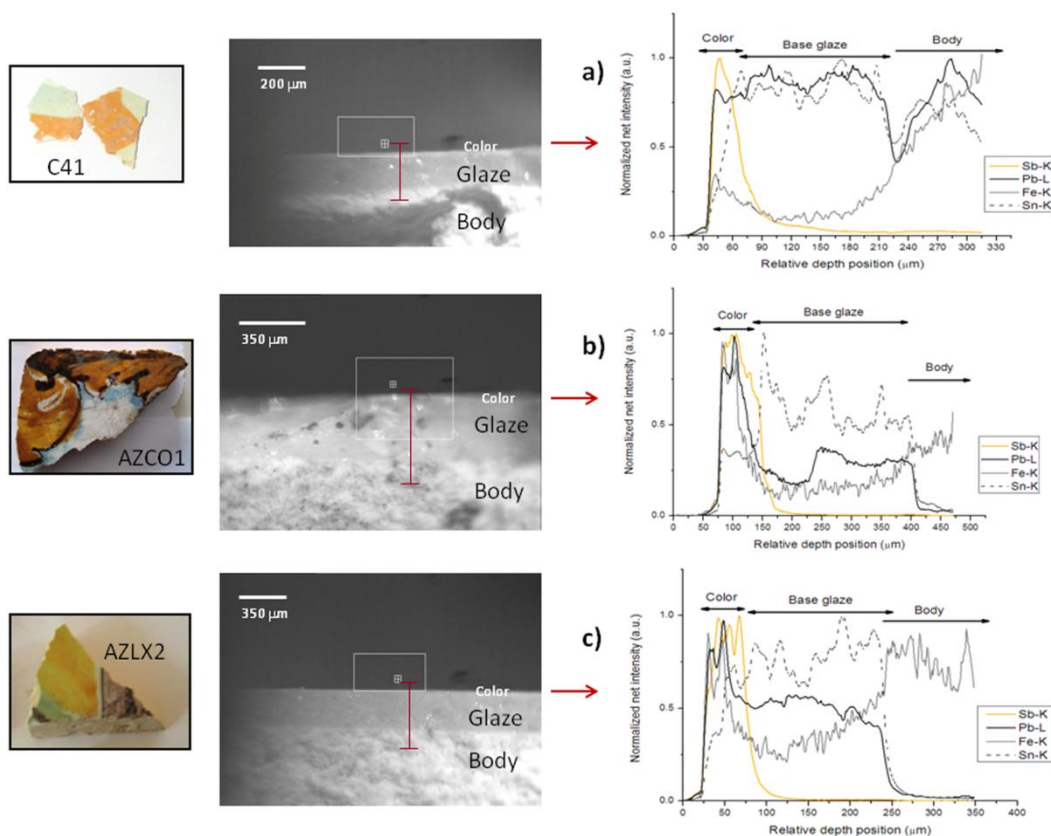


Figure 7.25 Elemental profiles from cross-section scans of two samples from Coimbra C41 (a) and AZCO1 (b) and one sample from Lisbon AZLX2 (c)

7.2.4 Elemental mappings with a Color X-ray Camera (CXC)

For these measurements samples with a broad range of surface decorations were chosen in order to obtain a bigger elemental variety on these mappings. The CXC with the 1:1 polycapillary optic and the DMM with 20 keV were used to record these images. In order to get good statistics the measuring time for the mappings was one hour.

In figure 7.26 the elemental mappings of the four tile samples AZCO3 (a), AZCO2 (b), AZLX9 (c) and AZLX2 (d) are shown. To display the mappings each element was assigned a different color as indicated next to the images.

The samples from Coimbra (figure 7.26a and 7.26b) have a green base decoration together with purple motifs on top of it which explains the abundant presence of Cu and Mn. The dark green color of sample AZCO3 is caused by a higher concentration of the green pigment which becomes apparent by a much stronger Cu signal than in sample AZCO2.

From sample AZLX9 (figure 7.26c) two areas were measured, the first containing green and purple and the second including yellow and purple motifs. The CXC mapping of the first

area shows that the green color actually is a mixture of green (Cu) and blue pigments (Co) while in the second area the purple pigment (Mn) is applied over the yellow one (Sb).

At last an elemental mapping of sample AZLX2 (figure 7.26d) shows the distribution of Sb from the yellow pigment (plotted in green for a better contrast) and the Mn from the dark purple line and the light purple area. Notice that even if over painted with yellow and purple the homogeneous distribution of Pb - characteristic for the glaze and the white color – is clearly to see.

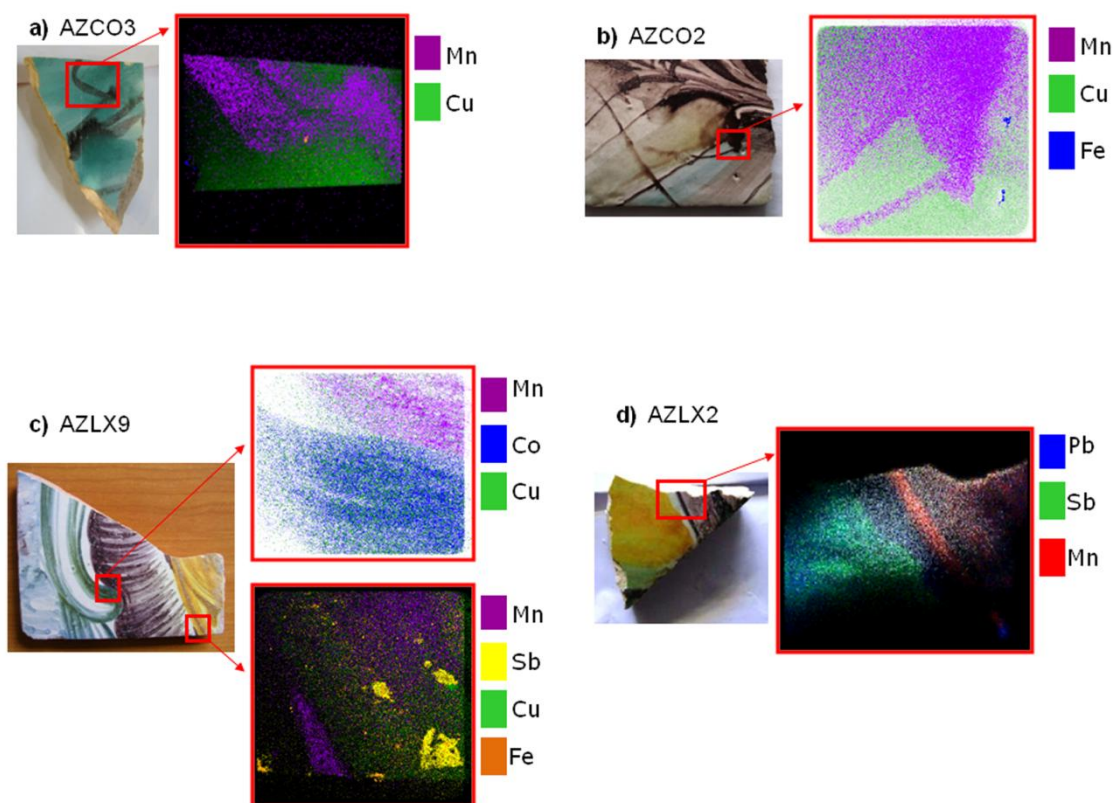


Figure 7.26 Elemental mappings performed with the Color X-ray Camera (CXC) on two samples from Coimbra AZCO3 (a) and AZCO2 (b) and two samples from Lisbon AZLX9 (c) and AZLX2 (d).

7.2.5 Conclusions

The samples used for this investigation were chosen to be representative of each type of ceramics as well as of the two centers of production. The most important conclusion with-drawn from this work is the usefulness of this method, for the investigation of this type of cultural heritage objects; since cross-section scans with high lateral resolution (1 μm) revealed features and properties of the samples which are not accessible by other techniques.

The difference between faiences and tiles is in the thickness of the glaze, which for faiences is only up to 180 μm , while for tiles it is up to 400 μm .

The major difference between the tiles from the two production centers is that the pigment layer is thicker in the tiles from Coimbra, while the intake of the pigment throughout the glaze is higher in the tile samples from Lisbon.

Other features like the broader glaze/body interface in the tiles from Lisbon may be the result of a more pronounced chemical exchange between some elements from the glaze and from the body than in the samples from Coimbra. The fact that the glazes show defects like voids or cracks lead to the assumption that the glaze has not undergone a previous firing process before been applied onto the bisque (fired ceramic body) but was applied in raw. This theory is sustained by the observed chemical exchange between Pb and Fe at the glaze/body interface. This exchange occurs during the firing process, where the dissolved lead compounds of the glaze are dragged into the ceramic body due to the high water absorbance of the bisque. The smoother exchange in the samples from Lisbon may lead to the conclusion that these samples were fired at higher temperatures which also could explain the fact that the pigment intake in the sample from Lisbon is higher than in the samples from Coimbra.

The elemental mappings made with the CXC, show the distribution of the elements, which characterize the color or the glaze and also reveal that some of the motifs are applied on top of other colors, as to observe e.g. in figure 7.26a.

8 Conclusions and Outlook

Compound Refractive Lenses have, compared to other X-ray focusing devices, the big advantage that the focal distance can be adjusted by aligning different numbers of single lens elements. Depending on the photon energy and the desired aperture of the lens, the focal distance can be chosen from some centimeters until some meters. This wide range and their simple design and alignment allow adapting the CRL's to most of the existing setups at synchrotron beamlines which were not initially designed for micro focus applications. The only requirements for the use of these lenses are a parallel and monochromatic ($\frac{\Delta E}{E} \leq 10^{-3}$) beam. Due to the circumstances at synchrotron beamlines where the source to sample distance is usually in the range of several tens of meters and the lens apertures are in the range of less than a millimeter the beam can be seen as parallel and an energy bandwidth of less than 10^{-3} can be reached e.g. by a crystal monochromator.

In the previous chapters the results of using the CRL outside the specified parameters are shown. A systematic investigation of the influences of a broad bandwidth multilayer monochromator, a prefocused (therefore divergent) beam as well as the usability of the CRL's for X-ray absorption spectroscopy (XAS) measurements was conducted.

For a complete characterization of the CRL the nominal parameters like beam size and focal distance were also measured. While the calculated and measured spot sizes are in good agreement, the values for the focal distance showed quite big differences especially for the lenses with smaller apertures as shown in table 6.3. The origin of this discrepancy is not known now, but will be further investigated. The measurements at the present lenses will be repeated to approve or disprove the former obtained values and in case they are approved, measurements on other lenses will be carried out to distinguish if the discrepancies are from the production of this lens or a general problem.

High resolution scans of bigger areas are very time consuming and therefore higher primary flux is desired which can be achieved by using a multilayer instead of a crystal monochromator. Using the DMM with an energy bandwidth in the order of 10^{-2} the flux at the *BAMline* is about 100 times higher than with the DCM and bending the second multilayer to parallelize the beam in the vertical plane further increases the flux on the sample. This about 200 times higher photon flux leads to significantly shorter measuring times but also to an increase of the spot size to $1.6 \mu\text{m} \times 1.5 \mu\text{m}$ (FWHM).

An important point of this work was to examine the usability of the CRL's to conduct XAS measurements. The investigation showed that only minor changes of the lens parameters occur in the XANES energy region (± 100 eV) while for the EXAFS region the changes are significant (see Chapter 6.4). Next to spot size and focal distance also the absorption within the lenses changes when tuning the energy of the primary beam, leading for standard normalization of XAS spectra (with pre- and post-edge line) to an overestimation in the XANES region. XAS measurements on different standard materials with and without lens showed that this does not affect the features of the XANES spectra and can be corrected easily.

Summing up, the studies showed that it is possible to conduct XANES measurements without adjusting the distance between sample and lens and even without taking into account the change of the absorption of the lens as long as the investigated structures are homogeneous over an area of about two times the nominal beam size. For samples smaller than the spot XANES analysis is still possible, but reference materials with well known sizes smaller than 1 μm have to be produced and measured.

For EXAFS measurements the absorption of the lens has to be taken into account and the distance between sample and CRL has to be adjusted simultaneously to the energy scan. While the absorption correction is quite easy, the correction of the focal distance is a technical challenge, since both sample and detector as a unit or the lens have to be moved precisely along the beam. For particles with a size in the order of micrometers and a beam of comparable size with a Gaussian energy distribution, it is obvious that already minor inaccuracies in the setup could provoke stronger changes than the actual EXAFS signal. If these problems are solved, EXAFS measurements with a resolution of about 2 μm should be possible. Nevertheless restrictions like a minimal size for the analyzed structure of several μm should be made to ensure a certain accuracy of the results. On the other hand for samples with this size capillary optics with spot sizes in the order of 10 μm and a much lower energy dependence might be used to conduct such measurements.

Investigation of a solar grade silicon wafer showed that elements with bulk concentrations in the order of one $\text{ng}\cdot\text{g}^{-1}$ can be detected by synchrotron micro X-ray fluorescence analysis, if they form precipitates within the solar cell. Taking Cu as an example it is shown that the instrumental limit of detection is in the range of 5 fg ($\sim 5 \cdot 10^7$ atoms). Furthermore, it was shown that the depth of the precipitates within the solar cell can be estimated by the ratio of the emitted fluorescence lines (K_α/K_β) which leads to a better estimation of the cluster size and the spacing between them. These values are important to determine the influence of the

impurities on the minority carrier diffusion length in the area and the solar cell efficiency in general. Furthermore, μ -XANES measurements revealed that different Cu-compounds (most likely Cu_3Si and Cu_2O) are present in the solar cell. The knowledge of distribution and species are essential for a successful "defect engineering" with the aim of raising the solar cell efficiency while using cheaper but therefore dirtier feedstock material.

Another application was the investigation of Portuguese glazed ceramic fragments showing the usefulness of measurements with high resolution when studying this type of cultural heritage objects. Elemental profiles from cross-section scans with a $1\ \mu\text{m}$ lateral resolution on several objects revealed general features for the different kinds of ceramics and the production centers Lisbon and Coimbra. The major difference between the two kinds of ceramics is the thickness of the glaze, which is up to $200\ \mu\text{m}$ and up to $400\ \mu\text{m}$ for faiences and tiles respectively. General differences between the two compared production centers are the broader maximum of the signal from the characteristic element of the pigment in the samples from Coimbra and the slightly higher intake of the pigment throughout the glaze as well as a broader glaze/body interface in the samples from Lisbon. These measurements are only a small contribution to the study of these objects but together with previous investigations they provided information about the manufacturing techniques, the raw materials and the mixtures which were used to produce these pieces.

Bibliography

1. Moseley, H.G.J., *The high-frequency spectra of the elements*. Philosophical Magazine, 1913. **26**(156): p. 1024-1034.
2. Moseley, H.G.J., *The high-frequency spectra of the elements. Part II*. Philosophical Magazine, 1914. **27**(157-62): p. 703-713.
3. Smith, J.V., *Synchrotron X-ray sources - Instrumental characteristics - New applications in microanalysis, tomography, absorption-spectroscopy and diffraction*. Analyst, 1995. **120**(5): p. 1231-1245.
4. Duke, P.J., *Synchrotron radiation: Production and properties*. 2000: Oxford University Press.
5. Snigirev, A. and I. Snigireva, *High energy X-ray micro-optics*. Comptes Rendus Physique, 2008. **9**(5-6): p. 507-516.
6. Ice, G.E., J.D. Budai, and J.W.L. Pang, *The race to X-ray microbeam and nanobeam science*. Science, 2011. **334**(6060): p. 1234-1239.
7. Guilherme, A., G. Buzanich, and M.L. Carvalho, *Focusing systems for the generation of X-ray micro beam: An overview*. Spectrochimica Acta Part B: Atomic Spectroscopy, 2012. **77**(0): p. 1-8.
8. Riesemeier, H., et al., *Layout and first XRF applications of the BAMline at BESSY II*. X-ray Spectrometry, 2005. **34**(2): p. 160-163.
9. Borovikov, V.M., et al., *Superconducting 7T wave length shifter for BESSY-II*. Nuclear Instruments & Methods in Physics Research Section a-Accelerators Spectrometers Detectors and Associated Equipment, 2001. **467**: p. 181-184.
10. Strub, E., et al., *Measurements with compound refractive lenses at the "BAMline"*. Nuclear Instruments & Methods in Physics Research Section B-Beam Interactions with Materials and Atoms, 2008. **266**(10): p. 2165-2168.
11. Liénard, A., *The electric and magnetic field produced by an electric charge concentrated at a point and in arbitrary motion*. L'Éclairage Électrique, 1898. **16**: p. 5.
12. Schott, G.A., *Electromagnetic Radiation and the mechanical reactions arising from it*. Cambridge University Press, Cambridge, 1912.
13. Kerst, D.W., *Acceleration of electrons by magnetic induction*. Physical Review, 1940. **58**(9): p. 841-841.
14. Kerst, D.W., *The acceleration of electrons by magnetic induction*. Physical Review, 1941. **60**(1): p. 47-53.
15. Iwanenko, D. and I. Pomeranchuk, *On the maximal energy attainable in a betatron*. Physical Review, 1944. **65**(11/12): p. 343-343.
16. Westendorp, W.F. and E.E. Charlton, *A 100-million volt induction electron accelerator*. Journal of Applied Physics, 1945. **16**(10): p. 581-593.
17. Blewett, J.P., *Radiation losses in the induction electron accelerator*. Physical Review, 1946. **69**(3-4): p. 87-95.

18. Schwinger, J., *Electron radiation in high energy accelerators*. Physical Review, 1946. **70**(9-10): p. 798-799.
19. Schwinger, J., *On the classical radiation of accelerated electrons*. Physical Review, 1949. **75**(12): p. 1912-1925.
20. McMillan, E.M., *The Synchrotron - A proposed high energy particle accelerator*. Physical Review, 1945. **68**(5-6): p. 143-144.
21. McMillan, E.M., *Radiation from a group of electrons moving in a circular orbit*. Physical Review, 1945. **68**(5-6): p. 144-145.
22. Elder, F.R., et al., *A 70-MeV Synchrotron*. Journal of Applied Physics, 1947. **18**(9): p. 810-818.
23. Elder, F.R., R.V. Langmuir, and H.C. Pollock, *Radiation from electrons accelerated in a Synchrotron*. Physical Review, 1948. **74**(1): p. 52-56.
24. Corson, D.R., *Radiation by electrons in large orbits*. Physical Review, 1953. **90**(5): p. 748-752.
25. Ado, I.M. and P.A. Cherenkov, *Energy distribution of incoherent radiation from synchrotron electrons*. Soviet Physics Doklady, 1956. **1**: p. 517-519.
26. Tomboulian, D.H. and P.L. Hartman, *Spectral and angular distribution of ultraviolet radiation from the 300-MeV Cornell Synchrotron*. Physical Review, 1956. **102**(6): p. 1423-1447.
27. Lynch, D., *Tantalus, a 240MeV Dedicated Source of Synchrotron Radiation, 1968-1986*. Journal of Synchrotron Radiation, 1997. **4**(6): p. 334-343.
28. Chasman, R., G.K. Green, and E.M. Rowe, *Preliminary design of a dedicated synchrotron radiation facility*. Ieee Transactions on Nuclear Science, 1975. **NS22**(3): p. 1765-1767.
29. Pollock, H.C., *The discovery of Synchrotron Radiation*. American Journal of Physics, 1982. **51**(3): p. 278-280.
30. Koch, E., *Handbook on Synchrotron Radiation* 1983: North-Holland Publishing Company, Amsterdam.
31. Wiedemann, H., *Synchrotron Radiation*. Advanced Texts in Physics. 2003, Berlin: Springer.
32. Bastian, H., *Principle of Wiggler and Undulator devices*, 2006, Bastieh at de.wikipedia [GFDL (<http://www.gnu.org/copyleft/fdl.html>)]: <http://commons.wikimedia.org/wiki/File%3AUndulator-prinzip.svg>.
33. http://hasylab.desy.de/e70/e6129/e4242/e4370/felbasics_eng.pdf, Retrieved on 13th July 2012.
34. Snigireva, I. and A. Snigirev, *X-ray microanalytical techniques based on synchrotron radiation*. Journal of Environmental Monitoring, 2006. **8**(1): p. 33-42.
35. Bergemann, C., H. Keymeulen, and J.F. van der Veen, *Focusing X-ray beams to nanometer dimensions*. Physical Review Letters, 2003. **91**(20): p. 2048011-4.
36. Schroer, C.G., et al., *Nanofocusing parabolic refractive X-ray lenses*. Applied Physics Letters, 2003. **82**(9): p. 1485-1487.
37. <http://X-ray-optics.de/>, Retrieved on 13th March 2012.

38. Kirkpatrick, P. and A.V. Baez, *Formation of optical images by X-rays*. J. Opt. Soc. Am., 1948. **38**(9): p. 766-773.
39. http://www.xrayoptic.ru/e_kumakhov_art_1.htm, Retrieved on 13th March 2012.
40. Bragg, W.H. and W.L. Bragg, *The reflection of X-rays by crystals*. Proceedings of the Royal Society of London Series a-Containing Papers of a Mathematical and Physical Character, 1913. **88**(604): p. 428-428.
41. Suehiro, S., H. Miyaji, and H. Hayashi, *Refractive lens for X-ray focus*. Nature, 1991. **352**(6334): p. 385-386.
42. Snigirev, A., et al., *A compound refractive lens for focusing high-energy X-rays*. Nature, 1996. **384**(6604): p. 49-51.
43. Lengeler, B., et al., *Parabolic refractive X-ray lenses: a breakthrough in X-ray optics*. Nuclear Instruments & Methods in Physics Research Section a-Accelerators Spectrometers Detectors and Associated Equipment, 2001. **467**: p. 944-950.
44. Snigirev, A., et al., *Focusing High-Energy X-rays by Compound Refractive Lenses*. Appl. Opt., 1998. **37**(4): p. 653-662.
45. Dudchik, Y.I. and N.N. Kolchevsky, *A microcapillary lens for X-rays*. Nuclear Instruments & Methods in Physics Research Section a-Accelerators Spectrometers Detectors and Associated Equipment, 1999. **421**(1-2): p. 361-364.
46. Cederstrom, B., et al., *Focusing hard X-rays with old LPs*. Nature, 2000. **404**(6781): p. 951-951.
47. Nillius, P., et al., *Large-aperture focusing of high-energy X-rays with a rolled polyimide film*. Optics Letters, 2011. **36**(4): p. 555-557.
48. <http://www.zoneplates.com/zone%20plate.html>, Retrieved on 28th June 2012.
49. Röntgen, W.C., *Ueber eine neue Art von Strahlen*, in *Aus den Sitzungsberichten der Würzburger physik.-med. Gesellschaft*. . 1895, Stahel'sche Verlagsanstalt - Königlicher Hof- und Universitäts-Verlag: Würzburg.
50. Barkla, C.G., *Note on experiments to detect refraction of X-rays*. Philosophical Magazine, 1916. **31**(181-86): p. 257-260.
51. James, R.W., *The optical principles of the diffraction of X-rays*. . 1954: G. Bell.
52. Protopopov, V.V. and K.A. Valiev, *Theory of an ideal compound X-ray lens*. Optics Communications, 1998. **151**(4-6): p. 297-312.
53. Elleaume, P., *Optimization of compound refractive lenses for X-rays*. Nuclear Instruments and Methods in Physics Research Section A: Accelerators, Spectrometers, Detectors and Associated Equipment, 1998. **412**(2-3): p. 483-506.
54. Pantell, R.H., et al., *Characteristics of the thick, compound refractive lens*. Applied Optics, 2003. **42**(4): p. 719-723.
55. Kohn, V.G., *On the theory of X-ray refractive optics: Exact solution for a parabolic medium*. Jetp Letters, 2002. **76**(10): p. 600-603.
56. Born, M., E. Wolf, and A.B. Bhatia, *Principles of Optics: Electromagnetic Theory of Propagation, Interference and Diffraction of Light*. 1999: Cambridge University Press.
57. Lengeler, B., et al., *Imaging by parabolic refractive lenses in the hard X-ray range*. Journal of Synchrotron Radiation, 1999. **6**: p. 1153-1167.

58. Lipson, A., S.G. Lipson, and H. Lipson, *Optical physics*. 4th ed ed. 2011, Cambridge ; New York: Cambridge University Press.
59. Vyvenko, O.F., et al., *X-ray beam induced current - a synchrotron radiation based technique for the in situ analysis of recombination properties and chemical nature of metal clusters in silicon*. *Journal of Applied Physics*, 2002. **91**(6): p. 3614-3617.
60. Lengeler, B., *Extended X-ray absorption fine structure*. *Neutron and X-ray Spectroscopy*, ed. E.G. F.Hippert, J.L. Hodeau, E. Lelièvre-Berna and J.R. Regnard; . 2006: Springer.
61. Baumgartel, H., *X-ray Absorption - Principles, Applications, Techniques of EXAFS, SEXAFS and XANES*. *Nachrichten aus Chemie, Technik und Laboratorium*, ed. D.K.u.R. Prins. Vol. 36. 1988, Chichester: Wiley-VCH Verlag GmbH & Co. 650.
62. Rehr, J.J. and R.C. Albers, *Theoretical approaches to X-ray absorption fine structure*. *Reviews of Modern Physics*, 2000. **72**(3): p. 621-654.
63. Yano, J. and V.K. Yachandra, *X-ray absorption spectroscopy*. *Photosynthesis Research*, 2009. **102**(2-3): p. 241-254.
64. Bouguer, P., *Essai d'optique sur la gradation de la lumiere* 1729, Paris: Chez Claude Jombert.
65. Lambert, J.H., *Photometria sive de mensura et gradibus luminis, colorum et umbrae* 1760, Augsburg, Germany: Eberhardt Klett.
66. Beer, *Bestimmung der Absorption des rothen Lichts in farbigen Flüssigkeiten*. *Annalen der Physik*, 1852. **162**(5): p. 78-88.
67. Victoreen, J.A., *The Calculation of X-ray Mass Absorption Coefficients*. *Journal of Applied Physics*, 1949. **20**(12): p. 1141-1147.
68. Chaboy, J., A. Marcelli, and T.A. Tyson, *Influence of double-electron transitions on the EXAFS L-edges of rare-earth systems*. *Physical Review B*, 1994. **49**(17): p. 11652-11661.
69. D'Angelo, P., H.F. Nolting, and N.V. Pavel, *Evidence for multielectron resonances at the Sr K edge*. *Physical Review A*, 1996. **53**(2): p. 798-805.
70. Wende, H., et al., *Evidence for photoelectron backscattering by interstitial charge densities*. *Journal of Physics-Condensed Matter*, 1997. **9**(31): p. 427-433.
71. Wende, H. and K. Baberschke, *Atomic EXAFS: evidence for photoelectron backscattering by interstitial charge densities*. *Journal of Electron Spectroscopy and Related Phenomena*, 1999. **101**: p. 821-826.
72. Yamauchi, K., et al., *Single-nanometer focusing of hard X-rays by Kirkpatrick-Baez mirrors*. *Journal of Physics-Condensed Matter*, 2011. **23**(39): p. 3942061-9.
73. Kitajima, N., et al., *Observation of arsenic transfer in leaf tissue of hyperaccumulator fern by utilizing synchrotron radiation micro-XRF imaging*. *Chemistry Letters*, 2008. **37**(1): p. 32-33.
74. Tsuji, K., T. Yonehara, and K. Nakano, *Application of confocal 3D micro-XRF for solid/liquid interface analysis*. *Analytical Sciences*, 2008. **24**(1): p. 99-103.
75. Vespa, M., et al., *Speciation of heavy metals in cement-stabilized waste forms: A micro-spectroscopic study*. *Journal of Geochemical Exploration*, 2006. **88**(1-3): p. 77-80.

76. Curti, E., D. Grolimund, and C.N. Borca, *A micro-XAS/XRF and thermodynamic study of Ce-III/IV speciation after long-term aqueous alteration of simulated nuclear waste glass: Relevance for predicting Pu behavior?* Applied Geochemistry, 2012. **27**(1): p. 56-63.
77. Ortega, R., *Direct speciation analysis of inorganic elements in single cells using X-ray absorption spectroscopy.* Journal of Analytical Atomic Spectrometry, 2011. **26**(1): p. 23-29.
78. Martinetto, P., et al., *Synchrotron X-ray micro-beam studies of ancient Egyptian make-up.* Nuclear Instruments and Methods in Physics Research Section B: Beam Interactions with Materials and Atoms, 2001. **181**(1-4): p. 744-748.
79. Scordari, F., et al., *XRD, micro-XANES, EMPA, and SIMS investigation on phlogopite single crystals from Mt. Vulture (Italy).* American Mineralogist, 2010. **95**(11-12): p. 1657-1670.
80. Mongkhonsin, B., et al., *Distribution and speciation of chromium accumulated in Gynura pseudochina (L.) DC.* Environmental and Experimental Botany, 2011. **74**: p. 56-64.
81. Heald, S.M., et al., *The PNC/XOR X-ray microprobe station at APS sector 20.* Nuclear Instruments & Methods in Physics Research Section a-Accelerators Spectrometers Detectors and Associated Equipment, 2007. **582**(1): p. 215-217.
82. Borca, C.N., et al., *The microXAS beamline at the swiss light source: Towards nano-scale imaging.* Journal of Physics: Conference Series, 2009. **186**(1): p. 012003.
83. Flank, A.M., et al., *LUCIA, a microfocuss soft XAS beamline.* Nuclear Instruments & Methods in Physics Research Section B-Beam Interactions with Materials and Atoms, 2006. **246**(1): p. 269-274.
84. Pascarelli, S., et al., *Energy-dispersive absorption spectroscopy for hard-X-ray micro-XAS applications.* Journal of Synchrotron Radiation, 2006. **13**: p. 351-358.
85. http://www.helmholtz-berlin.de/angebote/arbeiten-lernen/info/beschleunigerphysik-fuer-anfaenger/index_en.html, Retrieved on 24th July 2012.
86. Goerner, W., et al., *BAMline: the first hard X-ray beamline at BESSY II.* Nuclear Instruments & Methods in Physics Research Section a-Accelerators Spectrometers Detectors and Associated Equipment, 2001. **467**: p. 703-706.
87. Eichelbaum, M., et al., *On the chemistry of gold in silicate glasses: Studies on a nonthermally activated growth of gold nanoparticles.* Angewandte Chemie-International Edition, 2005. **44**(48): p. 7905-7909.
88. Strub, E., et al., *Determination of Cr(VI) in wood specimen: A XANES study at the CrK edge.* Nuclear Instruments & Methods in Physics Research Section B-Beam Interactions with Materials and Atoms, 2008. **266**(10): p. 2405-2407.
89. Müller, B.R. and M.P. Hentschel, *Synchrotron radiation refraction topography for characterization of lightweight materials.* X-ray Spectrometry, 2004. **33**(6): p. 402-406.
90. Goerner, W., et al., *Non-destructive investigation of composition, chemical properties and structure of materials by synchrotron radiation.* Insight - Non-Destructive Testing and Condition Monitoring, 2006. **48**(9): p. 540-544.
91. Krumrey, M., et al., *Calibration and characterization of semiconductor X-ray detectors with synchrotron radiation.* Nuclear Instruments and Methods in Physics

- Research Section A: Accelerators, Spectrometers, Detectors and Associated Equipment, 2006. **568**(1): p. 364-368.
92. Büermann, L., et al., *Measurement of the X-ray mass energy-absorption coefficient of air using 3 keV to 10 keV synchrotron radiation*. Physics in Medicine and Biology, 2006. **51**(20): p. 5125.
93. Zehbe, R., et al., *Imaging of articular cartilage - Data matching using X-ray tomography, SEM, FIB slicing and conventional histology*. Micron, 2012. **43**(10): p. 1060-7.
94. Zabler, S., *X-ray imaging by partially coherent synchrotron light: Application to metallic alloys, tooth dentin and natural rock*, 2007, Fakultät III - Prozesswissenschaften; Technische Universität Berlin: Berlin. p. 129-137.
95. Rack, A., et al., *High resolution synchrotron-based radiography and tomography using hard X-rays at the BAMline (BESSY II)*. Nuclear Instruments & Methods in Physics Research Section a-Accelerators Spectrometers Detectors and Associated Equipment, 2008. **586**(2): p. 327-344.
96. Weitkamp, T., C. Raven, and A.A. Snigirev, *Imaging and microtomography facility at the ESRF beamline ID 22*. 1999: p. 311-317.
97. <http://www.pco.de/categories/sensitive-cameras/pco4000/>, Retrieved on 27th July 2012.
98. Meidinger, N., et al., *CCD detectors for spectroscopy and imaging of X-rays with the eROSITA space telescope*. 2009: p. 743502-743502.
99. Bjeoumikhov, A., et al., *New generation of polycapillary lenses: manufacture and applications*. X-ray Spectrometry, 2003. **32**(3): p. 172-178.
100. Scharf, O., et al., *Compact pnCCD-based X-ray camera with high spatial and energy resolution: A Color X-ray Camera*. Analytical Chemistry, 2011. **83**(7): p. 2532-2538.
101. Ordavo, I., et al., *A new pnCCD-based color X-ray camera for fast spatial and energy-resolved measurements*. Nuclear Instruments & Methods in Physics Research Section a-Accelerators Spectrometers Detectors and Associated Equipment, 2011. **654**(1): p. 250-257.
102. Nazmov, V., et al., *Fabrication and preliminary testing of X-ray lenses in thick SU-8 resist layers*. Microsystem Technologies, 2004. **10**(10): p. 716-721.
103. Nazmov, V., et al. *Refractive lenses fabricated by deep SR lithography and LIGA technology for X-ray energies from 1 keV to 1 MeV*. in 8. international conference on synchrotron radiation instrumentation. 2004. San Francisco, CA (United States): AIP Conference Proceedings.
104. Nazmov, V., et al., *X-ray lenses fabricated by LIGA technology*, in *Synchrotron Radiation Instrumentation, Pts 1 and 2*, J.Y.R.S. Choi, Editor. 2007. p. 770-773.
105. Nazmov, V., et al., *Parabolic crossed planar polymeric X-ray lenses*. Journal of Micromechanics and Microengineering, 2011. **21**(1).
106. Buzanich, G., et al., *Micro-X-ray absorption spectroscopy with compound refractive lenses*. Journal of Analytical Atomic Spectrometry, 2012.
107. Ravel, B. and M. Newville, *ATHENA, ARTEMIS, HEPHAESTUS: data analysis for X-ray absorption spectroscopy using IFEFFIT*. Journal of Synchrotron Radiation, 2005. **12**: p. 537-541.

108. Buzanich, G., et al., *Impurities in multicrystalline silicon wafers for solar cells detected by synchrotron micro-beam X-ray fluorescence analysis*. Journal of Analytical Atomic Spectrometry, 2012.
109. Guilherme, A., et al., *Synchrotron micro-XRF with Compound Refractive Lenses (CRLs) for tracing key elements on Portuguese glazed ceramics*. Journal of Analytical Atomic Spectrometry, 2012. **27**(6): p. 966-974.
110. Khouzam, R.B., R. Lobinski, and P. Pohl, *Multi-element analysis of bread, cheese, fruit and vegetables by double-focusing sector-field inductively coupled plasma mass spectrometry*. Analytical Methods, 2011. **3**(9): p. 2115-2120.
111. Fabry, L., et al., *Trace-analytical methods for monitoring contaminations in semiconductor-grade Si manufacturing*. Fresenius' Journal of Analytical Chemistry, 1994. **349**(4): p. 260-271.
112. Hsiao, P.K., S.J. Jiang, and A.C. Sahayam, *Determination of trace elements in silicon powder using slurry sampling electrothermal vaporization inductively coupled plasma mass spectrometry*. Journal of Analytical Atomic Spectrometry, 2011. **26**(3): p. 586-592.
113. Kempenaers, L., L. Vincze, and K. Janssens, *The use of synchrotron micro-XRF for characterization of the micro-heterogeneity of heavy metals in low-Z reference materials*. Spectrochimica Acta Part B: Atomic Spectroscopy, 2000. **55**(6): p. 651-669.
114. Guilherme, A., et al., *X-ray fluorescence (conventional and 3D) and scanning electron microscopy for the investigation of Portuguese polychrome glazed ceramics: Advances in the knowledge of the manufacturing techniques*. Spectrochimica Acta Part B-Atomic Spectroscopy, 2011. **66**(5): p. 297-307.
115. Grolimund, D., et al., *Shedding new light on historical metal samples using micro-focused synchrotron X-ray fluorescence and spectroscopy*. Spectrochimica Acta Part B: Atomic Spectroscopy, 2004. **59**(10-11): p. 1627-1635.
116. Borsato, A., et al., *Trace element distribution in annual stalagmite laminae mapped by micrometer-resolution X-ray fluorescence: Implications for incorporation of environmentally significant species*. Geochimica Et Cosmochimica Acta, 2007. **71**(6): p. 1494-1512.
117. Thieme, J., et al., *Microscopy and spectroscopy with X-rays for studies in the environmental sciences*. Mineralogical Magazine, 2008. **72**(1): p. 211-216.
118. Bontempi, E., et al., *Micro X-ray fluorescence as a potential technique to monitor in-situ air pollution*. Microchimica Acta, 2008. **161**(3-4): p. 301-305.
119. Petibois, C., *Imaging methods for elemental, chemical, molecular, and morphological analyses of single cells*. Analytical and Bioanalytical Chemistry, 2010. **397**(6): p. 2051-2065.
120. Kemner, K.M., et al., *Elemental and redox analysis of single bacterial cells by X-ray microbeam analysis*. Science, 2004. **306**(5696): p. 686-687.
121. Farquharson, M.J., et al., *The localisation and micro-mapping of copper and other trace elements in breast tumours using a synchrotron micro-XRF system*. Applied Radiation and Isotopes, 2007. **65**(2): p. 183-188.
122. Nakano, K., et al., *Depth elemental imaging of forensic samples by confocal micro-XRF method*. Analytical Chemistry, 2011. **83**(9): p. 3477-3483.

123. Zoeger, N., et al., *Determination of the elemental distribution in human joint bones by SR micro XRF*. X-ray Spectrometry, 2008. **37**(1): p. 3-11.
124. Shockley, W. and H.J. Queisser, *Detailed Balance Limit of Efficiency of p-n Junction Solar Cells*. Journal of Applied Physics, 1961. **32**(3): p. 510-519.
125. <http://www.iec.ch/>, Retrieved on 30th July 2012.
126. Istratov, A.A., et al., *Control of metal impurities in "dirty" multicrystalline silicon for solar cells*. Materials Science and Engineering B-Solid State Materials for Advanced Technology, 2006. **134**(2-3): p. 282-286.
127. McHugo, S.A., et al., *Synchrotron-based impurity mapping*. Journal of Crystal Growth, 2000. **210**(1-3): p. 395-400.
128. Trushin, M., et al., *XBIC/ μ -XRF/ μ -XAS analysis of metals precipitation in block-cast solar silicon*. Nuclear Instruments & Methods in Physics Research Section B-Beam Interactions with Materials and Atoms, 2010. **268**(3-4): p. 254-258.
129. Vyvenko, O.F., et al., *Application of synchrotron-radiation-based X-ray microprobe techniques for the analysis of recombination activity of metals precipitated at Si/SiGe misfit dislocations*. Journal of Physics-Condensed Matter, 2002. **14**(48): p. 13079-13086.
130. Buonassisi, T., et al., *Engineering metal-impurity nanodefects for low-cost solar cells*. Nature Materials, 2005. **4**(9): p. 676-679.
131. Macdonald, D., et al., *Scanning X-ray fluorescence microspectroscopy of metallic impurities in solar-grade silicon*. Physica Status Solidi a-Applications and Materials Science, 2010. **207**(8): p. 1807-1810.
132. Ryan, C.G., et al., *The new Maia detector system: Methods for high definition trace element imaging of natural material*. AIP Conference Proceedings, 2010. **1221**(1): p. 9-17.
133. Trushin, M., et al., *Combined XBIC/ μ -XRF/ μ -XAS/DLTS investigation of chemical character and electrical properties of Cu and Ni precipitates in silicon*. physica status solidi (c), 2009. **6**(8): p. 1868-1873.
134. Buonassisi, T., et al., *Analysis of copper-rich precipitates in silicon: Chemical state, gettering, and impact on multicrystalline silicon solar cell material*. Journal of Applied Physics, 2005. **97**(6): p. 063503.
135. Guilherme, A., J. Coroado, and M.L. Carvalho, *Chemical and mineralogical characterization on glazes of ceramics from Coimbra (Portugal) from the sixteenth to nineteenth centuries*. Analytical and Bioanalytical Chemistry, 2009. **395**(7): p. 2051-2059.
136. Guilherme, A., et al., *Micro energy dispersive X-ray fluorescence analysis of polychrome lead-glazed Portuguese faiences*. Spectrochimica Acta Part B-Atomic Spectroscopy, 2010. **65**(4): p. 328-333.
137. Sole, V.A., et al., *A multiplatform code for the analysis of energy-dispersive X-ray fluorescence spectra*. Spectrochimica Acta Part B-Atomic Spectroscopy, 2007. **62**(1): p. 63-68.

Appendix

CURRICULUM VITAE

Name: Günter Buzanich
Academic title: Dipl.-Ing.
Date of birth: 1973-04-13
Place of birth: Vienna, Austria
Personal status: married
Nationality: Austria
Private address: 2732 Zweiersdorf, Hubertusgasse 14, Austria
Email: gb@tos.at

Education

since 2009: PhD study at the Vienna University of Technology

Thesis title: “*Characterization of Compound Refractive Lenses for synchrotron μ -XRF and μ -XAS and applications with high spatial resolution*”

Accomplished under supervision of Prof. Dr. Christina Strelí (Institute of Atomic and Subatomic Physics), in cooperation with the BAM - Federal Institute for Materials Research and Testing in Berlin, Germany under supervision of Dr. Heinrich Riesemeier

1995 - 2008: Study of Technical Physics at the Vienna University of Technology.

Diploma examination in January 2008

Thesis title: “*Portable XRF system with polycapillary optics and light element vacuum chamber for archeometric and other applications.*”

Accomplished under supervision of Prof. Dr. Wobrauschek (Institute of Atomic and Subatomic Physics), in cooperation with the IAEA’s Nuclear Sciences and Applications Laboratories in Seibersdorf, Austria.

1987 - 1992: Höhere Technische Bundeslehr- und Versuchsanstalt (HTBLuVA) für Maschinenbau (Higher technical education institute with emphasis on mechanical engineering) in Mödling, Austria

Professional activity:

2010 - 2012: BAM Federal Institute for Materials Research and Testing, Berlin, Germany
Division 1.3 - Structural analysis

Microanalysis (e.g. μ -XRF, μ -XANES) using X-ray optics (capillaries, CRL's) at the BAMline and μ -Spot Beamline at BESSY II

- polycrystalline silicon (metal impurities)
- art objects (e.g. ceramics)
- standard reference materials (BAM – SRM's)
- geological samples (e.g. oil shale)
- biological samples (e.g. nematodes and bone)

2009 - 2010: Brandenburgische Technische Universität, Cottbus, Germany
IHP/ BTU Joint Lab

XBIC, μ -XRF and μ -XANES analysis on metallic impurities in photovoltaic polycrystalline silicon at the Synchrotron source BESSY II in Berlin, Germany

2008 - 2009: Vienna University of Technology, Vienna Austria
Atomic Institute of the Austrian Universities

Design, assembly and start-up of a portable XRF system with special adaption to the requirements of the "Kunsthistorisches Museum Wien"

2000 - 2004: Wolfgang Denzel AG, Vienna, Austria
Department - new buildings and maintenance

- Supervision of building services
- Acquisition of technical and business-related equipment
- Awarding authority for modification of buildings and new construction

1995 - 2008: Various summer jobs/internships for practical training.

1993 - 1995: MAPLAN GmbH, Ternitz, Austria
Department - extrusion plants

- Design and construction of extrusion plants for synthetic materials and the customized attachments.
- Direction and supervision of purchase, production, quality assurance, assembling and start-up of the plants.

1992 - 1993: Federal armed forces (military service fully served)

Additional skills

Software: Windows, Office, Origin, IDL (Interactive Data Language)
Special programs for data analysis (e.g. AXIL, Athena)

Driving Licence: Category B (vehicles up to 3500kg)

List of Publications:

- Guilherme A., Buzanich G., Radtke M., Reinholz U., Coroado J., Dos Santos J.M.F., and Carvalho M.L., *Synchrotron micro-XRF with Compound Refractive Lenses (CRLs) for tracing key elements on Portuguese glazed ceramics*. Journal of Analytical Atomic Spectrometry, 2012. **27**(6): p. 966-974.
- Constantinescu B., Vasilescu A., Stan D., Radtke M., Reinholz U., Buzanich G., Ceccato D., and Oberlander-Tarnoveanu E., *Studies on archaeological gold items found on Romanian territory using X-Ray based analytical spectrometry*. Journal of Analytical Atomic Spectrometry, 2012.
- Buzanich G., Radtke M., Reinholz U., Riesemeier H., and Strelci C., *Micro-X-ray absorption spectroscopy with compound refractive lenses*. Journal of Analytical Atomic Spectrometry, 2012. **27**(10): p. 1803-1808.
- Guilherme A., Buzanich G., and Carvalho M.L., *Focusing systems for the generation of X-ray micro beam: An overview*. Spectrochimica Acta Part B: Atomic Spectroscopy, 2012. **77**(0): p. 1-8.
- Buzanich G., Radtke M., Reinholz U., Riesemeier H., Thunemann A.F., and Strelci C., *Impurities in multicrystalline silicon wafers for solar cells detected by synchrotron micro-beam X-ray fluorescence analysis*. Journal of Analytical Atomic Spectrometry, 2012. **27**(11): p. 1875-1881.
- Scharf O., Ihle S., Ordavo I., Arkadiev V., Bjeoumikhov A., Bjeoumikhova S., Buzanich G., Gubzhokov R., Gunther A., Hartmann R., Kuhbacher M., Lang M., Langhoff N., Liebel A., Radtke M., Reinholz U., Riesemeier H., Soltau H., Struder L., Thunemann A.F., and Wedell R., *Compact pnCCD-based X-ray camera with high spatial and energy resolution: A Color X-ray Camera*. Analytical Chemistry, 2011. **83**(7): p. 2532-2538.
- Grunewald C., Radtke M., Reinholz U., Buzanich G., and Riesemeier H., *SRXRF-measurements at non-planar objects: automatic determination of the angle of incidence of the exciting X-ray*. Journal of Analytical Atomic Spectrometry, 2011. **26**(5): p. 1088-1089.
- El-Hasan T., Szczerba W., Buzanich G., Radtke M., Riesemeier H., and Kersten M., *Cr(VI)/Cr(III) and As(V)/As(III) Ratio Assessments in Jordanian Spent Oil Shale Produced by Aerobic Combustion and Anaerobic Pyrolysis*. Environmental Science & Technology, 2011. **45**(22): p. 9799-9805.
- Ordavo I., Ihle S., Arkadiev V., Scharf O., Soltau H., Bjeoumikhov A., Bjeoumikhova S., Buzanich G., Gubzhokov R., Guenther A., Hartmann R., Holl P., Kimmel N., Kuehbacher M., Lang M., Langhoff N., Liebel A., Radtke M., Reinholz U., Riesemeier H., Schaller G., Schopper F., Strueder L., Thamm C., and Wedell R., *A new pnCCD-based color X-ray camera for fast spatial and energy-resolved measurements*. Nuclear Instruments & Methods in Physics Research Section a-Accelerators Spectrometers Detectors and Associated Equipment, 2011. **654**(1): p. 250-257.
- Buzanich G., Wobrauschek P., Strelci C., Markowicz A., Wegrzynek D., Chinea-Cano E., Griesser M., and Uhler K., *PART II (Portable ART analyzer) - development of a XRF spectrometer adapted for the study of artworks in the Kunsthistorisches Museum, Vienna*. X-Ray Spectrometry, 2010. **39**(2): p. 98-102.

Uhlir K., Griesser M., Buzanich G., Wobrauschek P., Strelci C., Wegrzynek D., Markowicz A., and China-Cano E., *Applications of a new portable (micro) XRF instrument having low-Z elements determination capability in the field of works of art*. X-Ray Spectrometry, 2008. **37**(4): p. 450-457.

Buzanich G., Wobrauschek P., Strelci C., Markowicz A., Wegrzynek D., China-Cano E., and Bamford S., *A portable micro-X-ray fluorescence spectrometer with polycapillary optics and vacuum chamber for archaeometric and other applications*. Spectrochimica Acta Part B-Atomic Spectroscopy, 2007. **62**(11): p. 1252-1256.

Participations in conferences:

- 2012:** EXRS, Wien, Austria; → *Oral (Guilherme) and 3 Poster*
- 2011:** Technart, Berlin, Germany; → *Oral (Bidarra) and 3 Poster*
ICXOM, Campinas, Brazil; → *Oral (Radtke)*
- 2010:** SNI, Berlin, Germany; → *Poster*
EXRS, Figueira da Foz, Portugal; → *Oral*
- 2009:** TraceSpec, Mainz, Germany; → *Poster*
X-ray Conference, Denver, USA; → *Poster (Wobrauschek)*
- 2008:** ART - 9th Int. Conference, Jerusalem, Israel; → *Oral (Wegrzynek)*
- 2006:** X-ray Conference, Denver, USA; → *Poster (Wobrauschek)*
- 2005:** ICXOM, Frascati, Italy; → *Poster*
- 2000:** EXRS, Krakow, Poland; → *Oral (Wobrauschek) and Poster*
X-ray Conference, Denver, USA; → *Poster (Wobrauschek)*

Place, Date

Signature